Multiphase chemistry and partitioning of PAHs: numerical modeling from molecular to global scales

Jake Wilson
geb. am 18.06.1993 in London

Dissertation

zur Erlangung des Grades

'Doctor rerum naturalium (Dr. rer. nat.)'

im Promotionsfach Chemie

am Fachbereich Chemie, Pharmazie und Geowissenschaften

der Johannes Gutenberg-Universität in Mainz

Paul Crutzen Graduate School

Mainz, December 2020

I hereby declare that I wrote the dissertation submitted without any unauthorized external assistance and used only sources acknowledged in the work. All textual passages which are appropriated verbatim or paraphrased from published and unpublished texts as well as all information obtained from oral sources are duly indicated and listed in accordance with bibliographical rules. In carrying out this research, I complied with the rules of standard scientific practice as formulated in the statutes of Johannes Gutenberg University Mainz to ensure standard scientific practice.

Mainz, 15th December, Jake Wilson

Abstract

Atmospheric aerosols from anthropogenic sources influence the climate and are associated with disease. Prominent chemical components of these aerosols are polycyclic aromatic hydrocarbons (PAHs), a group of toxic substances produced during the incomplete combustion of fossil fuels and biomass. The concentrations of PAHs are governed by chemical reactions, partitioning between the gas and particle phases, as well as atmospheric transport across the globe. These processes span length scales from the molecular level to the global level, and timescales from nanoseconds to days. To accurately predict the atmospheric concentrations of PAHs and their oxidation products, the mechanisms of each process must be resolved and integrated into mathematical models. In this thesis, the following three topics are addressed:

1. Development of a kinetic model to calculate the time needed for PAHs in the gas phase to reach equilibrium with those adsorbed on the surface of soot particles. The model shows that these timescales are controlled either primarily by the process of desorption or by the process of adsorption, depending on temperature and the number of soot particles. Furthermore, a time-independent equation is analytically derived in order to estimate these timescales without a kinetic model. Under certain conditions, the interplay between the chemical loss, adsorption and desorption of PAHs causes the gas-particle distribution to differ from the state expected at equilibrium. For instance, the surface reaction with O_3 can perturb the particulate fraction of PAHs far below its equilibrium value. For large-scale atmospheric models that assume the gas-particle distribution of PAHs to reach equilibrium instantaneously, these non-equilibrium effects are shown to produce significant errors compared to the kinetic model solution.

2. Application of a chemical transport model (CTMs) to predict the global spatial distribution of two nitrated PAHs (NPAHs) formed in the atmosphere: 2-nitrofluoranthene (2-NFLT) and 2-nitropyrene (2-NPYR). The model is particularly sensitive to the rate at which NPAHs are formed from PAHs, and the rate at which NPAHs are lost by photolytic degradation. Model performance is improved by using a NO_2-dependent formation scheme with lower production rates of NPAHs in less polluted environments. Overall, the model predicts that due to formation during atmospheric transport, 2-NFLT and 2-NPYR are spread across the globe.

3. Development of the computational tool *KinViz* to visualize a set of chemical reactions as a network. Using a directed graph in which chemical species are represented by nodes and chemical reactions by edges, reaction rates are represented by edge weightings to illustrate the evolution of a system of reactions in time. For chemical systems comprised of many coupled reactions, *KinViz* provides an intuitive alternative to time-concentration profiles that greatly enhances the development, analysis and presentation of kinetic models.

Zusammenfassung

Atmosphärische Aerosole aus anthropogenen Quellen beeinflussen das Klima und können gesundheitliche Schäden hervorrufen. Wichtige chemische Bestandteile dieser Aerosole sind polyzyklische aromatische Kohlenwasserstoffe (PAK), eine Gruppe toxischer Substanzen, die bei der unvollständigen Verbrennung fossiler Brennstoffe und Biomasse entstehen. Die PAK-Konzentrationen werden durch chemische Reaktionen, die Verteilung zwischen Gas- und Partikelphase, sowie den atmosphärischen Transport rund um den Globus bestimmt. Diese Prozesse erstrecken sich von molekularen zu globalen Längenskalen und über Zeitskalen von Nanosekunden bis zu Tagen. Um die atmosphärischen Konzentrationen von PAK und ihren Oxidationsprodukten genau vorherzusagen, müssen die Mechanismen jedes Prozesses aufgelöst und in mathematische Modelle integriert werden. In dieser Arbeit werden folgende drei Themen behandelt:

1. Entwicklung eines kinetischen Modells zur Berechnung der Equilibrierung von PAK in der Gasphase mit denen, die an der Oberfläche von Rußpartikeln adsorbiert sind. Das Modell zeigt, dass die Zeitskala dieses Prozesses abhängig von der Temperatur und der Anzahlkonzentration der Rußpartikel sind, und entweder vornehmlich durch den Desorptionsprozess oder vornehmlich durch den Adsorptionsprozess gesteuert werden. Darüber hinaus wird eine zeitunabhängige Gleichung abgeleitet, um diese Zeitskalen ohne kinetisches Modell abzuschätzen. Unter bestimmten Bedingungen führt das Zusammenspiel von chemischem Abbau, Adsorption und Desorption von PAK dazu, dass sich die Gas-Partikelverteilung vom im Gleichgewicht erwarteten Zustand unterscheidet. Beispielsweise kann eine Oberflächenreaktion mit O_3 den Partikelanteil von PAK weit unter ihren Gleichgewichtswert bringen. Im Zusammenhang mit großskaligen atmosphärischen Modellen, bei welchen angenommen wird, dass sich bei der Gas-Partikelverteilung von PAK sofort ein Gleichgewicht einstellt, wird gezeigt, dass diese Nichtgleichgewichtseffekte im Vergleich zur kinetischen Modelllösung signifikante Fehler verursachen können.

2. Anwendung eines chemischen Transportmodells (CTMs) zur Vorhersage der globalen räumlichen Verteilung von zwei in der Atmosphäre gebildeten, nitrierten PAK (NPAK): 2-Nitrofluoranthen (2-NFLT) und 2-Nitropyren (2-NPYR). Das Modell ist besonders sensitiv gegenüber der Bildungsgeschwindigkeit von NPAK aus PAK, und der Geschwindigkeit, mit der NPAK durch photolytischen Abbau verloren gehen. Die Modellperformance wird durch die Verwendung eines NO_2-abhängigen Formationsschemas mit niedrigeren Produktionsraten von NPAK in weniger belasteten Gegenden verbessert. Insgesamt sagt das Modell voraus, dass sich 2-NFLT und 2-NPYR wahrscheinlich aufgrund der kontinuierlichen Nachbildung während des atmosphärischen Transports auf der ganzen Welt ausbreiten.

3. Entwicklung des Rechenwerkzeugs *KinViz* zur Visualisierung eines Satzes chemischer Reaktionen als Netzwerk. Unter Verwendung eines gerichteten Graphen,

in dem chemische Spezies durch Knoten und chemische Reaktionen durch Kanten dargestellt werden, werden Reaktionsumsätze durch Kantengewichtungen dargestellt, um die Entwicklung eines Reaktionssystems mit der Zeit zu veranschaulichen. Für chemische Systeme, die aus vielen gekoppelten Reaktionen bestehen, bietet *KinViz* eine intuitive Alternative zu Zeit-Konzentrationsprofilen, die die Entwicklung, Analyse und Präsentation kinetischer Modelle erheblich verbessert.

Contents

1. Introduction

1.1. Air Pollution in the Anthropocene

As global population (Bongaarts, 2009) and energy consumption (IEA, 2020) increase, human development continues to inflict extensive and often irreversible damage on the natural and human environment (Rockström et al., 2009). A proposed geological epoch, the Anthropocene, accentuates that humans are now the main force acting on the climate and environment (Goudie, 2018). The anthropogenic impact on the atmosphere in particular is extensive and multifaceted: air pollutants from human activity alter the hydrological cycle by affecting cloud formation and precipitation (Rosenfeld, 2000; Ramanathan et al., 2001), refrigerant gases such as chlorofluorocarbons (CFCs) catalyse the destruction of stratospheric ozone (Solomon, 1999), and rising concentrations of carbon dioxide and methane pose existential risks to human societies and ecosystems through global warming (IPCC, 2013). Furthermore, air pollution is directly linked to chronic and acute diseases (Pope III, 2002; Kampa and Castanas, 2008; Reinmuth-Selzle et al., 2017; Cohen et al., 2017), and fine particulate matter ($PM_{2.5}$) alone is estimated to cause 3.3 million premature deaths annually across the globe (Lelieveld et al., 2015).

Air pollution contains a complex mixture of gas and particle-phase chemical species with distinct physicochemical and toxicological properties (Harrison and Yin, 2000; Mudway et al., 2020). The chemical and physiological mechanisms by which these components cause disease are not fully understood (Kelly and Fussell, 2020). In order to implement targeted environmental regulations and develop novel mitigation technologies for reducing air pollution, the exact chemical components responsible for disease must be identified.

1.2. Atmospheric Aerosol Particles

Atmospheric aerosols consist of small organic and inorganic particles suspended in air, typically ranging between 0.002 and 100 μm in diameter (Finlayson-Pitts and Pitts, 1999). Aerosol particles may be emitted directly from natural and anthropogenic sources (termed primary, Lamarque et al., 2010), or formed in the atmosphere by chemical

reactions of volatile gases that form low-volatility products (termed secondary, Kroll and Seinfeld, 2008; Hallquist et al., 2009). Most aerosol particles in the atmosphere originate from natural sources such as sea salt, mineral dust, sulfate formed from volcanic SO_2 emissions, and biogenic sources (Andreae and Crutzen, 1997; Andreae and Rosenfeld, 2008). However, a significant fraction of aerosol particles are emitted from anthropogenic sources, such as combustion processes (Lighty et al., 2000).

Aerosol particles play a fundamental role in the climate via radiative forcing (Charlson et al., 1992), act as cloud condensation nuclei (Pöschl et al., 2010), and enable heterogeneous chemistry (Ravishankara, 1997; George and Abbatt, 2010; George et al., 2015). The composition and physicochemical properties of aerosol particles influence their function in the atmosphere (Pöschl, 2005). Atmospheric conditions influence the properties of aerosol particles, for instance, temperature and relative humidity both affect viscosity (Koop et al., 2011). Aerosol particles undergo aging due to reactions with atmospheric oxidants, thus resulting in further transformation of physical and chemical properties (Pöschl, 2005; George and Abbatt, 2010).

One type of aerosol particle with anthropogenic sources is soot, which plays a particularly important role in the climate due to its ability to adsorb solar radiation (Ramanathan and Carmichael, 2008). Although epidemiological and toxicological evidence associates soot particles with disease (Lighty et al., 2000), the exact mechanisms are not fully resolved. Soot particles are comprised of over 80% carbon in graphitic-like crystalline and amorphous domains (Sadezky et al., 2005), and are formed during combustion by a series of high-temperature reactions between carbon-containing precursors (Haynes and Wagner, 1981; Bockhorn, 1994; Frenklach, 2002). Fresh soot tends to be hydrophobic, but due to oxidative reactions, the surface becomes more hydrophilic, thus facilitating the removal of soot particles from the atmosphere by wet deposition (Zuberi et al., 2005). One key group of chemical components linked to the toxicity of soot particles is PAHs.

1.3. Polycyclic Aromatic Hydrocarbons

Polycyclic aromatic hydrocarbons (PAHs) are a group of organic compounds consisting of multiple aromatic rings (Keyte et al., 2013). Many PAHs are considered a risk to human health due to their carcinogenic (Boström et al., 2002) and teratogenic properties (Kim et al., 2013). PAHs are mainly emitted into the atmosphere from anthropogenic sources, primarily due to the incomplete combustion of fossil fuels and biomass (Ravindra et al., 2008). The term partitioning refers to the distribution of PAHs, which may either be individual molecules and molecular clusters in the gas phase (Rapacioli et al., 2005), or sorbed on and within aerosol particles (Finlayson-Pitts and Pitts, 1999). Among several factors, the partitioning of PAHs depends on their molecular structure, temperature, and the particle number concentration and type (Lohmann and Lammel, 2004). Assuming

equilibrium, thermodynamic predictors can be used to estimate the partitioning of PAHs (Pankow, 1994; Dachs and Eisenreich, 2000; Shahpoury et al., 2016) and simplify their description in larger-scale models. However, the timescales required for PAHs to reach partitioning equilibrium under different atmospheric conditions have not been quantified and therefore the equilibrium assumption remains to be validated. A description of non-equilibrium effects in the partitioning process requires a detailed kinetic model.

Following emission, PAHs can be transported in the troposphere far from source, including remote regions such as the Arctic (Friedman et al., 2014), thus making them ubiquitous in the environment (Baek et al., 1991). During transport, multiphase chemical reactions transform atmospheric PAHs into oxidized products such as quinones and nitrated PAHs (NPAHs) (Albinet et al., 2008; Tomaz et al., 2017). These reactions may occur homogeneously (Atkinson and Arey, 1994) or heterogeneously (Zimmermann et al., 2013) and involve oxidants such as hydroxyl radicals (OH), ozone (O_3), and nitrate radicals (NO_3) (Keyte et al., 2013). The carcinogenicity of NPAHs (Rosenkranz and Mermelstein, 1985; Bandowe and Meusel, 2017) are of particular concern for human health, as is the ability of quinones to form semi-quinones and generate reactive oxygen species (ROS; Bolton et al., 2000), a group of oxygen containing oxidants associated with oxidative stress (Sies et al., 2017). While extensive monitoring of atmospheric PAH concentrations is in place (Boström et al., 2002), the spatial distributions of PAH transformation products such as NPAHs are far less resolved. Chemical transport models are one method to predict the concentrations of these toxic species, and hence human exposure on regional and global scales.

1.4. Kinetic Models for Multiphase Chemistry

The formation and loss of chemical species during chemical reactions can be described mathematically with rate equations, following the laws of mass action (Turanyi and Tomlin, 2014). While gas-phase reactions can often be described in a single concerted reaction step, it is particularly challenging to resolve the mechanisms and kinetic parameters of chemical reactions that take place on aerosol particles (Abbatt et al., 2012). In heterogeneous systems, chemical reactions are closely coupled to mass-transport processes, such as diffusion, adsorption and desorption. Molecules may undergo adsorption following collision with the surface of aerosol particles. This binding may be characterized by relatively weak intermolecular forces, termed physisorption, or by reaction to form strong chemical bonds, termed chemisorption.

In order to develop kinetic models that contain transferable parameters, it is often necessary to resolve mass-transport processes explicitly. Previously, a kinetic model framework for gas-particle interfaces (PRA; Pöschl et al., 2007) has been adopted to develop mathematical models for surface chemistry (K2-SURF; Shiraiwa et al., 2009),

both surface and bulk-phase chemistry (KM-SUB; Shiraiwa et al., 2010), and account for the dynamic size change of aerosol particles (KM-GAP; Shiraiwa et al., 2012). In some cases, global optimization algorithms are required to obtain multiple unknown kinetic parameters from an experimental data set (e.g. MCGA; Berkemeier et al., 2017). Kinetic models have been used to investigate the diffusion-limited reactions between ozone and benzo(a)pyrene in SOA (Zhou et al., 2013), ice nucleation on glassy organic aerosol particles (Berkemeier et al., 2014), and the degradation of particle-phase pesticides (Socorro et al., 2017).

Kinetic models have also been used to study the health effects associated with aerosol particles by quantifying the generation of reactive oxygen species in the epithelial lining fluid (ELF; Lakey et al., 2016) and surrogate mixtures (Tong et al., 2018). After inhalation, the ELF is the first line of defense in the respiratory tract and lungs (Kelly et al., 1996) and consists of a liquid layer of liquid proteins (Hermans and Bernard, 1999) and antioxidants such as ascorbate, urate, and glutathione (van der Vliet et al., 1999). Given that chemical species are coupled by numerous interdependent and competing reactions varying across vastly different timescales, the mathematical and mechanistic description of these complex systems with kinetic models raises a unique set of challenges. One particular challenge is the visualization of model output. Time-concentration profiles which are conventionally used to analyze kinetic models are unable to convey results in an intuitive way. In recent years, the field of systems chemistry has evolved to investigate complex mixtures of interacting chemicals, with a particular focus on emergent properties such as feedback loops and amplification (Ludlow and Otto, 2007). Novel visualization tools are required to intuitively view kinetic models from a systems perspective and build mechanistic intuition in complex systems.

1.5. Chemical Transport Models for Atmospheric Pollutants

While kinetic models are useful for describing the micro-physical processes of aerosol particles, chemical transport models (CTMs) are required to establish the overall fate of a chemical species in the atmosphere. Chemical transport models use mathematical descriptions of physical and chemical processes to describe the emission, chemical formation and loss, transport, and deposition of species such as PAHs (Seinfeld and Pandis, 1998). In the absence of long-term monitoring data, chemical transport models allow the prediction of concentrations and in combination with population data, estimation of human exposure to atmospheric pollutants (Anenberg et al., 2010; Brauer et al., 2016). Chemical transport models that focus on a single air parcel with a moving coordinate system are termed Lagrangian, while those that use a fixed spatial coordinate system are termed Eulerian (Jacob, 1999). The choice of spatial resolution for CTMs is a com-

promise between the computational cost and the requirement for model detail, and the lengths of grid cells at the equator can range from several to hundreds of kilometres. Rather than using height to represent the vertical levels in the atmosphere, many CTMs use a combination of sigma coordinates which follow surface topography and pressure coordinates (Brasseur and Jacob, 2017).

The spatiotemporal distributions of PAHs have been studied using Eulerian chemical transport models at urban (San José et al., 2013), regional (Inomata et al., 2012), and global (Friedman and Selin, 2012) scales. A global emissions inventory for sixteen PAHs is available at a 0.1° by 0.1° spatial resolution (Shen et al., 2013) and accounts for key sources such as biomass burning and motor vehicles. The dry deposition of gas- and particle-phase PAHs is calculated using depositional velocities (Wesely, 1989; Kerkweg et al., 2006) and the wet deposition of gas-phase PAHs is dependent on Henry's coefficient (Tost et al., 2006). Global models have been shown to be sensitive to the choice of gas-particle partitioning scheme (Lammel et al., 2009). However, for PAHs, the partitioning equilibrium is conventionally assumed to be restored instantaneously at each model time step. Recently, the mass-transport limitations that control heterogeneous reactions between PAHs and O_3 have been explicitly included in CTMs (Shrivastava et al., 2017; Mu et al., 2018). Spatial distributions of PAH concentrations obtained with chemical transport models may be combined with population data to assess the burden of diseases, such as the incremental lifetime cancer risk (ILCR; Shen et al., 2015; Shrivastava et al., 2017). Despite these achievements, the transformation products of PAHs such as NPAHs have not before been investigated with regional and global chemical transport models.

1.6. Research Objectives

The research objectives of this PhD project are to explain the time dependence of gas-particle interactions in the atmosphere, predict the spatial distributions of semi-volatile pollutants, and to visualize systems of complicated chemical reactions. Specifically, this project addresses three key topics with the following objectives:

A) Investigate the non-equilibrium distribution of toxic polycyclic aromatic hydrocarbons (PAHs) between the gas phase and the surface of aerosol particles with a kinetic model.

1. Determine the timescales needed for PAHs to equilibrate on the surface of soot particles and examine the underlying molecular processes that control them.

2. Compare these equilibration timescales with the timescales of chemical reactions with either ozone or hydroxyl radicals. Classify the effects of non-equilibrium behavior on the distribution of PAHs.

3. Assess the implications for chemical transport models (CTMs) that assume instantaneous equilibration by comparing solutions from an operator-splitting approach and an explicitly-coupled kinetic model.

B) Predict the global spatial distribution of two secondarily formed nitrated PAHs (NPAHs) using a CTM.

1. Adapt the SVOC sub-model, previously used for PAHs, to include the formation and degradation of 2-nitrofluoranthene and 2-nitropyrene. Collect observational data from the literature and validate the model.

2. Explore the sensitivity of the model to the rate of photolytic degradation and to a mechanism with a NO_2-dependent formation yield.

C) Develop a tool *KinViz* to automatically visualize complex chemical systems as a weighted network.

1. Provide an alternative to time-concentration profiles by converting of a system of reactions into a directed graph, in which nodes represent chemical species and edges represent chemical reactions.

2. Establish a set of visualization aids to represent the time-concentration output of kinetic models as weighted edges in the directed graph.

1.7. Overview

The key results of this PhD project are summarized in three first-author manuscripts for publication in peer-reviewed scientific journals. One of these manuscripts has been published in an internationally leading journal of environmental science, the second is available as preprint undergoing public peer review, and the third will soon be submitted. Besides these three main studies, this PhD project intersects nine further publications which either explore the underlying mechanisms whereby air pollutants generate reactive oxygen species or the adsorption of gases to graphitic surfaces. In all three first-author studies, numerical models and computational algorithms are used to integrate, quantify or visualize chemical processes occurring in the atmosphere. An overview of the key topics of this PhD project and the concepts that connect them is shown (Fig. 1.1).

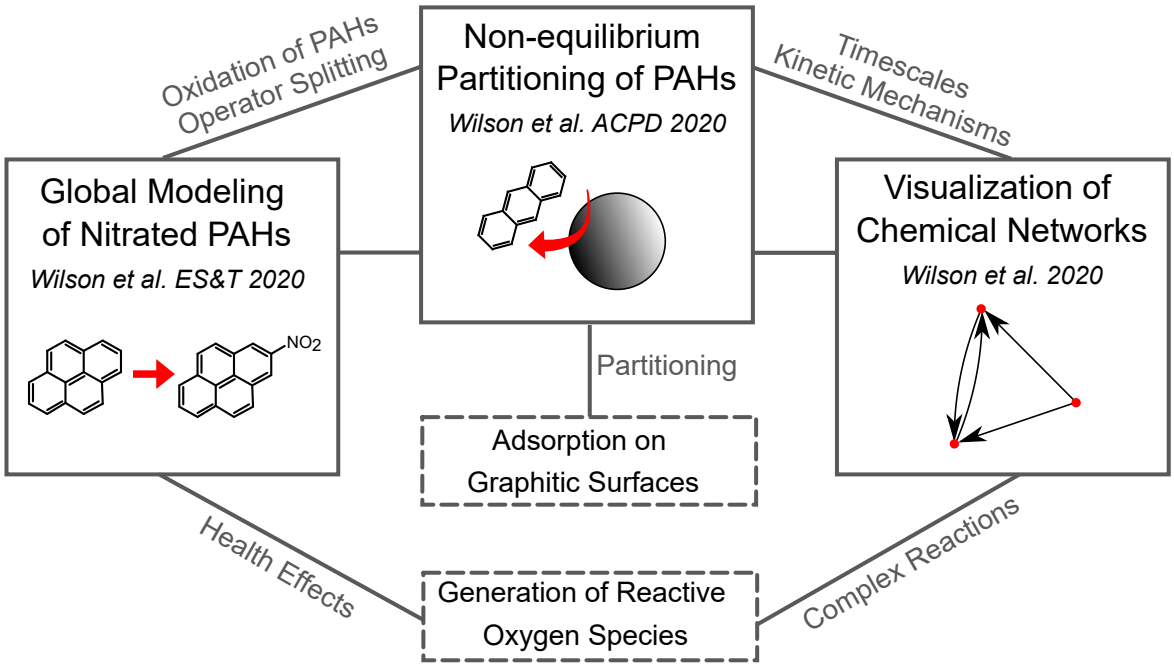

Figure 1.1.: *A graphical overview of the structure of this PhD project. The solid boxes refer to three key topics that are presented within first-author papers. The two dashed boxes represent sub-topics that are explored in co-authored papers. The lines show the common concepts between topics.*

2. Results

2.1. Non-equilibrium Partitioning of PAHs

This chapter has already been published as a preprint in Atmospheric Chemistry and Physics Discussions (ACPD) and is undergoing peer review. I am the first author of this publication and my personal contribution to this work included writing code for the kinetic model (using systems of differential equations in MATLAB), creating the framework to emulate operator splitting, and implementing optimization algorithms to evaluate the optimal time step. Furthermore, I was responsible for running simulations and carrying out data analysis and visualization (using Python and MATLAB). This also included designing and writing code to automatically generate phase portraits for a given kinetic model. I also derived the time-independent equation for equilibration time. Alongside my coauthors, I played a primary role in initiating and designing the research, analyzing the results, preparing figures, and writing the manuscript.

Atmos. Chem. Phys. Discuss., in review (2020).

Non-equilibrium interplay between gas-particle partitioning and multiphase chemical reactions of semi-volatile compounds: mechanistic insights and practical implications for atmospheric modeling of PAHs

Jake Wilson[1], Ulrich Pöschl[1], Manabu Shiraiwa[2], and Thomas Berkemeier[1]

[1]Multiphase Chemistry Department, Max Planck Institute for Chemistry, Mainz, Germany
[2]Department of Chemistry, University of California, Irvine, CA, USA

https://doi.org/10.5194/acp-2020-1000
Preprint. Discussion started: 7 October 2020

Atmospheric Chemistry and Physics Discussions

Non-equilibrium interplay between gas-particle partitioning and multiphase chemical reactions of semi-volatile compounds: mechanistic insights and practical implications for atmospheric modeling of PAHs

Jake Wilson[1], Ulrich Pöschl[1], Manabu Shiraiwa[2,*], and Thomas Berkemeier[1,*]

[1]Multiphase Chemistry Department, Max Planck Institute for Chemistry, Mainz, Germany
[2]Department of Chemistry, University of California, Irvine, CA, USA

Correspondence: Thomas Berkemeier (t.berkemeier@mpic.de) and Manabu Shiraiwa (m.shiraiwa@uci.edu)

Abstract. Polycyclic aromatic hydrocarbons (PAHs) are carcinogenic air pollutants. The dispersion of PAHs in the atmosphere is influenced by gas-particle partitioning and chemical loss. These processes are closely interlinked and may occur at vastly differing timescales, which complicates their mathematical description in chemical transport models. Here, we use a kinetic model that explicitly resolves mass transport and chemical reactions in the gas and particle phases to describe and explore the dynamic and non-equilibrium interplay of gas-particle partitioning and chemical losses of PAHs on soot particles. We define the equilibration timescale τ_{eq} of gas-particle partitioning as the e-folding time for relaxation of the system to the partitioning equilibrium. We find this metric to span seconds to hours depending on temperature, particle surface area and the type of PAH. The equilibration time can be approximated using a time-independent equation $\tau_{eq} \approx \frac{1}{k_{des}+k_{ads}}$, which depends on the desorption rate coefficient k_{des} and adsorption rate coefficient k_{ads}, both of which can be calculated from experimentally-accessible parameters. The model reveals two regimes in which different physical processes control the equilibration timescale: a *desorption-controlled* and an *adsorption-controlled* regime. In a case study with the PAH pyrene, we illustrate how chemical loss can perturb the equilibrium particulate fraction at typical atmospheric concentrations of O_3 and OH. For the surface reaction with O_3, the perturbation is significant and increases with the gas-phase concentration of O_3. Conversely, perturbations are smaller for reaction with the OH radical, which reacts with PAHs on both the surface of particles and in the gas phase. Global and regional chemical transport models typically approximate gas-particle partitioning with instantaneous equilibration approaches. We highlight scenarios in which these approximations deviate from the explicit-coupled treatment of gas-particle partitioning and chemistry presented in this study. We find that the discrepancy between solutions depends on the operator-splitting time step and the choice of time step can help to minimize the discrepancy. The findings and techniques presented in this work are not only relevant for PAHs, but can also be applied to other semi-volatile substances that undergo chemical reactions and mass transport between the gas and particle phase.

https://doi.org/10.5194/acp-2020-1000
Preprint. Discussion started: 7 October 2020

Atmospheric Chemistry and Physics Discussions

1 Introduction

Polycyclic aromatic hydrocarbons (PAHs) are air pollutants that are structurally characterized by their fused aromatic ring systems (Keyte et al., 2013). Given their carcinogenic properties (Boström et al., 2002), developmental toxicity (Billiard et al., 2008) and abundance in the environment (Ravindra et al., 2008), PAHs pose a risk to human health (Kim et al., 2013).

PAHs are semi-volatile compounds that may exist in the gas phase, adsorbed on the surface of aerosol particles, or absorbed into the bulk of particles. The transport and distribution between these phases is referred to as gas-particle partitioning. For PAHs, an accurate model description of gas-particle partitioning is needed to interpret monitoring data, determine atmospheric burden and lifetime, and ultimately assess the hazards their emissions pose to human health.

In equilibrium, the flux of a semi-volatile species from the gas phase to the particle surface is equal to the flux that desorbs back into the gas phase. The state of the system at equilibrium can be described mathematically with thermodynamic entities (Junge, 1977; Yamasaki et al., 1982; Pankow, 1994). The equilibrium gas-particle partitioning of semi-volatile compounds is determined by both adsorption onto the particle surfaces and absorption into the particle bulk. The relative contributions of these processes depend on the concentrations, composition and phase state of particles. Physicochemical properties of a compound, such as the octanol-air partition coefficient K_{OA} (Finizio et al., 1997; Harner and Bidleman, 1998), the soot-air partition coefficient K_{SA} (Dachs and Eisenreich, 2000; Lohmann and Lammel, 2004) and Abraham descriptors (Arp et al., 2008; Shahpoury et al., 2016) are typically used to predict the position of equilibrium. In terms of surface adsorption, soot or black carbon particles may be especially relevant for the gas-particle partitioning of PAHs as they exhibit large energies of desorption (Kubicki, 2006; Guilloteau et al., 2010) and are often co-emitted (Miguel et al., 1998).

Field observations of PAH gas-particle partitioning in the form of particulate fractions often differ from the predictions of equilibrium models (Lohmann et al., 2000; Mandalakis et al., 2002; Terzi and Samara, 2004; Callén et al., 2008; Akyüz and Çabuk, 2010; Lammel et al., 2010; Wei et al., 2015). These discrepancies can be induced by perturbations to the equilibrium such as emissions, changes in temperature, dry and wet deposition, or chemical reaction (Pankow and Bidleman, 1992), but only persist if the rate of the adsorption-desorption kinetics is slow compared to rate of the perturbing process. In other words, partitioning equilibrium will still be maintained if the equilibration timescale is shorter than the perturbation timescale. This means that accurate knowledge of equilibration timescales is vital to assess whether non-equilibrium effects may occur.

Gas-particle partitioning is an important process in chemical transport models (CTMs) which describe the long-distance transport and chemical degradation of atmospheric constituents such as PAHs (Shrivastava et al., 2017; Mu et al., 2018). In CTMs, PAHs are partitioned, transformed and transported in discrete time steps, often using the method of operator splitting. With operator splitting, the partitioning equilibrium is restored at each model time step through instantaneous equilibration (Galarneau et al., 2014) rather than treating gas-particle partitioning continuously. PAH concentrations predicted by CTMs have been shown to depend on the employed treatment of gas-particle partitioning. For instance, Lammel et al. (2009) found that using different equilibrium partitioning models influenced atmospheric cycling, the total environmental fate, and long-range transport potential of PAHs. Friedman et al. (2014) found that implementing a partitioning scheme in which PAHs slowly evaporate from aerosol particles yielded the better agreement between observed and simulated concentration and par-

https://doi.org/10.5194/acp-2020-1000
Preprint. Discussion started: 7 October 2020


Atmospheric Chemistry and Physics Discussions

titioning data compared to the instantaneous equilibration approach. Overall, CTMs that assume equilibrium partitioning tend to be more common than those accounting for mass-transfer limitations explicitly, as can be seen from a recent review of partitioning methods in regional-scale transport models of SOA (McFiggans et al., 2015).

Equilibration timescales of gas-partitioning may be estimated theoretically, using analytical equations or numerical models. By solving analytical transport equations, the equilibration timescales of partitioning for volatile inorganic compounds were found to depend on the size of particles (Meng and Seinfeld, 1996). More recently, there have been numerical simulations for secondary organic aerosol (SOA) as a function of temperature and relative humidity (Shiraiwa and Seinfeld, 2012; Li and Shiraiwa, 2019). Alternatively, equilibration timescales may also be obtained experimentally. For example, Saleh et al. (2013) found the equilibration timescale of SOA formed by α-pinene ozonolysis to be less than 30 min following a perturbation in temperature. Furthermore, the interplay between partitioning and multiphase reaction of OH with alkanes was shown to influence the distribution of product isomers (Zhang et al., 2015).

For PAHs, several studies have investigated the timescales of gas-particle partitioning from the perspective of absorptive partitioning. Rounds and Pankow used a radial diffusion model to investigate the kinetic limitations of partitioning resulting from diffusion of a semi-volatile compound absorbed within a particle (Rounds and Pankow, 1990). Odum et al. (1994) additionally included a parameter to accounting for mass-transfer limitations at the surface. In chamber experiments, Kamens et al. (1995) examined the equilibration timescales of PAHs. However, an in-depth analysis of the important case of PAH adsorption onto the surface of soot remains elusive. In recent years, the desorption rate coefficients of PAHs from soot have been experimentally parameterized over a range of atmospherically-relevant temperatures (Guilloteau et al., 2010). However, a systematic comparison between the equilibration timescales of partitioning and the timescales of loss processes has not been carried out.

In this study, we examine the timescales of gas-particle partitioning and chemical loss of PAHs with a kinetic model in which both processes are explicitly coupled. The model uses the conventions of the PRA framework (Pöschl et al., 2007) and is based on the kinetic double-layer model for aerosol surface chemistry (K2-SURF; Shiraiwa et al., 2009). We quantify the equilibration timescales of six PAHs on the model surface of solid soot particles for different temperatures and particle number concentrations (Sect. 3.2). We illustrate how the combination of slow partitioning and chemical loss of PAHs can perturb the particulate fraction from equilibrium (Sect. 3.3.2) and alter chemical lifetime (Sect. 3.3.1). We apply the knowledge gained from the kinetic model calculations to the description of gas-particle partitioning in CTMs by comparing the explicitly-coupled solution to a method mimicking operator splitting with instantaneous equilibration and evaluate the performance of both methods in different scenarios.

2 Methods

2.1 Kinetic Model

A modified version of the kinetic double-layer model K2-SURF is used for all simulations (Shiraiwa et al., 2009). The original K2-SURF model consists of a near-surface gas phase and surface layer, with gas diffusion from the far-surface gas phase represented by a correction factor (Fig. A1). In this study, we added explicit treatment of gas diffusion to K2-SURF to track

https://doi.org/10.5194/acp-2020-1000
Preprint. Discussion started: 7 October 2020

Atmospheric Chemistry and Physics Discussions

gas-phase PAH concentrations. PAHs reversibly desorb and adsorb between the aerosol particle surface and the near-surface gas phase. The rate coefficient for PAH desorption from the particle surface $k_{\mathrm{des}} = Ae^{-E_{\mathrm{A}}/RT}$ (s^{-1}) depends on temperature T and two parameters determined from experiment: the Arrhenius factor A and the activation energy of desorption E_{A} (Guilloteau et al., 2010). R is the gas constant. Aerosol particles are assumed to be monodisperse and to consist of a spherical, impenetrable solid carbon core. The system is closed with respect to aerosol particles and PAH in all simulations. In simulations involving chemical reactions, the system is open with respect to oxidants, i.e. gas-phase OH and $\mathrm{O_3}$ concentrations are fixed.

The differential equations in Eqs. 1-3 describe the time evolution of $[\mathrm{PAH}]_{\mathrm{g}}$ (cm^{-3}), $[\mathrm{PAH}]_{\mathrm{gs}}$ (cm^{-3}) and $[\mathrm{PAH}]_{\mathrm{s}}$ (cm^{-2}), which are the concentrations of PAH in the gas phase, near-surface gas phase and on the surface of aerosol particles, respectively. J_{des} ($\mathrm{cm}^{-2}\,\mathrm{s}^{-1}$), J_{ads} ($\mathrm{cm}^{-2}\,\mathrm{s}^{-1}$) and J_{diff} (s^{-1}) are the desorption flux, adsorption flux and gas diffusion flux. Each flux term is described in detail in section A of the appendix.

$$\frac{\mathrm{d}[\mathrm{PAH}]_{\mathrm{g}}}{\mathrm{d}t} = -J_{\mathrm{diff}} N_{\mathrm{p}} - L_{\mathrm{g}} \tag{1}$$

$$\frac{\mathrm{d}[\mathrm{PAH}]_{\mathrm{gs}}}{\mathrm{d}t} = \frac{(J_{\mathrm{des}} - J_{\mathrm{ads}}) d_{\mathrm{p}}^2 \pi + J_{\mathrm{diff}}}{V_{\mathrm{gs}}} \tag{2}$$

$$\frac{\mathrm{d}[\mathrm{PAH}]_{\mathrm{s}}}{\mathrm{d}t} = -J_{\mathrm{des}} + J_{\mathrm{ads}} - L_{\mathrm{s}} \tag{3}$$

The surface area of a single aerosol particle with diameter d_{p} (cm) is $d_{\mathrm{p}}^2\pi$, V_{gs} (cm^3) is the volume of gas in the near-surface gas phase for a single aerosol particle and N_{p} (cm^{-3}) is the particle number concentration. L_{g} ($\mathrm{cm}^{-3}\,\mathrm{s}^{-1}$) is the rate of chemical loss in the gas phase and L_{p} ($\mathrm{cm}^{-2}\,\mathrm{s}^{-1}$) is the rate of chemical loss in the particle phase. Reactions of PAHs within the near-surface gas phase are considered to be negligible due to the small fraction of PAHs in this volume. Sources of PAHs are not considered in this study.

2.2 Chemical reactions

The surface reaction between PAH and $\mathrm{O_3}$ is modeled using a Langmuir-Hinshelwood mechanism, including reversible adsorption of $\mathrm{O_3}$ onto the surface of aerosol particles and reaction of surface-adsorbed $\mathrm{O_3}$ with surface-adsorbed PAH.

$$\mathrm{O_{3(gs)} \rightleftharpoons O_{3(s)}} \tag{R1}$$

$$\mathrm{PAH_{(s)} + O_{3(s)} \rightarrow product_{(s)}} \tag{R2}$$

https://doi.org/10.5194/acp-2020-1000
Preprint. Discussion started: 7 October 2020

Atmospheric Chemistry and Physics Discussions

The rate coefficient for reaction of PAH with O_3, $k_{PAH+O3} = 2.7 \times 10^{-17} cm^2\,s^{-1}$, and the corresponding mass-transport parameters are taken from Shiraiwa et al. (2009) (Table A1). Reaction products are treated as inert and non-volatile. Note that the reaction between O_3 and benzo(a)pyrene on the surface of soot has been suggested to involve the formation of long-lived reactive oxygen intermediates (ROI; Shiraiwa et al., 2011). Such a detailed chemical mechanism is beyond the scope of this study, which instead focuses on the interaction of partitioning and chemistry, and has thus been omitted for simplicity. The gas-phase reaction between O_3 and PAH is considered negligible and is therefore not included (Keyte et al., 2013). The reaction between PAH and OH is accounted for in both the gas phase and on the surface of particles.

$$PAH_{(g)} + OH_{(g)} \rightarrow product_{(g)} \tag{R3}$$

$$PAH_{(s)} + OH_{(gs)} \rightarrow product_{(s)} \tag{R4}$$

The gas-phase reaction between PAH and OH is modeled with the rate coefficient $k_{PAH+OH} = 6.58 \times 10^{-11} cm^3\,s^{-1}$ (theoretical calculation for pyrene at 298 K, Zhang et al., 2014). We do not consider temperature dependence of chemical rate coefficients in this model. The reaction between PAH and OH on the surface of particles is treated with an Eley-Rideal like mechanism using a surface reaction probability of 0.32 (obtained for pyrene, Bertram et al., 2001) and assuming an OH gas diffusion coefficient D_g of $0.21 cm^2\,s^{-1}$ (Tang et al., 2014). The uptake of OH onto the surface of particles is considered to be irreversible.

2.3 Particulate fraction

The measured distribution of PAHs (and other semi-volatiles) between the particle phase and the gas phase is commonly described with the particulate fraction Φ, i.e. the fraction of total PAHs associated with aerosol particles (Eq. 4).

$$\Phi = \frac{[PAH]_p}{[PAH]_p + [PAH]_g} \tag{4}$$

The total concentration of PAH adsorbed on the surface of aerosol particles $[PAH]_p$ (cm^{-3}) is the product of the surface area of a single particle $d_p^2\pi$ with diameter d_p, the particle number concentration N_p, and surface concentration of PAH, $[PAH]_s$ (cm^{-2}; Eq. 5).

$$[PAH]_p = d_p^2 \pi N_p [PAH]_s \tag{5}$$

2.4 Equilibration timescale τ_{eq}

To quantify the time for PAHs to reach their equilibrium distribution between the gas phase and the particle phase we use the equilibration timescale (τ_{eq}), defined as e-folding time for the relaxation of the system to gas-particle partitioning equilibrium.

https://doi.org/10.5194/acp-2020-1000
Preprint. Discussion started: 7 October 2020

Atmospheric Chemistry and Physics Discussions

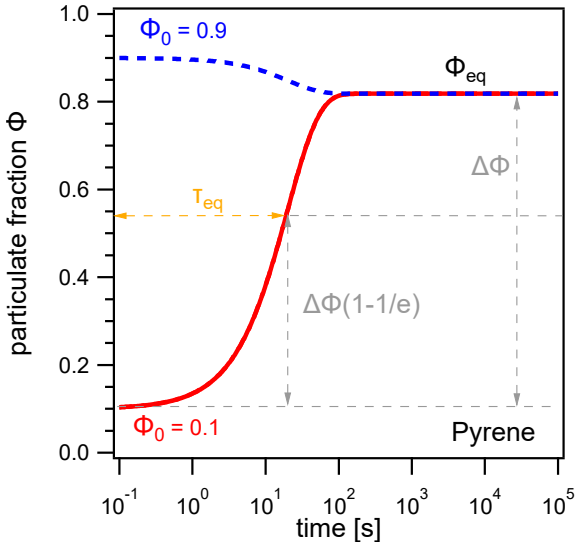

Figure 1. The evolution of the particulate fraction Φ of pyrene with respect to time, starting from initial particulate fractions $\Phi_0 = 0.1$ (red) and $\Phi_0 = 0.9$ (blue). The equilibration timescale τ_{eq} is defined as the time required for the system to achieve 63.2 % of $\Delta\Phi$, the difference between Φ_0 and Φ_{eq}.

Figure 1 shows results from a kinetic box model simulation with a concentration of pyrene in air of 5×10^5 cm^{-3}, temperature $T = 298$ K, particle number concentration $N_p = 1\times10^4$ $\mathrm{particles\,cm}^{-3}$, and particle diameter $d_p = 200$ nm. No chemical loss of pyrene is included here. τ_{eq} is obtained numerically from model outputs by interpolating the time required by the system to achieve $1 - \frac{1}{e}$ (i.e. $\approx$ 63.2 %) of the difference $\Delta\Phi$ between an initial particulate fraction Φ_0 and the equilibrium particulate fraction Φ_{eq}.

In this example, pyrene reaches Φ_{eq} after $\approx$ 2 minutes and the equilibration timescale is independent of the initial particulate fraction, i.e. τ_{eq} is the same regardless of whether $\Phi_0 = 0.1$ or $\Phi_0 = 0.9$. In fact, τ_{eq} is found to be independent of the choice of Φ_0 for most conditions due to the first-order and hence mono-exponential nature of the adsorption and desorption processes. This allows for consistent intercomparison across different temperatures and particle number concentrations without changing starting distributions. Exceptions may occur in cases where surface adsorption is not strictly a first-order process, either due to surface saturation effects or gas phase diffusion limitations. These conditions occur at very low particle number concentrations (typically $< 1\times10^3$ $\mathrm{particles\,cm}^{-3}$) and further details are given in Appendix B.

3 Results and discussion

3.1 Extreme cases of multiphase chemistry and partitioning interaction

Three extreme cases can be formulated when partitioning and chemical-loss processes of a semi-volatile compound take place at different relative timescales (Fig. 2).

https://doi.org/10.5194/acp-2020-1000
Preprint. Discussion started: 7 October 2020

Atmospheric Chemistry and Physics Discussions

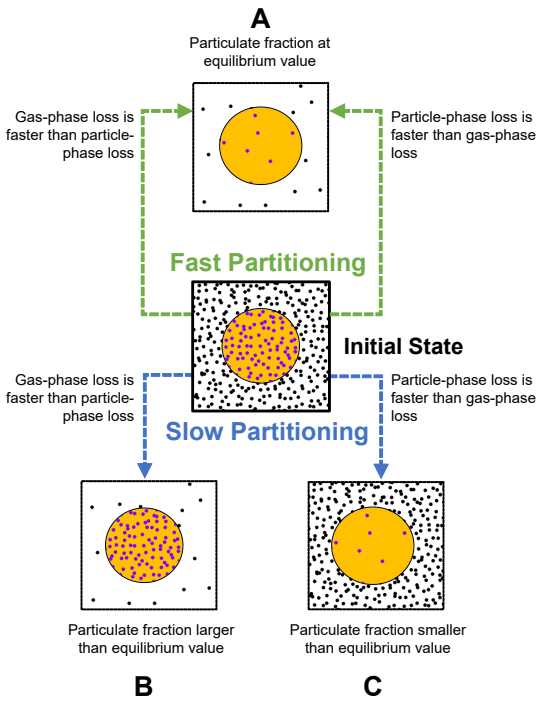

Figure 2. Schematic on how the gas-particle partitioning equilibrium of a semi-volatile compound may be perturbed from an initial state (center) due to chemical loss, depending on equilibration timescales. If the timescales of partitioning are shorter than the timescales of chemical loss, the system is able to maintain equilibrium (A). However, the combination of rapid gas-phase loss and slow replenishment from the particle phase increases the particulate fraction above the equilibrium value (B). In turn, the combination of rapid particle-phase loss and slow replenishment by condensation decreases particulate fraction below the equilibrium value (C).

When the timescale of partitioning is short compared to the timescales of chemical loss, molecules are redistributed quickly between both phases (case A, Fig. 2). In this case, the relative amounts of gas- and particle-phase species will remain very close to their equilibrium values ($\Phi \approx \Phi_{eq}$). This is independent of whether molecules are lost primarily from the gas phase or from the particle phase.

In contrast, if the timescale of the partitioning process is slow and the chemical loss rates from the gas and particle phase differ substantially, the particulate fraction will be perturbed from its equilibrium value (cases B and C, Fig. 2). When the loss rate in the gas phase exceeds the loss rate in the particle phase, the particulate fraction increases beyond its equilibrium value ($\Phi > \Phi_{eq}$; case B, Fig. 2). However, when the loss rate in the particle phase is greater than that in the gas phase, the particulate fraction decreases ($\Phi < \Phi_{eq}$; case C, Fig. 2).

Unlike these scenarios, chemical loss and partitioning timescales may not differ substantially. Likewise, chemical losses are likely to take place in both phases simultaneously. Every real system must therefore be seen as superposition of these cases. The extent to which perturbation occurs depends upon the difference between partitioning and chemical reactions timescales. An in-depth discussion on the magnitude of perturbation is provided in Sect. 3.3.

https://doi.org/10.5194/acp-2020-1000
Preprint. Discussion started: 7 October 2020

Atmospheric Chemistry and Physics Discussions

Hence, two preconditions are required for the particulate fraction Φ of the system to be perturbed from the equilibrium particulate fraction predicted by equilibrium partitioning theory Φ_{eq}: 1) Slow partitioning relative to the timescale of chemical loss and 2) an imbalance of chemical loss between the gas and particle phases.

If timescales of chemical loss and partitioning were known for all natural systems, they could be classified and mathematically treated in the respective limiting case. In this manuscript, we: 1) estimate the partitioning timescales of PAH on soot as a function of atmospheric conditions, 2) compare these timescales to typical chemical loss rates in order to investigate whether perturbations from equilibrium exist, and 3) explore the implications of treating partitioning and chemistry separately in chemical transport models.

3.2 Partitioning equilibration timescales for PAHs on soot

τ_{eq} depends on the molecular structure of the PAH, particle number concentration and temperature. This is explored in the following section with a series of simulations using a fixed total concentration of PAHs in air of 5×10^5 cm^{-3} and particles with a diameter of 50 nm.

3.2.1 PAH molecular structure

3.2.2 Particle number concentration

The effect of varying the particle number concentration N_p on the equilibration timescale shows a distinct behavior (Fig. 3a): τ_{eq} is particle number-independent at lower N_p, while τ_{eq} is particle number-dependent at higher N_p. The equilibration timescales of the less strongly adsorbed PAHs including anthracene, fluoranthene and pyrene are not significantly affected by particle number concentration until a fairly high threshold particle number concentration is achieved ($\approx 10^5$, 10^4 and 10^4 $\mathrm{particles\,cm}^{-3}$, respectively).

Once the threshold particle number concentration is reached, a linear relationship in the double logarithmic dependence of equilibration timescale and particle number concentration emerges. The more strongly adsorbed PAHs, chrysene, benzo(e)pyrene and benzo(a)pyrene, reach this limit at a much lower N_p ($\approx 10^2$ $\mathrm{particles\,cm}^{-3}$). This can be understood when looking at Fig. 3b, in which the equilibration timescale of pyrene is shown together with the individual timescales of desorption τ_{des} (gray dashed line, calculated with Eq. 6) and adsorption τ_{ads} (gray dotted line, calculated with Eq. 7).

$$\tau_{des} = \frac{1}{k_{des}} = Ae^{-E_A/RT} \tag{6}$$

$$\tau_{ads} = \frac{1}{k_{ads}} = \frac{1}{(1-\theta_s)\alpha_{s,0}d_p^2\pi N_p\omega/4} \approx \frac{1}{\alpha_{s,0}d_p^2\pi N_p\omega/4} \tag{7}$$

In the limit of an adsorbate-free surface, adsorption and desorption are first-order processes with respect to the near-surface gas and surface concentrations of PAH respectively and can therefore be described with rate coefficients k_{ads} (s^{-1}) and k_{des}

https://doi.org/10.5194/acp-2020-1000
Preprint. Discussion started: 7 October 2020

Atmospheric Chemistry and Physics Discussions

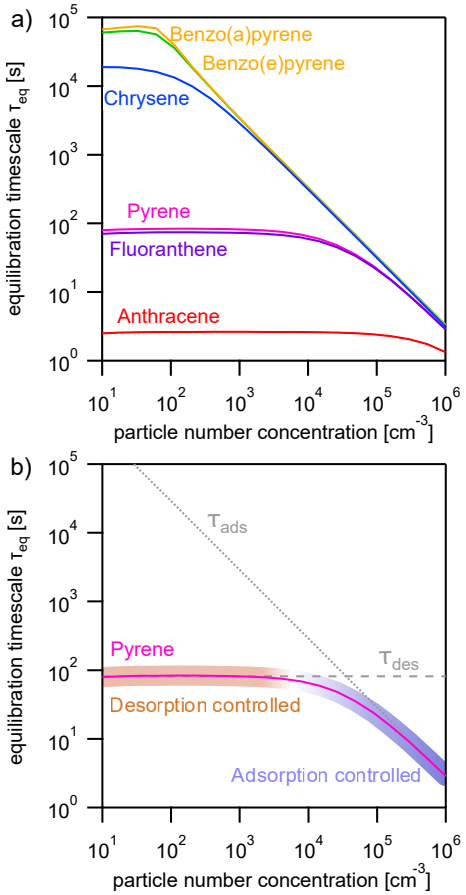

Figure 3. a) Equilibration timescale τ_{eq} for different PAHs as a function of particle number concentration at a constant temperature ($T = 298$ K). b) Comparison of the equilibration timescale of pyrene to the timescales of adsorption τ_{ads} and desorption τ_{des}, highlighting the transition between adsorption-controlled and desorption-controlled behavior.

(s^{-1}). The desorption timescale τ_{des} depends on the Arrhenius factor A and the activation energy for desorption from the aerosol particle surface (E_A), the gas constant R and temperature T. The adsorption timescale τ_{ads} depends on the surface accommodation coefficients on an adsorbate-free substrate $\alpha_{s,0}$, the particle number concentration N_p, the surface area of a single aerosol particle $d_p^2\pi$ with diameter d_p and the mean thermal velocity ω. The surface coverage θ_s is very small for typical particle number concentrations and will therefore be neglected in the following. In general, τ_{eq} can be approximated as a function of both timescales according to Eq. 8 (see appendix for details of the terms and derivation). This approximation holds as long as gas diffusion is sufficiently fast and does not limit equilibration.

$$\tau_{eq} \approx \frac{1}{k_{des} + k_{ads}} = \frac{1}{Ae^{-E_A/RT} + \alpha_{s,0} d_p^2 \pi N_p \omega / 4} \tag{8}$$

https://doi.org/10.5194/acp-2020-1000
Preprint. Discussion started: 7 October 2020

Atmospheric Chemistry and Physics Discussions

If one process (desorption or adsorption) dominates the behavior of τ_{eq}, the system can be said to fall into an *adsorption-controlled* regime (highlighted for pyrene with red shading) or a *desorption-controlled* regime (highlighted with blue shading). A multi-step process in which mass is lost and transferred in one direction can be described analagously to a series of resistors in an electrical circuit and the term *limiting* can be used to describe the slowest step. In contrast, the gas-particle partitioning system is a reversible system in which mass is transferred in both directions and the relative rates of these mass-transfer processes determine the position of equilibrium. We therefore observe in Fig. 3b (and also Fig. 4b) that the equilibration time is determined primarily by the fastest process (i.e. that with the shortest timescale). We therefore adopt the term *controlled* to characterize this behavior.

In the low particle number concentration limit, the system is in a *desorption-controlled* regime and the equilibration timescale is thus strongly influenced by strength of the PAH-soot interaction, which explains the large differences in equilibration timescale between PAHs in Fig. 3a. In the high particle number concentration limit, the equilibration timescale is determined primarily by the adsorption of PAH onto particles from the near-surface gas phase and is therefore independent of PAH type as can be seen from the convergence of curves in Fig. 3a. The equilibration timescale here coincides with the adsorption timescale τ_{ads} and the system is in an *adsorption-controlled* regime. The transition between both regimes occurs where τ_{ads} intersects τ_{des} and coincides with the point $\Phi_{eq} = 0.5$. At this specific point, equal amounts of PAH are in the gas and particle phases and the timescales of desorption and adsorption contribute equally to the equilibration time.

As surface coverages θ_s are very small and PAHs generally have surface accommodation coefficients on an adsorbate-free substrate of $\alpha_{s,0} = 1$ (Julin et al., 2014), we find in this study a special case of the *adsorption-controlled* regime where molecular collision of gas molecules is the sole controller of partitioning. For adsorbates with lower $\alpha_{s,0}$, the adsorption timescale would be longer and the system may be in the *desorption-controlled* regime.

3.2.3 Temperature

The effect of varying temperature T on the equilibration timescale shows a behavior similar to the one seen for the particle number concentration (Fig. 4a): τ_{eq} is temperature-independent at low T, while τ_{eq} is temperature-dependent and begins to decrease at higher T. For the most weakly adsorbed PAH anthracene, τ_{eq} begins decreasing at 240 K towards higher T and at 298 K is already less than 5 s. The equilibration timescales for fluoranthene and pyrene begin decreasing at $\approx$ 260 K and at 298 K are both less than 100 s. Strongly adsorbed PAHs including chrysene, benzo(e)pyrene and benzo(a)pyrene do not undergo a significant change in equilibration timescale in the investigated temperature range.

Again, the *adsorption-controlled* and *desorption-controlled* regimes explain this behavior (Fig. 4b). Between 210 K and 240 K, PAH molecules possess little kinetic energy and are prevented from escaping into the gas phase, thus exhibiting long desorption lifetimes (Fig. A3) and high equilibrium particulate fractions (Fig. A2b). As most PAH is adsorbed on the surface of aerosol particles, molecular collision determines equilibration time. The system is in the *adsorption-controlled* regime, highlighted for pyrene with blue shading and signified by the coincidence with the adsorption timescale τ_{ads} (gray dotted line). The number of collisions between gas-phase PAHs and particles slightly increases as the thermal velocity increases, but this effect is much smaller compared to the effect of temperature increase on desorption rates. Note that the surface

https://doi.org/10.5194/acp-2020-1000
Preprint. Discussion started: 7 October 2020

Atmospheric Chemistry and Physics Discussions

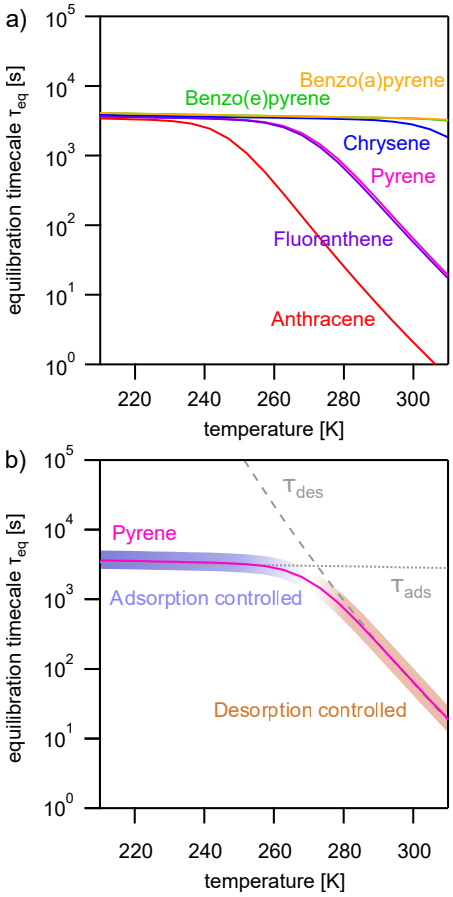

Figure 4. a) Equilibration timescale τ_{eq} for different PAHs as a function of temperature at a constant particle number concentration ($N_p = 1 \times 10^3$ particles cm^{-3}). b) Comparison of the equilibration timescale of pyrene to the timescales of adsorption τ_{ads} and desorption τ_{des}, highlighting the transition between *adsorption-controlled* and *desorption-controlled* behavior.

accommodation coefficient is assumed to be temperature-independent in this study. Overall, upon increase in temperature, the desorption process becomes increasingly important. At high temperature, the system is in the *desorption-controlled* regime, highlighted for pyrene with red shading in Fig. 4b and signified by the coincidence with the timescale of desorption τ_{des} (gray dashed line).

3.3 Interplay of multiphase chemistry and partitioning

Chemical reactions with O_3 and OH are important loss processes for PAHs. If the rate of chemical loss is fast relative to gas-particle partitioning, the gas-particle distribution may be perturbed from its equilibrium state (cf. Fig. 2, cases B and C). This effect is exemplified for pyrene by including surface chemistry with O_3 (0, 1, 10 and 100 ppb) or gas-phase and surface chemistry with OH (0, 0.01, 0.1 and 1 ppt) in the model. 10 ppb is representative of surface background O_3 concentrations

https://doi.org/10.5194/acp-2020-1000
Preprint. Discussion started: 7 October 2020

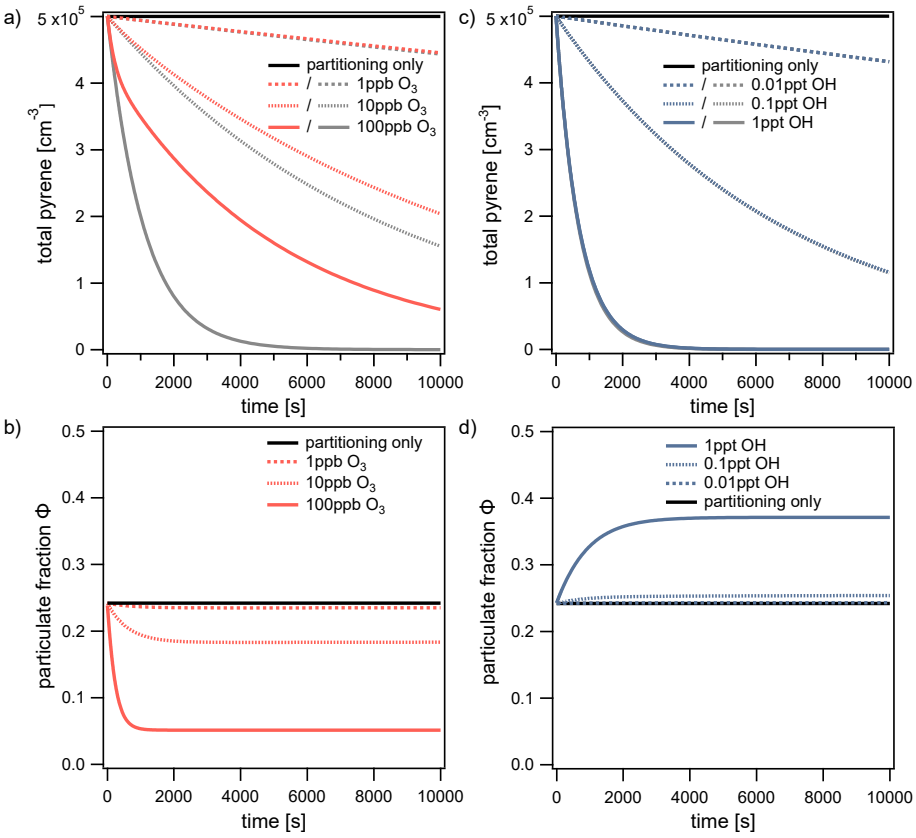

Figure 5. The total pyrene concentration (gas phase + particle phase) with respect to time at different concentrations of a) O_3 and b) OH. O_3 reacts only with pyrene on the surface of particles, whereas OH reacts with pyrene in simultaneous gas and surface reactions. The total concentration of pyrene determined in a fictional scenario with infinitely fast partitioning is shown with gray lines. For the same simulations, the particulate fraction of pyrene with respect to time is shown: c) O_3 and d) OH. The equilibrium particulate fraction Φ_{eq} is shown with a black line.

(Vingarzan, 2004), while 100 ppb O_3 is characteristic of concentrations at more polluted sites (Wang et al., 2017). An OH concentration of 0.01 ppt is representative of concentrations measured at night (Geyer et al., 2003), while 0.1 ppt is representative of daytime concentrations (Stone et al., 2012) and 1 ppt is an upper limit only encountered in highly polluted conditions (Hofzumahaus et al., 2009) and smoke plumes (Hobbs et al., 2003). We employ the following conditions in the pyrene-soot system: $T = 280$ K, N_p = 1×10^3 particles cm^{-3}, d_p = 50 nm. At the start of the simulation, the initial total concentration of pyrene (5×10^5 cm^{-3}) is distributed between the gas and particle phases according to the particulate fraction expected at equilibrium (i.e. $\Phi_0 = \Phi_{eq} = 0.24$). The kinetic rate coefficients for all reactions are given in Sect. 2.2. Oxidant concentrations are fixed during simulations.

https://doi.org/10.5194/acp-2020-1000
Preprint. Discussion started: 7 October 2020

Atmospheric Chemistry and Physics Discussions

3.3.1 Non-equilibrium effects on chemical lifetime and particulate fraction

Figure 5a shows the decrease in the total (gas + particle) concentration of pyrene at different O_3 concentrations. The chemical lifetime of pyrene is determined by calculating the time needed for the concentration to reach $1/e$ (i.e. $\approx$ 36.8 %) of its initial value. As the concentration of O_3 increases from 1 ppb to 10 ppb and 100 ppb, the chemical lifetime of pyrene subsequently decreases to 23.9 h, 3.1 h and 1.2 h, respectively. It is informative to compare these chemical lifetimes to those calculated by assuming partitioning is infinitely fast (i.e. the particulate fraction is fixed to Φ_{eq} during simulations). In this fictional scenario, the lifetimes of pyrene are significantly shorter at 23.1 h, 2.4 h and 0.3 h and correspond to decreases of 3 %, 23 % and 75 %, respectively. This comparison demonstrates that partitioning and chemical loss are closely interlinked. In this specific case, slow partitioning prolongs the lifetime of pyrene.

This effect can be understood by observing the change in particulate fraction over time during each of the simulations (Fig. 5b). As each simulation proceeds, the particulate fraction Φ drops below the equilibrium particulate fraction Φ_{eq} and eventually reaches a quasi-steady state Φ_{qs}. At O_3 concentrations of 10 ppb and 100 ppb, the particulate fractions reach values of $\Phi_{qs} = 0.18$ and 0.05, respectively. This effect can be explained by slow partitioning: chemical loss reduces the surface concentration of pyrene faster than its replenishment from the gas phase (non-equilibrium case C in Fig. 2). In the quasi-steady state, chemical loss and repartitioning are balanced. Importantly, both values differ significantly from Φ_{eq}. In contrast, when the O_3 concentration is low enough (1 ppb) the particulate fraction remains approximately equal to its value at equilibrium ($\Phi \approx \Phi_{eq} = 0.24$). At this O_3 concentration, the rate of partitioning is sufficiently high so that pyrene lost from the particle surface can be fully replenished from the gas phase (equilibrium case A in Fig. 2). Hence, non-equilibrium behavior increases with oxidant concentration.

Figure 5c shows the decrease in total concentration of pyrene due to the simultaneous gas and surface reactions with OH. The lifetimes of pyrene with OH concentrations of 0.01 to 0.1 and 1 ppt, are 18.9 h, 1.9 h and 0.2 h, respectively. Nearly identical lifetimes are obtained if partitioning is assumed to be infinitely fast, thus indicating that non-equilibrium effects on chemical lifetime are insignificant for this system. Figure 5d shows that in contrast to the behavior of the O_3 system, the highest concentration of OH perturbs the particulate fraction to a quasi-steady state above its equilibrium value. The particulate fraction reaches a quasi-steady state with a value of $\Phi_{qs} = 0.37$ at 1 ppt OH. Although chemical loss takes in both phases simultaneously, the turnover of pyrene is higher in the gas phase. The particulate fraction thus increases, characteristic of the non-equilibrium case B in Figure 2. At lower concentrations of OH, the extent of the perturbation becomes only slight ($\Phi_{qs} = 0.25$ at 0.1 ppt) and eventually disappears (0.01 ppt in Fig. 5d). Hence, non-equilibrium effects on particulate fraction can be significant, even if they were insignificant for chemical lifetime. This is due to the short reaction timescale of the OH-pyrene system compared to its partitioning timescale: pyrene reaches $1/e$ of its initial concentration before the quasi-steady state is established.

https://doi.org/10.5194/acp-2020-1000
Preprint. Discussion started: 7 October 2020

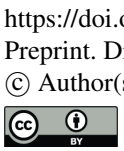

Atmospheric Chemistry and Physics Discussions

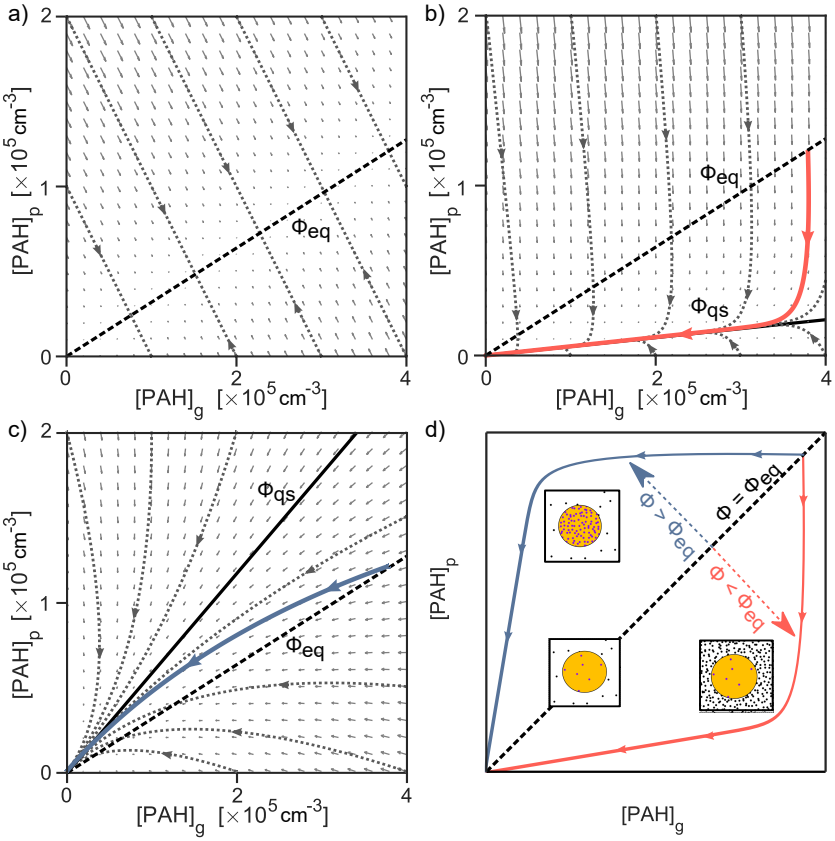

Figure 6. The interplay of partitioning and chemistry illustrated as simulated trajectories in the phase space of gas- and particle-phase concentrations, $[PAH]_g$ and $[PAH]_p$, of pyrene. a) partitioning only, b) partitioning and chemical loss from the particle phase due to surface reaction with O_3 (100 ppb, red solid line), c) partitioning and chemical loss from the gas and particle phase due to reaction with OH (1 ppt, blue solid line), and d) comparison to schematics in Fig. 2. The direction of each small gray vector arrow indicates the extent to which pyrene is being lost or transferred between phases, and its length is proportional to the rate of change. The nullcline representing equilibrium particulate fraction in panel a) ($\Phi_{eq} = 0.24$, black dashed line) is shown in panels b) and c), alongside the respective slow manifold representing the quasi-steady-state particulate fraction (Φ_{qs}, solid black line).

3.3.2 Visualization of non-equilibrium effects with phase portraits

The dynamic behavior of the system may be visualized as a trajectory in the phase space of gas-phase and particle-phase pyrene concentrations, $[PAH]_g$ and $[PAH]_p$ (Fig. 6). At every point in the phase portrait, a vector illustrates how the system would change with time. Here, the direction of each vector arrow indicates the extent to which pyrene is being lost or transferred between phases, and its length indicates the rate of change. The exact characteristics of the phase portrait depend on temperature, available particle surface area, the strength of the PAH-soot interaction and the rate of the chemical reactions

https://doi.org/10.5194/acp-2020-1000
Preprint. Discussion started: 7 October 2020


Atmospheric Chemistry and Physics Discussions

involved. For a system where pyrene partitions without chemical loss, all trajectories converge onto a central line at which the system stops changing, known in mathematics as the nullcline (Fig. 6a). This line represents the point of gas-particle partitioning equilibrium. The slope of the line represents the dimensionless gas-particle partitioning coefficient K_{p}, from which the equilibrium particulate fraction Φ_{eq} can be obtained (Eq. 9).

$$[\mathrm{PAH}]_{\mathrm{p}} = K_{\mathrm{p}}[\mathrm{PAH}]_{\mathrm{g}} = \frac{\Phi_{\mathrm{eq}}}{1-\Phi_{\mathrm{eq}}}[\mathrm{PAH}]_{\mathrm{g}} \tag{9}$$

As seen previously, chemical reactions may cause perturbation of the partitioning equilibrium. Such a perturbation would be indicated by deviation of trajectories from the nullcline in the phase portrait. The difference between perturbed and equilibrium system is depicted for $[\mathrm{O_3}] = 100\ \mathrm{ppb}$ in Fig. 6b. The vector field fundamentally changes and the trajectory of an exemplary simulated system (red solid line) does not converge to the nullcline obtained in Fig. 6a, despite starting at equilibrium conditions Φ_{eq} (shown as black dashed line for reference). Instead, the trajectory converges onto a central trajectory termed the slow manifold (Fraser, 1988). All trajectories in this system (represented with gray dotted lines) converge towards this manifold, irrespective of initial conditions. After approaching the slow manifold, the trajectory proceeds towards the origin (i.e. full depletion of pyrene) with a constant slope. This constant slope indicates that a constant quasi-steady-state particulate fraction $\Phi_{\mathrm{qs}} = 0.05$ has been reached. The deviation of the nullcline (Fig. 6a) and the slow manifold (Fig. 6b) can be used to indicate the extent of non-equilibrium effects in a multiphase chemical reaction system. For example, Fig. 6c shows that for the reaction with $1\ \mathrm{ppt}$ OH, the discrepancy between the simulation trajectory and the partitioning nullcline is much smaller due to simultaneous loss in the gas and particle phases. The slow manifold here runs above the partitioning nullcline and is reached only just before all pyrene is consumed (compare solid blue lines in Fig. 5). Fig. 6d shows how the nullcline and the slow manifolds above or below it can be interpreted using the diagrams in Fig. 2.

3.4 Implications for chemical transport models (CTMs)

In the previous sections, an explicit, coupled model of partitioning and chemistry is used. This means that mass-transport and chemical-loss processes are simultaneously evaluated in a set of differential equations. Hereon, this is referred to as the explicit-coupled approach (EC). As the explicit-coupled approach is computationally expensive, CTMs often treat the partitioning and chemical loss of PAHs separately using operator splitting (Brasseur and Jacob, 2017). Instantaneous equilibration (IE) is one type of operator-splitting approach: at each model time step (Δt), the gas-particle distribution of PAH is reset to the partitioning equilibrium (estimated by temperature, particle number concentration, PAH, and particle type) and chemical loss is then further integrated separately, starting from the newly established equilibrium. Time steps of global and regional transport models used to study PAH are typically around $15\ \mathrm{min}$ (Galarneau et al., 2014) or $30\ \mathrm{min}$ (Sehili and Lammel, 2007).

3.4.1 Influence of model time step length

The solution obtained using the IE approach can differ from the EC solution. Using the surface reaction of $\mathrm{O_3}$ ($100\ \mathrm{ppb}$) with pyrene in the particle phase, we demonstrate that the magnitude and sign of this difference varies between $\Delta t = 4\ \mathrm{min}$,

https://doi.org/10.5194/acp-2020-1000
Preprint. Discussion started: 7 October 2020

Atmospheric Chemistry and Physics Discussions

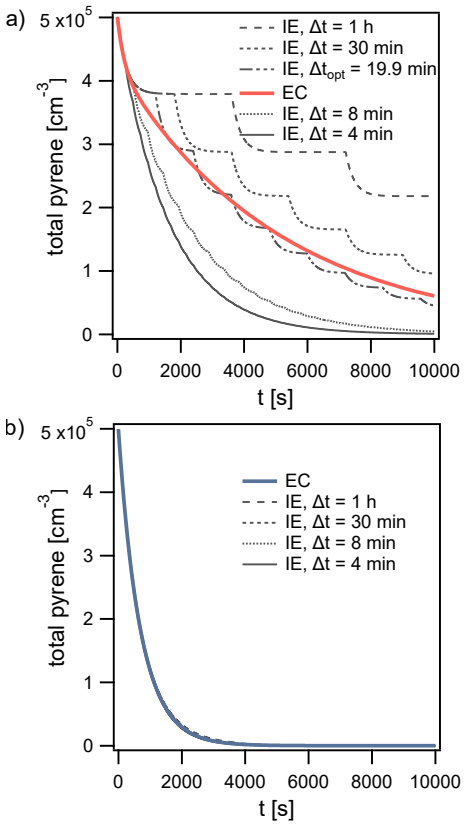

Figure 7. Time evolution of total pyrene concentration in model calculations, comparing the explicit-coupled (EC) to the operator splitting with instantaneous equilibration (IE) solution ($\Delta t = 4$ min, 8 min, 30 min and 1 h) for systems with a) surface reaction of particle-phase pyrene with 100 ppb O_3 and b) reaction of gas- and surface-bound pyrene with 1 ppt OH. The operator-splitting time step leading to the smallest deviation is depicted as Δt_{opt}.

8 min, 30 min and 1 h (Fig. 7a). The following conditions are used in the simulations: $T = 280$ K, $d_p = 50$ nm, $N_p = 1 \times 10^3$ particles cm^{-3}.

325 The lifetime of pyrene is underestimated when using time steps Δt of 4 and 8 min (Fig. 7a), but overestimated with Δt of 30 min and 1 h. In this example, an optimal time step exists, for which the deviation from EC is minimized, $\Delta t_{opt} = 19.9$ min (Fig. 7a). It is close to the equilibration timescale of gas-particle partitioning τ_{eq} of pyrene, which is around 15 min under these conditions. τ_{eq} could thus serve as initial guess for Δt_{opt}. Δt_{opt} is determined using a golden-section search optimization algorithm (Kiefer, 1953) to minimize the absolute difference between EC and IE model outputs. Of note, a deviation between
330 IE and EC and hence a dependence of the model result on the operator-splitting time step only arises if a significant departure from partitioning equilibrium occurs. Under equilibrium partitioning conditions, a range of sufficiently short Δt can describe the system accurately. In an example with OH (1 ppt) reacting with gas-phase and surface-bound pyrene, all IE calculations

https://doi.org/10.5194/acp-2020-1000
Preprint. Discussion started: 7 October 2020

Atmospheric Chemistry and Physics Discussions

produce negligible errors, irrespective of the time step used (Fig. 7b). This is due to the particulate fraction being very close to Φ_{eq} until the majority of PAH has reacted (cf. Fig. 5d).

3.4.2 Deviation from explicit-coupled (EC) approach

The discrepancy between the EC and IE solutions not only depends on the length of Δt, but also on the relative rates of partitioning and chemical loss. The discrepancy can be quantified with an error metric, E_{loss}, which can be interpreted as the relative difference in loss rates (Eq. 10). $\Delta[\text{PAH}]_{\text{EC}}(t)$ and $\Delta[\text{PAH}]_{\text{IE}}(t)$ are the accumulated losses of PAH at each time point t using EC and IE, respectively (Eqs. 11 and 12). This metric is chosen as it detects discrepancies in model solutions independent of the absolute turnover, which is important when comparing scenarios at high and low oxidant concentrations. E_{loss} ranges between -1 and 1, and is evaluated until either $t_{90\%}$ or $t = 24$ h is reached. E_{loss} is positive when the IE solution overpredicts the loss of pyrene compared to the reference EC solution, and negative when loss is underestimated.

$$E_{\text{loss}} = \frac{1}{n}\sum_{t=1}^{n}\frac{\Delta[\text{PAH}]_{\text{IE}}(t) - \Delta[\text{PAH}]_{\text{EC}}(t)}{\Delta[\text{PAH}]_{\text{EC}}(t) + \Delta[\text{PAH}]_{\text{IE}}(t)} \tag{10}$$

$$\Delta[\text{PAH}]_{\text{EC}}(t) = [\text{PAH}]_{\text{EC}}(0) - [\text{PAH}]_{\text{EC}}(t) \tag{11}$$

$$\Delta[\text{PAH}]_{\text{IE}}(t) = [\text{PAH}]_{\text{IE}}(0) - [\text{PAH}]_{\text{IE}}(t) \tag{12}$$

Figure 8 shows the extent and direction of deviation of IE from EC in a case study of PAH surface chemistry in which the desorption rate coefficient k_{des} is varied between $5{\times}10^{-8}$ and 5×10^{-1} s^{-1}, and the concentration of O_3 between 0 and 120 ppb for IE time steps of $\Delta t = 1$ min and $\Delta t = 30$ min. When $\Delta t = 1$ min (Fig. 8a), IE overestimates PAH loss compared to EC, indicated by red coloring. Deviation is largest when k_{des} is between $1{\times}10^{-4}$ and $1{\times}10^{-2}$ s^{-1}. Here, the IE time step of 1 min causes PAH to transfer onto particles at an artificially high rate. This increases the particle-phase concentration of PAH and results in faster chemical loss. The IE solution hence shows less non-equilibrium effects of slow partitioning on multiphase chemistry compared to the reference EC model. At the highest k_{des} ($> 1 \times 10^{-2}$ s^{-1}), non-equilibrium effects of slow partitioning still occur, but in the *desorption-controlled* regime (cf. Fig. 4 at 280 K) an increase in k_{des} leads to a reduction in equilibration timescale. This not only leads to weaker non-equilibrium effects of slow partitioning in the EC solution, but also to a better match between EC equilibration timescale and IE time step. Hence, the discrepancy between IE and EC approach is reduced, as evident by the more faint red coloring. At low k_{des} ($< 1{\times}10^{-5}$ s^{-1}), most PAH is located on the surface of particles at all times and re-partitioning of gas-phase PAH after depletion of particle-phase PAH is negligible. Thus, no deviation of the IE from the EC approach occurs.

In contrast, with a time step of $\Delta t = 30$ min (Fig. 8b), the IE approach generally underestimates the loss of PAH compared to the EC approach, indicated by blue coloring. The largest underestimations are found at high k_{des} and high $[O_3]_g$. Underestimation of PAH loss occurs because the re-partitioning induced by the longer IE time step of 30 min is slower than the true

https://doi.org/10.5194/acp-2020-1000
Preprint. Discussion started: 7 October 2020

Atmospheric Chemistry and Physics Discussions

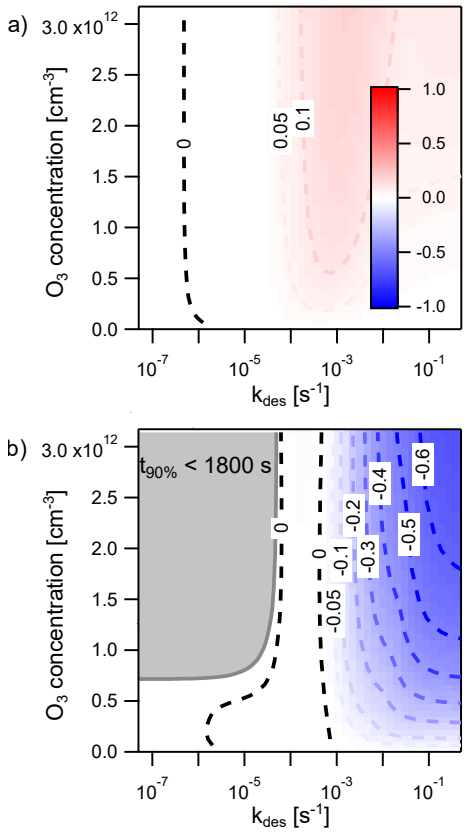

Figure 8. Discrepancy between the explicit-coupled solution EC and the operator-splitting solution IE for surface reaction of particle-phase pyrene with O_3 (100 ppb), determined with the error metric E_{loss}. Regions where IE overestimates the loss of PAH are indicated in red (0 < $E_{\text{loss}} \leq 1$) and where it underestimates PAH loss in blue (-1 $\geq E_{\text{loss}}$ < 0). The result is shown using two different operator-splitting time step lengths a) $\Delta t = 1$ min and b) $\Delta t = 30$ min. The dark gray area indicates the conditions under which the time taken for total pyrene to deplete by 90 % ($t_{90\%}$) is less than a single operator-splitting time step.

equilibration rate in the EC model. In this scenario, the IE approach thus leads to stronger non-equilibrium effects of slow partitioning compared to the EC model. When the equilibration timescale becomes shorter, at high k_{des} ($> 1 \times 10^{-2}$ s^{-1}), the discrepancy between the IE and the EC solution further increases, especially at high $[O_3]_g$. Notably, at $k_{\text{des}} \approx 1 \times 10^{-4}$ s^{-1}, the IE approach slightly overestimates loss of PAH at high $[O_3]_g$. This is due to the EC equilibration timescale dropping below the equivalent of $\Delta t = 30$ min just before non-equilibrium effects of slow partitioning vanish at the lowest k_{des}. In between, a zero contour (labeled '0') and hence no deviation between both methods occurs when $k_{\text{des}} \approx 1 \times 10^{-3}$ s^{-1}. Here, the IE approach matches the EC equilibration timescale by alternatingly underestimating and overestimating the concentration of PAH at different points of the simulation and a cancellation of errors occurs (cf. Fig. 7a). This case is distinct from the left zero contour at $k_{\text{des}} \approx 5 \times 10^{-5}$ s^{-1}, in which departure from equilibrium does not occur and both methods return truly identical results (compare Figs. A5a and A5c). Another region exists: for $k_{\text{des}} < 1 \times 10^{-4}$ s^{-1}, the simulation proceeds for less than 30 min

https://doi.org/10.5194/acp-2020-1000
Preprint. Discussion started: 7 October 2020


Atmospheric Chemistry and Physics Discussions

and therefore less than one IE time step is evaluated (Fig. A5). In this region partitioning effectively does not take place and we chose not to report the numerical value of E_{loss}.

E_{loss} is negligibly small when the concentration of $[\text{OH}]_{\text{g}}$ is varied between 0 and 0.5 ppt with reaction in both the gas phase and on the surface of particles (Fig. A4a). Unlike the example with O_3, PAH loss rates due to reaction with OH in each phase are similar enough that Φ is not perturbed far from Φ_{eq} under these conditions. Often, in chemical transport models only the gas-phase reaction of PAH with OH is included. Varying the concentration of OH between 0 and 0.5 ppt with reaction in the gas phase only causes IE to overestimate the loss of PAH (red area, Fig. A4b).

4 Atmospheric implications

This study shows that the chemical loss of polycyclic aromatic hydrocarbons (PAHs) and their partitioning between the gas and particle phases are closely interlinked. The equilibration timescales of adsorptive partitioning are quantified for six PAHs on the surface of soot. Our model predicts that equilibration timescales range from seconds to hours depending on temperature, available particle surface area and molecular structure of the PAH. We highlight the molecular processes governing this timescale with two regimes: *adsorption-controlled* and *desorption-controlled* partitioning.

Soot constitutes only a fraction of total ambient aerosol particles (Pöschl, 2005). Thus, a logical next step will be to investigate how equilibration timescales vary for other types of particle surfaces. For example, given the weaker desorption energies of PAHs such as anthracene on the surface of NaCl (75.3 kJ mol^{-1}) compared to soot (87.9 kJ mol^{-1}; Chu et al., 2010), one would expect equilibration timescales on NaCl to be shorter.

On other particle types, PAHs molecules can undergo absorptive partitioning by diffusing through surface layers into the bulk of the particle. For secondary organic aerosol (SOA), the particle phase state influences the rates of condensation and evaporation (Shiraiwa and Seinfeld, 2012). Equilibration timescales for PAHs are therefore also expected to be dependent on particle composition and humidity. Depending on the controlling regime, it might be expected that absorption lengthens the equilibration timescale compared to adsorption on a solid surface. The complex interplay of partitioning and reaction in the gas and particle phases plays a critical role in the growth of SOA particles (Shiraiwa et al., 2013; Berkemeier et al., in review, 2020) and departure from partitioning equilibrium adds to this complexity (Cappa and Wilson, 2011). However, the role of bulk diffusion in determining equilibration timescales is beyond the scope of this study and will be investigated in a follow-up study that builds on the framework provided here.

Chemical reaction of pyrene with O_3 on the surface of particles perturbs the particulate fraction from partitioning equilibrium at atmospherically-relevant oxidant concentrations. As the extent of this perturbation increases with concentration of O_3, the largest deviations from equilibrium particulate fraction are likely to take place in the most polluted air. The reaction of pyrene with OH in both phases results in much smaller perturbations. In general, the biggest deviations from equilibrium particulate fraction are expected for low-volatility PAHs when atmospheric conditions induce slow partitioning (i.e. cold temperatures and low particle number concentrations). Other chemical-loss processes may also be important for PAHs such as the reaction with NO_3 in both the gas phase (Zhang et al., 2014) and the particle phase (Gross and Bertram, 2008), as well as aqueous-phase

https://doi.org/10.5194/acp-2020-1000
Preprint. Discussion started: 7 October 2020


Atmospheric Chemistry and Physics Discussions

photodegradation processes (Fasnacht and Blough, 2002). These reactions must eventually be studied simultaneously in order to establish whether loss in both phases balances out or whether perturbation from equilibrium takes place.

It should also be noted that while in this study simulations involving chemical loss are initialized at the point of equilibrium ($\Phi_0 = \Phi_{eq}$), in reality PAHs may be emitted in a state far from partitioning equilibrium. Depending on the prevailing loss processes, such an effect could both enhance or inhibit perturbations from equilibrium.

Non-chemical loss processes, such as dry and wet deposition remove PAHs from the gas and the particle phases at different rates and may also cause perturbations from partitioning equilibrium. The fastest loss processes, i.e. those operating at the shortest timescales, will cause the greatest perturbations. In the case of polybrominated diphenyl ethers (PBDEs), Li et al. (2015) attempted to include the effect of loss by deposition on partitioning and derived an equation for the partitioning coefficient assuming a steady state rather than equilibrium. However, given that for PAHs the estimated lifetimes due to dry deposition (1 to 14 days) and wet deposition (5 to 15 months; Škrdlíková et al., 2011) are much longer than lifetimes due to chemical loss (in this study less than 24 h), chemical loss is expected to be the loss process that is most likely to perturb the partitioning equilibrium.

The methodology described in this study is universally applicable to semi-volatile compounds on solid surfaces if mass-transfer parameters and chemical reaction rate coefficients are available. In some cases it may be necessary to estimate these parameters. In quantum mechanical calculations, graphene surfaces could be used as a model for soot and desorption energies. Such values are already available for PBDEs (Ding et al., 2014) and other small organic molecules (Lazar et al., 2013).

It has to be noted that an explicitly coupled solution of partitioning and chemical loss is computationally too expensive for inclusion in typical regional and global CTMs. Hence, alternative algorithms would be highly anticipated. Knowledge about the position of the partitioning steady state in the presence of chemical loss (as indicated by the slow manifold that can be visualized in a phase portrait of gas and particle phase concentrations) could be used to develop such a method for global and regional models.

https://doi.org/10.5194/acp-2020-1000
Preprint. Discussion started: 7 October 2020

Atmospheric Chemistry and Physics Discussions

Appendix A: Kinetic model

The flux of PAH molecules from the gas phase to the near-surface gas phase J_{diff} with concentrations $[\text{PAH}]_{\text{g}}$ and $[\text{PAH}]_{\text{gs}}$, respectively, is calculated with Eq. A1.

$$J_{\text{diff}} = 2\pi(d_{\text{p}} + 2\lambda)D_{\text{g}}([\text{PAH}]_{\text{g}} - [\text{PAH}]_{\text{gs}}) \tag{A1}$$

The gas-phase diffusion coefficient D_{g} is fixed at 0.06 $\text{cm}^2\,\text{s}^{-1}$ for all PAH compounds, based on measurements for anthracene and pyrene in nitrogen (Siddiqi et al., 2009). d_{p} is the diameter of aerosol particles. The mean free path λ is defined in Eq. A2.

$$\lambda = \frac{3D_{\text{g}}}{\omega} \tag{A2}$$

The mean thermal velocity of a molecule ω depends on temperature T and its molar mass M (Eq. A3).

$$\omega = \sqrt{\frac{8RT}{\pi M}} \tag{A3}$$

The adsorption flux J_{ads} of molecules from the near-surface gas phase to the particle phase is described using Eq. A4.

$$J_{\text{ads}} = \alpha_{\text{s},0}(1 - \theta_{\text{s}})J_{\text{coll}} \tag{A4}$$

The surface accommodation coefficient on an adsorbate-free substrate $\alpha_{\text{s},0}$ describes the probability that a molecule adsorbs upon collision with an adsorbate-free aerosol particle and for PAH molecules is assumed to be $\alpha_{\text{s},0} = 1$ (Julin et al., 2014). The total sorption layer coverage θ_{s} is calculated as the sum of the fractional coverages of PAH and O_3, θ_{PAH} and θ_{O3}, respectively (Eq. A5). θ_{PAH} and θ_{O3} are calculated using the surface concentrations $[\text{PAH}]_{\text{s}}$ and $[O_3]_{\text{s}}$, and molecular cross sections σ_{PAH} and σ_{O3} of PAH and O_3, respectively (Eq. A6). In order to estimate σ, each benzene-like ring of a PAH molecule is assumed to occupy 2×10^{-15} cm^2. The collision flux J_{coll}, i.e. the flux of molecules colliding with the surface, is defined in Eq. A7.

$$\theta_{\text{s}} = \theta_{\text{PAH}} + \theta_{\text{O3}} \tag{A5}$$

$$\theta_{\text{PAH}} = \sigma[\text{PAH}]_{\text{s}} \tag{A6}$$

$$J_{\text{coll}} = \frac{[\text{PAH}]_{\text{gs}}\omega}{4} \tag{A7}$$

https://doi.org/10.5194/acp-2020-1000
Preprint. Discussion started: 7 October 2020

Atmospheric Chemistry and Physics Discussions

The temperature dependent desorption flux (J_{des}) due PAH molecules evaporating from the surface of an aerosol particle depends on the rate coefficient for desorption (k_{des}) and the surface concentration of PAH $[\mathrm{PAH}]_{\mathrm{s}}$ (Eq. A8).

$$J_{\mathrm{des}} = k_{\mathrm{des}}[\mathrm{PAH}]_{\mathrm{s}} \tag{A8}$$

k_{des} depends on the Arrhenius factor (A) and the activation energy for desorption from the aerosol particle surface (E_{A}; Eq. A9).

$$k_{\mathrm{des}} = Ae^{-E_{\mathrm{A}}/RT} \tag{A9}$$

The temperature dependence of the desorption rate coefficient was previously determined for seven PAHs on fresh kerosene soot (Guilloteau et al., 2008, 2010) and the obtained parameters are implemented in this model (see Table A1). These activation energies of desorption for PAHs on soot are consistent with those obtained theoretically on pure graphene (Lechner and Sax, 2014) and coronene (Kubicki, 2006). It should also be noted that different types of soots can have different effects on gas-particle partitioning (Mader and Pankow, 2002) and more aged soot may have a reduced affinity for PAH. Despite the simplifications of this model, we aim to provide a basis to which further complexity can be added.

Irreversible reactions between pyrene and either $\mathrm{O_3}$ on the surface of aerosol particles or OH in the gas phase and on the surface of aerosol particles are investigated with the model. The equations of mass-transport for $\mathrm{O_3}$ are identical to those for PAH and the corresponding parameters are reported in Tables A1 and A2. As the uptake of OH is considered to proceed via an Eley-Rideal mechanism, the diffusion of OH from the gas-phase to the near-surface gas phase is treated using a gas-phase diffusion correction factor $C_{\mathrm{g,OH}}$ (Eq. A10). The full equation for $C_{\mathrm{g,OH}}$ can be found in Eq. 14 of Pöschl et al. (2007).

$$[\mathrm{OH}]_{\mathrm{gs}} = C_{\mathrm{g,OH}}[\mathrm{OH}]_{\mathrm{g}} \tag{A10}$$

The rate of PAH loss from the particle surface due to chemical reaction with OH $L_{\mathrm{s,OH}}$ depends on probability $\gamma_{\mathrm{OH,PAH}}$ that reaction occurs following collision of OH with PAH on the particle surface (Eq. A11). The rate of gas-phase PAH loss by OH $L_{\mathrm{g,OH}}$ and the rate of PAH loss from the surface due to reaction with $\mathrm{O_3}$ $L_{\mathrm{s,O3}}$ are defined by Eq. A12 and Eq. A13, respectively. Further details of these reactions and their parameters can be found in section 2.2.

$$L_{\mathrm{s,OH}} = \gamma_{\mathrm{OH,PAH}}\theta_{\mathrm{PAH}}J_{\mathrm{coll,OH}} \tag{A11}$$

$$L_{\mathrm{g,OH}} = k_{\mathrm{g}}[\mathrm{PAH}]_{\mathrm{g}}[\mathrm{OH}]_{\mathrm{g}} \tag{A12}$$

$$L_{\mathrm{s,O3}} = k_{\mathrm{s}}[\mathrm{PAH}]_{\mathrm{s}}[\mathrm{O_3}]_{\mathrm{s}} \tag{A13}$$

https://doi.org/10.5194/acp-2020-1000
Preprint. Discussion started: 7 October 2020

Atmospheric Chemistry and Physics Discussions

Appendix B: Derivation of equation for equilibration time

An approximate equation for equilibration time τ_{eq} (s) is obtained analytically using the relaxation time of a simple reversible reaction (Bernasconi, 1976). The equation approximates the numerically-obtained results from the kinetic model and is derived by assuming that gas-particle partitioning can be described as two first-order processes, adsorption and desorption, with rate coefficients k_{des} (s^{-1}) and k_{ads} (s^{-1}). We find there is good agreement between the numerically-obtained results and the approximate equation as long as the gas diffusion flux J_{diff} does not significantly affect gas-particle partitioning (i.e. $[PAH]_g \approx [PAH]_{gs}$) and surface crowding effects do not significantly inhibit adsorption of PAH onto the surface (i.e. θ_s is small). The equilibration timescale of PAHs predicted by the equation are within 10 % of the numerically-obtained timescale among our test conditions ($\geq 10^3$ particles cm^{-3}, 210 K $\geq T \geq$ 310 K). For a gas-phase $[PAH]_g$ (cm^{-3}) and particle-phase concentration $[PAH]_p$ (cm^{-3}), the rate equation can be expressed in the following way

$$\frac{d[PAH]_g}{dt} = -\frac{d[PAH]_p}{dt} = k_{des}[PAH]_p - k_{ads}[PAH]_g. \quad \text{(B1)}$$

At equilibrium, the concentration of PAH in the gas and particle phases is $[PAH]_{g,eq}$ and $[PAH]_{p,eq}$. As there is no net transfer in mass

$$\frac{d[PAH]_g}{dt} = k_{des}[PAH]_{p,eq} - k_{ads}[PAH]_{g,eq} = 0. \quad \text{(B2)}$$

The concentrations of PAH in the gas and particle phases can therefore be expressed as a displacement from their values at equilibrium, $\Delta[PAH]_g$ and $\Delta[PAH]_p$ (Eq. B3 and Eq. B4).

$$[PAH]_g = [PAH]_{g,eq} + \Delta[PAH]_g \quad \text{(B3)}$$

$$[PAH]_p = [PAH]_{p,eq} + \Delta[PAH]_p \quad \text{(B4)}$$

Substitution of $\Delta[PAH]_g = -\Delta[PAH]_p = x$ into Eq. B3 and Eq. B4 allows the displacements from equilibrium to be expressed in terms of a single variable x (Eq. B5 and Eq. B6).

$$[PAH]_g = [PAH]_{g,eq} + x \quad \text{(B5)}$$

$$[PAH]_p = [PAH]_{p,eq} - x \quad \text{(B6)}$$

https://doi.org/10.5194/acp-2020-1000
Preprint. Discussion started: 7 October 2020

Atmospheric Chemistry and Physics Discussions

Insertion of Eq. B5 and Eq. B6 into Eq. B2 gives

$$\frac{\mathrm{d}[\mathrm{PAH}]_\mathrm{g}}{\mathrm{d}t} = +k_\mathrm{des}([\mathrm{PAH}]_\mathrm{p,eq} - x) - k_\mathrm{ads}([\mathrm{PAH}]_\mathrm{g,eq} + x) = 0. \tag{B7}$$

Expansion of brackets, followed by insertion of Eq. B2 gives

$$\frac{\mathrm{d}[\mathrm{PAH}]_\mathrm{g}}{\mathrm{d}t} = -(k_\mathrm{des} + k_\mathrm{ads})x = 0. \tag{B8}$$

Insertion of Eq. B5 into Eq. B8 gives Eq. B9, then noting that $\mathrm{d}[\mathrm{PAH}]_\mathrm{g,eq}/\mathrm{d}t = 0$ gives Eq. B10.

$$\frac{\mathrm{d}([\mathrm{PAH}]_\mathrm{g,eq} + x)}{\mathrm{d}t} = \frac{\mathrm{d}[\mathrm{PAH}]_\mathrm{g,eq}}{\mathrm{d}t} + \frac{\mathrm{d}x}{\mathrm{d}t} = -(k_\mathrm{des} + k_\mathrm{ads})x = 0 \tag{B9}$$

$$\frac{\mathrm{d}x}{\mathrm{d}t} = -(k_\mathrm{des} + k_\mathrm{ads})x. \tag{B10}$$

Both sides are integrated (Eq. B11) and the equation rearranged (Eq. B12).

$$\int_{x_0}^{x} \frac{1}{x} dt = \int_{t_0}^{t} -(k_\mathrm{des} + k_\mathrm{ads}) dt \tag{B11}$$

$$x = x_0 e^{-(k_\mathrm{des} + k_\mathrm{ads})t} \tag{B12}$$

The equilibration time τ_eq can therefore be considered the e-folding time required for the displacement x to decrease to $1/e$ of its initial value (Eq. B13).

$$\tau_\mathrm{eq} \approx \frac{1}{k_\mathrm{des} + k_\mathrm{ads}} = \frac{1}{Ae^{-E_\mathrm{A}/RT} + \alpha_\mathrm{s,0} d_\mathrm{p}^2 \pi N_\mathrm{p} \omega / 4} \tag{B13}$$

https://doi.org/10.5194/acp-2020-1000
Preprint. Discussion started: 7 October 2020

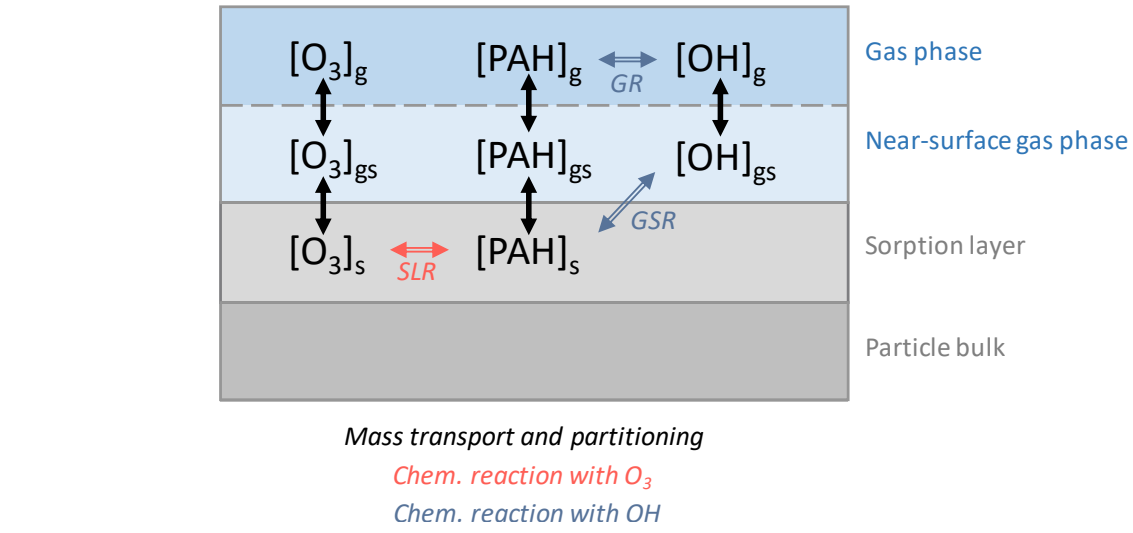

Figure A1. The model used in this study consists of three layers: gas-phase, near-surface gas-phase and sorption layer. The surface-layer reaction (SLR) with O_3, as well as the gas-surface reactions (GSR) and gas-phase reactions (GR) with OH are modeled alongside mass transport and partitioning.

https://doi.org/10.5194/acp-2020-1000
Preprint. Discussion started: 7 October 2020

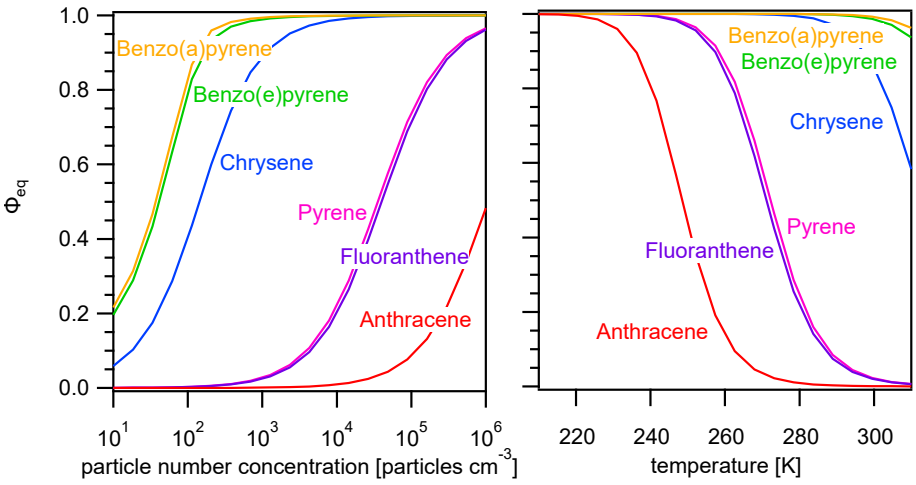

Figure A2. Equilibrium particulate fraction Φ_{eq} of selected PAHs as a function of a) particle number concentration ($T = 298$ K) and b) temperature ($N_p = 1 \times 10^3$) for particles of size $d_p = 50$ nm.

https://doi.org/10.5194/acp-2020-1000
Preprint. Discussion started: 7 October 2020

Atmospheric Chemistry and Physics Discussions

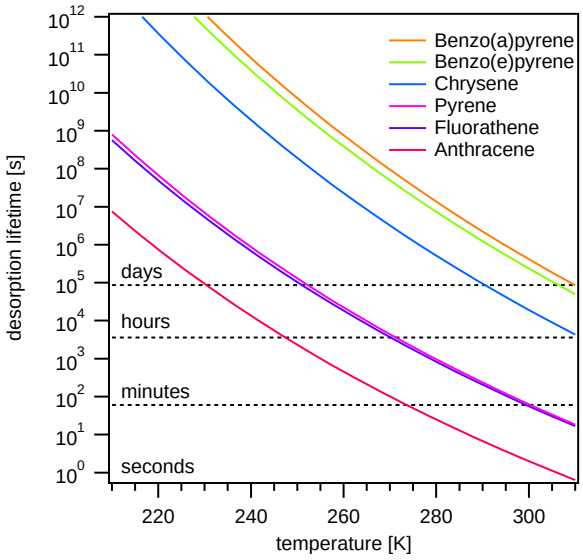

Figure A3. Desorption lifetime ($\tau_{\mathrm{des}} = 1/k_{\mathrm{des}}$) of selected PAHs as a function of temperature.

https://doi.org/10.5194/acp-2020-1000
Preprint. Discussion started: 7 October 2020

Atmospheric Chemistry and Physics Discussions

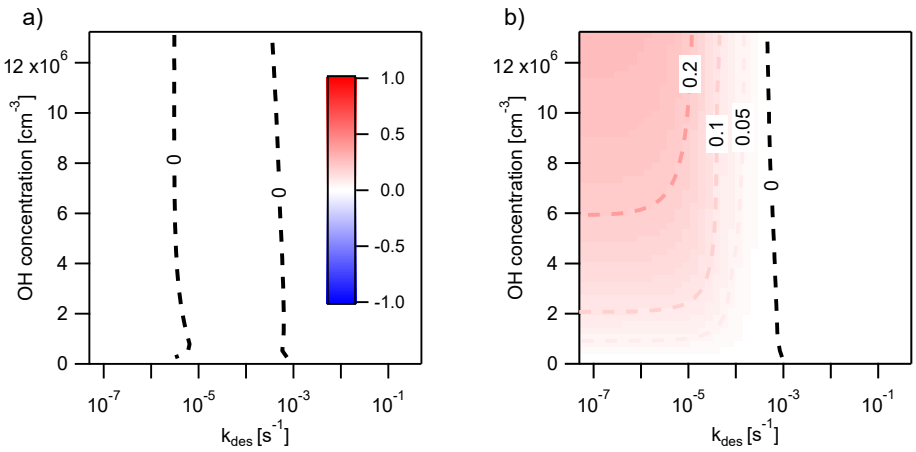

Figure A4. Discrepancy, determined with the error metric E_{loss}, between the the explicit-coupled solution EC and the operator-splitting solution IE with a time step of $\Delta t = 30$ min for the reaction of OH (1 ppt) with a) both gas- and particle-phase pyrene and b) only gas-phase pyrene. Regions where EC overestimates the loss of pyrene are indicated in red ($0 < E_{\text{loss}} \leq 1$) and underestimated in blue ($-1 \geq E_{\text{loss}} < 0$). The conditions are 280 K and 1×10^3 particles cm^{-3}.

https://doi.org/10.5194/acp-2020-1000
Preprint. Discussion started: 7 October 2020

Atmospheric Chemistry and Physics Discussions

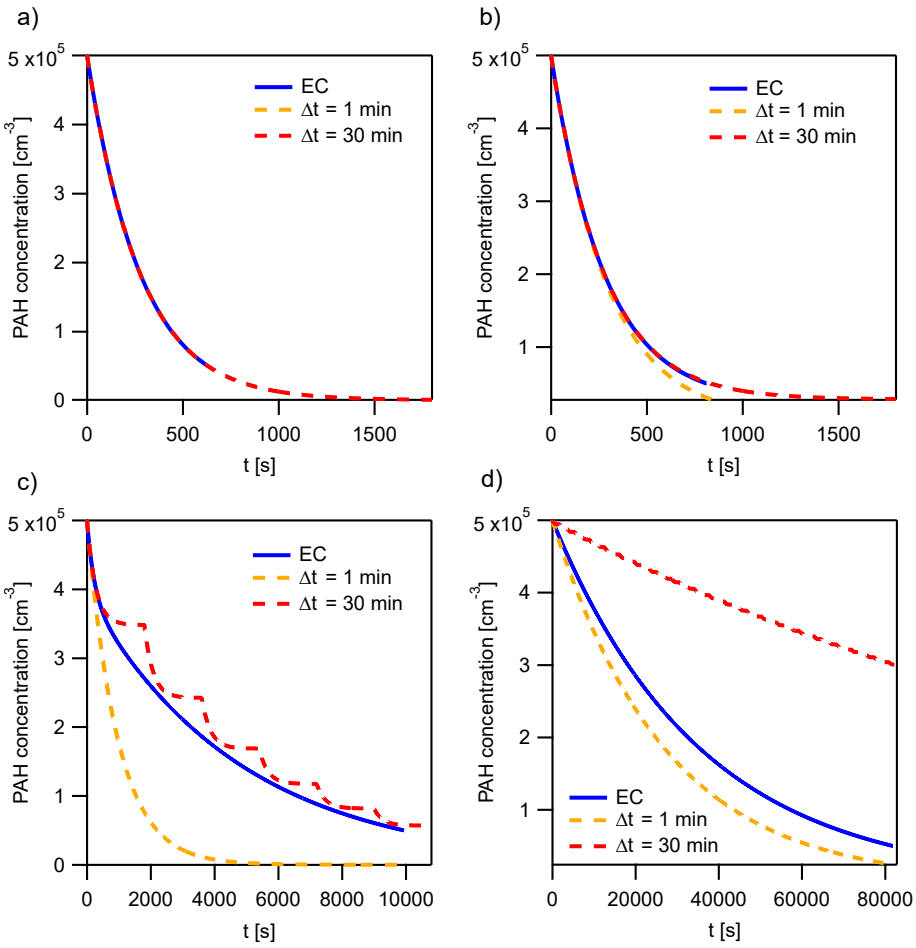

Figure A5. The explicit-coupled (EC) solution and instantaneous equilibration (IE) solutions with time steps $\Delta t = 1$ and 30 min at specific points for the evaluation of the error metric E_{loss} (Fig. 8a,b). These points represent a horizontal cross section of Fig. 8 at $[O_3] = 2.5 \times 10^{12}$ cm^{-3} and the following k_{des}: a) $10^{-6.3}$ b) $10^{-4.7}$ c) $10^{-3.1}$ and d) $10^{-1.5}$ s^{-1}.

https://doi.org/10.5194/acp-2020-1000
Preprint. Discussion started: 7 October 2020

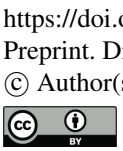

Atmospheric Chemistry and Physics Discussions

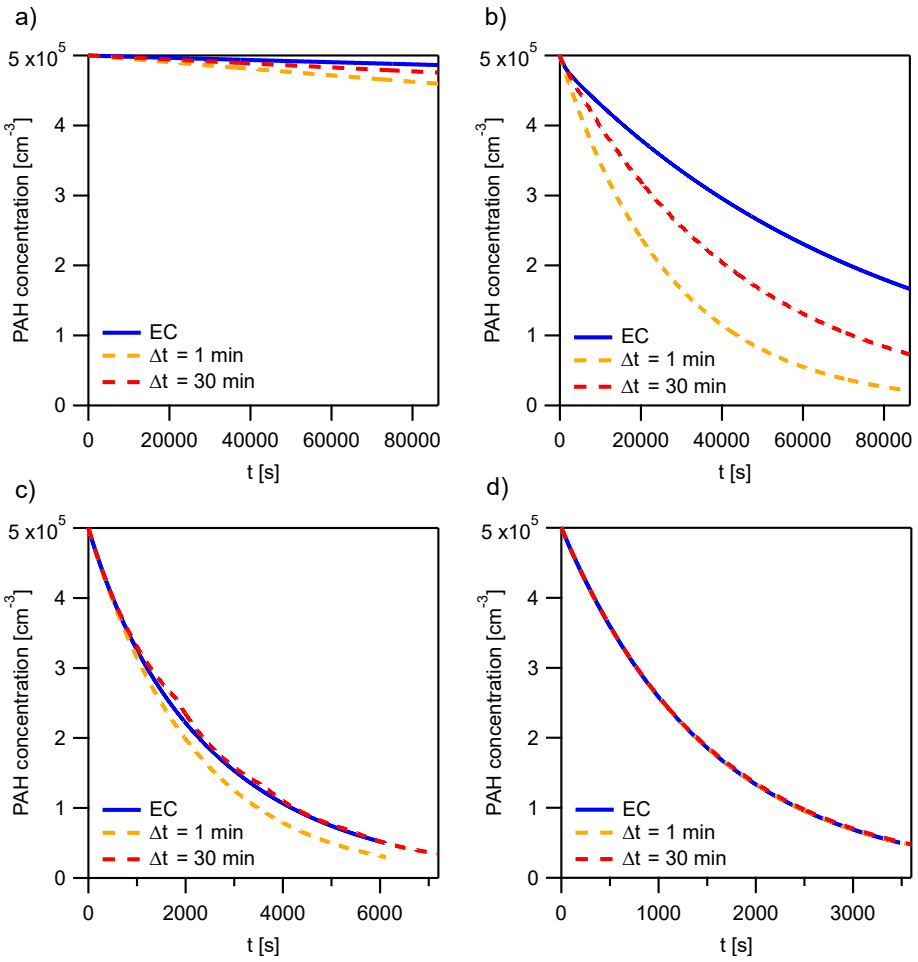

Figure A6. The explicit-coupled (EC) solution and instantaneous equilibration (IE) solutions with time steps $\Delta t = 1$ and 30 min at specific points for the evaluation of the error metric E_{loss} (Fig. A4b). These points represent a horizontal cross section of Fig. A4b at $[\text{OH}] = 1 \times 10^7$ cm^{-3} and the following k_{des}: a) $10^{-6.3}$ b) $10^{-4.7}$ c) $10^{-3.1}$ and d) $10^{-1.5}$ s^{-1}.

https://doi.org/10.5194/acp-2020-1000
Preprint. Discussion started: 7 October 2020

Atmospheric Chemistry and Physics Discussions

Table A1. Mass-transport parameters to determine the desorption rate coefficients of PAHs and O_3 ($k_{des} = Ae^{-E_A/RT}$): Arrhenius parameter A and activation energy of desorption E_A (Guilloteau et al., 2008, 2010).

Species	A / s^{-1}	E_a / kJ mol^{-1}
Anthracene	1.1×10^{15}	88.1
Fluoranthene	0.4×10^{15}	93.9
Pyrene	0.6×10^{15}	95.2
Chrysene	5.3×10^{15}	114.9
Benzo(e)pyrene	3.2×10^{15}	119.9
Benzo(a)pyrene	3.9×10^{15}	121.8
O_3	1.0×10^{14}	80.0

Table A2. Mass-transport parameters for adsorption of PAHs and O_3: molar mass M, surface accommodation coefficient on an adsorbate-free substrate $\alpha_{s,0}$ (Julin et al., 2014) and molecular cross section σ. The gas-phase diffusion coefficient D_g used for PAHs is 0.06 $cm^2 s^{-1}$ (Siddiqi et al., 2009) and for O_3 is 0.14 $cm^2 s^{-1}$ (Massman, 1998).

Species	M / g mol^{-1}	$\alpha_{s,0}$	σ / cm^2
Anthracene	178	1	$6{\times}10^{-15}$
Fluoranthene	202	1	$8{\times}10^{-15}$
Pyrene	202	1	$8{\times}10^{-15}$
Chrysene	228	1	$8{\times}10^{-15}$
Benzo(e)pyrene	252	1	$10{\times}10^{-15}$
Benzo(a)pyrene	252	1	$10{\times}10^{-15}$
O_3	48	0.001	$1.7{\times}10^{-15}$

https://doi.org/10.5194/acp-2020-1000
Preprint. Discussion started: 7 October 2020

Atmospheric Chemistry and Physics Discussions

Table A3. Symbols, definitions and units.

Symbol	Description	Units
$[\mathrm{PAH}]_\mathrm{g}$	gas phase concentration of PAH	cm^{-3}
$[\mathrm{PAH}]_\mathrm{gs}$	near-surface gas phase concentration of PAH	cm^{-3}
$[\mathrm{PAH}]_\mathrm{s}$	surface concentration of PAH	cm^{-2}
$[\mathrm{PAH}]_\mathrm{p}$	total particle phase concentration of PAH	cm^{-3}
Φ	particulate fraction	-
Φ_eq	equilibrium particulate fraction	-
Φ_qs	quasi-steady-state particulate fraction	-
Φ_0	initial particulate fraction	-
J_diff	gas diffusion flux	s^{-1}
J_coll	collision flux	$\mathrm{cm}^{-2}\,\mathrm{s}^{-1}$
J_ads	adsorption flux	$\mathrm{cm}^{-2}\,\mathrm{s}^{-1}$
J_des	desorption flux	$\mathrm{cm}^{-2}\,\mathrm{s}^{-1}$
V_gs	volume of near-surface gas phase	cm^{3}
L_g	loss rate from gas phase	$\mathrm{cm}^{-3}\,\mathrm{s}^{-1}$
L_s	loss rate from particle phase	$\mathrm{cm}^{-2}\,\mathrm{s}^{-1}$
N_p	particle number concentration	$\mathrm{particles}\,\mathrm{cm}^{-3}$
d_p	particle diameter	cm
t	time	s
τ_eq	equilibration timescale	s
τ_des	desorption lifetime	s
τ_ads	adsorption timescale	s
D_g	gas-phase diffusion coefficient	$\mathrm{cm}^{2}\,\mathrm{s}^{-1}$
R	gas constant	$\mathrm{J\,K}^{-1}\,\mathrm{mol}^{-1}$
ω	mean thermal velocity	$\mathrm{cm\,s}^{-1}$
M	molar mass	$\mathrm{kg\,mol}^{-1}$
σ	molecular cross section	cm^{2}
T	temperature	K
E_A	activation energy of desorption	$\mathrm{J\,mol}^{-1}$
k_des	desorption rate coefficient	s^{-1}
$\alpha_{\mathrm{s},0}$	surface accommodation coefficient on an adsorbate-free substrate	-

https://doi.org/10.5194/acp-2020-1000
Preprint. Discussion started: 7 October 2020

Atmospheric Chemistry and Physics Discussions

Table A4. Symbols, definitions and units.

Symbol	Description	Units
EC	explicit-coupled solution	-
IE	instantaneous-equilibration solution	-
$[\mathrm{PAH}](t)$	PAH concentration at time t	$\mathrm{cm}^{-3}\,\mathrm{s}^{-1}$
$[\mathrm{PAH}](0)$	PAH concentration at time $t = 0$	$\mathrm{cm}^{-3}\,\mathrm{s}^{-1}$
Δ[PAH](t)	total PAH loss up to time t	$\mathrm{cm}^{-3}\,\mathrm{s}^{-1}$
Δt	operator-splitting time step	s
Δt_{opt}	optimal operator-splitting time step	s
$t_{0\%}$	time at which simulation starts	s
$t_{90\%}$	time at which 90 % of PAH is lost	s

https://doi.org/10.5194/acp-2020-1000
Preprint. Discussion started: 7 October 2020

Atmospheric Chemistry and Physics Discussions

Author contributions. JW, UP, MS and TB designed research. JW, MS and TB wrote the model code and designed model calculations. JW and TB analyzed model results. JW and TB wrote the manuscript with contributions from all co-authors.

Competing interests. The authors declare that they have no conflict of interest.

Acknowledgements. This study was supported by the Max Planck Society (MPG). MS acknowledges funding by the U.S. National Science Foundation (AGS-1654104). The authors thank Gerhard Lammel for helpful discussions.

https://doi.org/10.5194/acp-2020-1000
Preprint. Discussion started: 7 October 2020

Atmospheric Chemistry and Physics Discussions

References

Akyüz, M. and Çabuk, H.: Gas–particle partitioning and seasonal variation of polycyclic aromatic hydrocarbons in the atmosphere of Zonguldak, Turkey, Sci. Total Environ., 408, 5550–5558, https://doi.org/10.1016/j.scitotenv.2010.07.063, 2010.

Arp, H. P. H., Schwarzenbach, R. P., and Goss, K.-U.: Ambient gas/particle partitioning. 2: The influence of particle source and temperature on sorption to dry terrestrial aerosols, Environ. Sci. Technol., 42, 5951–5957, https://doi.org/10.1021/es703096p, 2008.

Berkemeier, T., Takeuchi, M., Eris, G., and Ng, N. L.: Kinetic modelling of formation and evaporation of SOA from NO_3 oxidation of pure and mixed monoterpenes, Atmos. Chem. Phys. Discuss., https://doi.org/10.5194/acp-2020-55, in review, 2020.

Bernasconi, C. F.: Relaxation Kinetics, Chapter 1 - Basic Principles, Academic Press, https://doi.org/https://doi.org/10.1016/B978-0-12-092950-4.50005-8, 1976.

Bertram, A. K., Ivanov, A. V., Hunter, M., Molina, L. T., and Molina, M. J.: The reaction probability of OH on organic surfaces of tropospheric interest, J. Phys. Chem. A, 105, 9415–9421, https://doi.org/10.1021/jp0114034, 2001.

Billiard, S. M., Meyer, J. N., Wassenberg, D. M., Hodson, P. V., and Di Giulio, R. T.: Nonadditive effects of PAHs on Early Vertebrate Development: mechanisms and implications for risk assessment, Toxicol. Sci., 105, 5–23, https://doi.org/10.1093/toxsci/kfm303, 2008.

Boström, C.-E., Gerde, P., Hanberg, A., Jernström, B., Johansson, C., Kyrklund, T., Rannug, A., Törnqvist, M., Victorin, K., and Westerholm, R.: Cancer risk assessment, indicators, and guidelines for polycyclic aromatic hydrocarbons in the ambient air., Environ. Health Perspect., 110, 451–488, https://doi.org/10.1289/ehp.110-1241197, 2002.

Brasseur, G. P. and Jacob, D. J.: Modeling of Atmospheric Chemistry, Cambridge University Press, https://doi.org/10.1017/9781316544754, 2017.

Callén, M. S., de la Cruz, M. T., López, J. M., Murillo, R., Navarro, M. V., and Mastral, A. M.: Some inferences on the mechanism of atmospheric gas/particle partitioning of polycyclic aromatic hydrocarbons (PAH) at Zaragoza (Spain), Chemosphere, 73, 1357–1365, https://doi.org/10.1016/j.chemosphere.2008.06.063, 2008.

Cappa, C. D. and Wilson, K. R.: Evolution of organic aerosol mass spectra upon heating: implications for OA phase and partitioning behavior, Atmos. Chem. Phys., 11, 1895–1911, https://doi.org/10.5194/acp-11-1895-2011, 2011.

Chu, S. N., Sands, S., Tomasik, M. R., Lee, P. S., and McNeill, V. F.: Ozone oxidation of surface-adsorbed polycyclic aromatic hydrocarbons: Role of PAH-surface interaction, J. Am. Chem. Soc, 132, 15 968–15 975, https://doi.org/10.1021/ja1014772, 2010.

Dachs, J. and Eisenreich, S. J.: Adsorption onto aerosol soot carbon dominates gas-particle partitioning of polycyclic aromatic hydrocarbons, Environ. Sci. Technol., 34, 3690–3697, https://doi.org/10.1021/es991201+, 2000.

Ding, N., Chen, X., and Wu, C.-M. L.: Interactions between polybrominated diphenyl ethers and graphene surface: a DFT and MD investigation, Environ. Sci. Nano, 1, 55–63, https://doi.org/10.1039/C3EN00037K, 2014.

Fasnacht, M. P. and Blough, N. V.: Aqueous photodegradation of polycyclic aromatic hydrocarbons, Environ. Sci. Technol., 36, 4364–4369, https://doi.org/10.1021/es025603k, 2002.

Finizio, A., Mackay, D., Bidleman, T., and Harner, T.: Octanol-air partition coefficient as a predictor of partitioning of semi-volatile organic chemicals to aerosols, Atmos. Environ., 31, 2289–2296, https://doi.org/10.1016/S1352-2310(97)00013-7, 1997.

Fraser, S. J.: The steady state and equilibrium approximations: A geometrical picture, The Journal of Chemical Physics, 88, 4732–4738, https://doi.org/10.1063/1.454686, 1988.

https://doi.org/10.5194/acp-2020-1000
Preprint. Discussion started: 7 October 2020

Friedman, C. L., Pierce, J. R., and Selin, N. E.: Assessing the influence of secondary organic versus primary carbonaceous aerosols on long-range atmospheric polycyclic aromatic hydrocarbon transport, Environ. Sci. Technol., 48, 3293–3302, https://doi.org/10.1021/es405219r, 2014.

Galarneau, E., Makar, P. A., Zheng, Q., Narayan, J., Zhang, J., Moran, M. D., Bari, M. A., Pathela, S., Chen, A., and Chlumsky, R.: PAH concentrations simulated with the AURAMS-PAH chemical transport model over Canada and the USA, Atmos. Chem. Phys., 14, 4065–4077, https://doi.org/10.5194/acp-14-4065-2014, 2014.

Geyer, A., Bächmann, K., Hofzumahaus, A., Holland, F., Konrad, S., Klüpfel, T., Pätz, H.-W., Perner, D., Mihelcic, D., Schäfer, H.-J., Volz-Thomas, A., and Platt, U.: Nighttime formation of peroxy and hydroxyl radicals during the BERLIOZ campaign: Observations and modeling studies, J. Geophys. Res. Atmos., 108, 8249, https://doi.org/10.1029/2001JD000656, 2003.

Gross, S. and Bertram, A. K.: Reactive uptake of NO_3, N_2O_5, NO_2, HNO_3, and O_3 on three types of polycyclic aromatic hydrocarbon surfaces, J. Phys. Chem. A, 112, 3104–3113, https://doi.org/10.1021/jp7107544, 2008.

Guilloteau, A., Nguyen, M. L., Bedjanian, Y., and Le Bras, G.: Desorption of polycyclic aromatic hydrocarbons from soot surface: Pyrene and fluoranthene, J. Phys. Chem. A, 112, 10 552–10 559, https://doi.org/10.1021/jp803043s, 2008.

Guilloteau, A., Bedjanian, Y., Nguyen, M. L., and Tomas, A.: Desorption of polycyclic aromatic hydrocarbons from a soot surface: Three- to five-ring PAHs, J. Phys. Chem. A, 114, 942–948, https://doi.org/10.1021/jp908862c, 2010.

Harner, T. and Bidleman, T. F.: Octanol-air partition coefficient for describing particle/gas partitioning of aromatic compounds in urban air, Environ. Sci. Technol., 32, 1494–1502, https://doi.org/10.1021/es970890r, 1998.

Hobbs, P. V., Sinha, P., Yokelson, R. J., Christian, T. J., Blake, D. R., Gao, S., Kirchstetter, T. W., Novakov, T., and Pilewskie, P.: Evolution of gases and particles from a savanna fire in South Africa, J. Geophys. Res. Atmos., 108, https://doi.org/10.1029/2002JD002352, 2003.

Hofzumahaus, A., Rohrer, F., Lu, K., Bohn, B., Brauers, T., Chang, C.-C., Fuchs, H., Holland, F., Kita, K., Kondo, Y., Li, X., Lou, S., Shao, M., Zeng, L., Wahner, A., and Zhang, Y.: Amplified trace gas removal in the troposphere, Science, 324, 1702–1704, https://doi.org/10.1126/science.1164566, 2009.

Julin, J., Winkler, P. M., Donahue, N. M., Wagner, P. E., and Riipinen, I.: Near-unity mass accommodation coefficient of organic molecules of varying structure, Environ. Sci. Technol., 48, 12 083–12 089, https://doi.org/10.1021/es501816h, 2014.

Junge, C.: Basic considerations about trace constituents in the atmosphere as related to the fate of global pollutants. In: Suffet IH (ed), Fate of pollutants in the air and water environments, Part I., Wiley-Interscience, New York, 1977.

Kamens, R., Odum, J., and Fan, Z.-H.: Some observations on times to equilibrium for semivolatile polycyclic aromatic hydrocarbons, Environ. Sci. Technol., 29, 43–50, https://doi.org/10.1021/es00001a005, 1995.

Keyte, I. J., Harrison, R. M., and Lammel, G.: Chemical reactivity and long-range transport potential of polycyclic aromatic hydrocarbons – a review, Chem. Soc. Rev., 42, 9333–9391, https://doi.org/10.1039/C3CS60147A, 2013.

Kiefer, J.: Sequential minimax search for a maximum, Proc. Am. Math. Soc., 4, 502–506, https://doi.org/10.1090/S0002-9939-1953-0055639-3, 1953.

Kim, K.-H., Jahan, S. A., Kabir, E., and Brown, R. J. C.: A review of airborne polycyclic aromatic hydrocarbons (PAHs) and their human health effects, Environ. Int., 60, 71–80, https://doi.org/10.1016/j.envint.2013.07.019, 2013.

Kubicki, J. D.: Molecular simulations of benzene and PAH interactions with soot, Environ. Sci. Technol., 40, 2298–2303, https://doi.org/10.1021/es051083s, 2006.

Lammel, G., Sehili, A. M., Bond, T. C., Feichter, J., and Grassl, H.: Gas/particle partitioning and global distribution of polycyclic aromatic hydrocarbons – A modelling approach, Chemosphere, 76, 98–106, https://doi.org/10.1016/j.chemosphere.2009.02.017, 2009.

https://doi.org/10.5194/acp-2020-1000
Preprint. Discussion started: 7 October 2020

Atmospheric Chemistry and Physics Discussions

Lammel, G., Klánová, J., Ilić, P., Kohoutek, J., Gasić, B., Kovacić, I., and Škrdlíková, L.: Polycyclic aromatic hydrocarbons in air on small spatial and temporal scales – II. Mass size distributions and gas-particle partitioning, Atmos. Environ., 44, 5022–5027, https://doi.org/10.1016/j.atmosenv.2010.08.001, 2010.

Lazar, P., Karlický, F., Jurečka, P., Kocman, M., Otyepková, E., Šafářová, K., and Otyepka, M.: Adsorption of small organic molecules on graphene, J. Am. Chem. Soc., 135, 6372–6377, https://doi.org/10.1021/ja403162r, 2013.

Lechner, C. and Sax, A. F.: Adhesive forces between aromatic molecules and graphene, J. Phys. Chem. C, 118, 20 970–20 981, https://doi.org/10.1021/jp505894p, 2014.

Li, Y. and Shiraiwa, M.: Timescales of secondary organic aerosols to reach equilibrium at various temperatures and relative humidities, Atmos. Chem. Phys., 19, 5959–5971, https://doi.org/10.5194/acp-19-5959-2019, 2019.

Li, Y.-F., Ma, W.-L., and Yang, M.: Prediction of gas/particle partitioning of polybrominated diphenyl ethers (PBDEs) in global air: A theoretical study, Atmos. Chem. Phys., 15, 1669–1681, https://doi.org/10.5194/acp-15-1669-2015, 2015.

Lohmann, R. and Lammel, G.: Adsorptive and absorptive contributions to the gas-particle partitioning of polycyclic aromatic hydrocarbons: State of knowledge and recommended parametrization for modeling, Environ. Sci. Technol., 38, 3793–3803, https://doi.org/10.1021/es035337q, 2004.

Lohmann, R., Harner, T., Thomas, G. O., and Jones, K. C.: A comparative study of the gas-particle partitioning of PCDD/Fs, PCBs, and PAHs, Environ. Sci. Technol., 34, 4943–4951, https://doi.org/10.1021/es9913232, 2000.

Mader, B. T. and Pankow, J. F.: Study of the effects of particle-phase carbon on the gas/particle partitioning of semivolatile organic compounds in the atmosphere using controlled field experiments, Environ. Sci. Technol., 36, 5218–5228, https://doi.org/10.1021/es011048v, 2002.

Mandalakis, M., Tsapakis, M., Tsoga, A., and Stephanou, E. G.: Gas–particle concentrations and distribution of aliphatic hydrocarbons, PAHs, PCBs and PCDD/Fs in the atmosphere of Athens (Greece), Atmos. Environ., 36, 4023–4035, https://doi.org/10.1016/S1352-2310(02)00362-X, 2002.

Massman, W. J.: A review of the molecular diffusivities of H_2O, CO_2, CH_4, CO, O_3, SO_2, NH_3, N_2O, NO, and NO_2 in air, O_2 and N_2 near STP, Atmos. Environ., 32, 1111–1127, https://doi.org/10.1016/S1352-2310(97)00391-9, 1998.

McFiggans, G. B., Alfarra, M. R., Allan, J., Coe, H., Hamilton, J., Harrison, R., Jenkin, M. E., Lewis, A., Moller, S. J., and Williams, P. I.: A review of the state-of-the-science relating to secondary particulate matter of relevance to the composition of the UK atmosphere : Full technical report to Defra, project AQ0732., http://eprints.whiterose.ac.uk/92381/, 2015.

Meng, Z. and Seinfeld, J. H.: Time scales to achieve atmospheric gas-aerosol equilibrium for volatile species, Atmos. Environ., 30, 2889–2900, https://doi.org/10.1016/1352-2310(95)00493-9, 1996.

Miguel, A. H., Kirchstetter, T. W., Harley, R. A., and Hering, S. V.: On-road emissions of particulate polycyclic aromatic hydrocarbons and black carbon from gasoline and diesel vehicles, Environ. Sci. Technol., 32, 450–455, https://doi.org/10.1021/es970566w, 1998.

Mu, Q., Shiraiwa, M., Octaviani, M., Ma, N., Ding, A., Su, H., Lammel, G., Pöschl, U., and Cheng, Y.: Temperature effect on phase state and reactivity controls atmospheric multiphase chemistry and transport of PAHs, Sci. Adv., 4, eaap7314, https://doi.org/10.1126/sciadv.aap7314, 2018.

Odum, J. R., Yu, J., and Kamens, R. M.: Modeling the mass transfer of semivolatile organics in combustion aerosols, Environ. Sci. Technol., 28, 2278–2285, https://doi.org/10.1021/es00062a011, 1994.

Pankow, J. F.: An absorption model of gas/particle partitioning of organic compounds in the atmosphere, Atmos. Environ., 28, 185–188, https://doi.org/10.1016/1352-2310(94)90093-0, 1994.

https://doi.org/10.5194/acp-2020-1000
Preprint. Discussion started: 7 October 2020

Pankow, J. F. and Bidleman, T. F.: Interdependence of the slopes and intercepts from log-log correlations of measured gas-particle partitioning and vapor pressure—I. theory and analysis of available data, Atmos. Environ., 26, 1071–1080, https://doi.org/10.1016/0960-1686(92)90039-N, 1992.

Pöschl, U.: Atmospheric aerosols: Composition, transformation, climate and health effects, Angew. Chem. Int. Ed., 44, 7520–7540, https://doi.org/10.1002/anie.200501122, 2005.

Pöschl, U., Rudich, Y., and Ammann, M.: Kinetic model framework for aerosol and cloud surface chemistry and gas-particle interactions - Part 1: General equations, parameters, and terminology, Atmos. Chem. Phys., 7, 5989–6023, https://doi.org/10.5194/acp-7-5989-2007, 2007.

Ravindra, K., Sokhi, R., and Van Grieken, R.: Atmospheric polycyclic aromatic hydrocarbons: Source attribution, emission factors and regulation, Atmos. Environ., 42, 2895–2921, https://doi.org/10.1016/j.atmosenv.2007.12.010, 2008.

Rounds, S. A. and Pankow, J. F.: Application of a radial diffusion model to describe gas/particle sorption kinetics, Environ. Sci. Technol., 24, 1378–1386, https://doi.org/10.1021/es00079a012, 1990.

Saleh, R., Donahue, N. M., and Robinson, A. L.: Time scales for gas-particle partitioning equilibration of secondary organic aerosol formed from alpha-pinene ozonolysis, Environ. Sci. Technol., 47, 5588–5594, https://doi.org/10.1021/es400078d, 2013.

Sehili, A. M. and Lammel, G.: Global fate and distribution of polycyclic aromatic hydrocarbons emitted from Europe and Russia, Atmos. Environ., 41, 8301–8315, https://doi.org/10.1016/j.atmosenv.2007.06.050, 2007.

Shahpoury, P., Lammel, G., Albinet, A., Sofuoğlu, A., Dumanoğlu, Y., Sofuoğlu, S. C., Wagner, Z., and Zdimal, V.: Evaluation of a conceptual model for gas-particle partitioning of polycyclic aromatic hydrocarbons using polyparameter linear free energy relationships, Environ. Sci. Technol., 50, 12 312–12 319, https://doi.org/10.1021/acs.est.6b02158, 2016.

Shiraiwa, M. and Seinfeld, J. H.: Equilibration timescale of atmospheric secondary organic aerosol partitioning, Geophys. Res. Lett., 39, https://doi.org/10.1029/2012GL054008, 2012.

Shiraiwa, M., Garland, R. M., and Pöschl, U.: Kinetic double-layer model of aerosol surface chemistry and gas-particle interactions (K2-SURF): Degradation of polycyclic aromatic hydrocarbons exposed to O_3, NO_2, H_2O, OH and NO_3, Atmos. Chem. Phys., 9, 9571–9586, https://doi.org/10.5194/acp-9-9571-2009, 2009.

Shiraiwa, M., Sosedova, Y., Rouvière, A., Yang, H., Zhang, Y., Abbatt, J. P. D., Ammann, M., and Pöschl, U.: The role of long-lived reactive oxygen intermediates in the reaction of ozone with aerosol particles, Nat. Chem, 3, 291–295, https://doi.org/10.1038/nchem.988, 2011.

Shiraiwa, M., Yee, L. D., Schilling, K. A., Loza, C. L., Craven, J. S., Zuend, A., Ziemann, P. J., and Seinfeld, J. H.: Size distribution dynamics reveal particle-phase chemistry in organic aerosol formation, Proc. Natl. Acad. Sci. U.S.A., 110, 11 746–11 750, https://doi.org/10.1073/pnas.1307501110, 2013.

Shrivastava, M., Lou, S., Zelenyuk, A., Easter, R. C., Corley, R. A., Thrall, B. D., Rasch, P. J., Fast, J. D., Simonich, S. L. M., Shen, H., and Tao, S.: Global long-range transport and lung cancer risk from polycyclic aromatic hydrocarbons shielded by coatings of organic aerosol, Proc. Natl. Acad. Sci. U.S.A., 114, 1246–1251, https://doi.org/10.1073/pnas.1618475114, 2017.

Siddiqi, M. A., Siddiqui, R. A., and Atakan, B.: Thermal stability, sublimation pressures, and diffusion coefficients of anthracene, pyrene, and some metal β-diketonates, J. Chem. Eng. Data, 54, 2795–2802, https://doi.org/10.1021/je9001653, 2009.

Stone, D., Whalley, L. K., and Heard, D. E.: Tropospheric OH and HO_2 radicals: field measurements and model comparisons, Chem. Soc. Rev., 41, 6348–6404, https://doi.org/10.1039/C2CS35140D, 2012.

Tang, M. J., Cox, R. A., and Kalberer, M.: Compilation and evaluation of gas phase diffusion coefficients of reactive trace gases in the atmosphere: volume 1. Inorganic compounds, Atmos. Chem. Phys., 14, 9233–9247, https://doi.org/10.5194/acp-14-9233-2014, 2014.

https://doi.org/10.5194/acp-2020-1000
Preprint. Discussion started: 7 October 2020

Terzi, E. and Samara, C.: Gas-particle partitioning of polycyclic aromatic hydrocarbons in urban, adjacent coastal, and continental background sites of Western Greece, Environ. Sci. Technol., 38, 4973–4978, https://doi.org/10.1021/es040042d, 2004.

Vingarzan, R.: A review of surface ozone background levels and trends, Atmos. Environ., 38, 3431–3442, https://doi.org/10.1016/j.atmosenv.2004.03.030, 2004.

Wang, T., Xue, L., Brimblecombe, P., Lam, Y. F., Li, L., and Zhang, L.: Ozone pollution in China: A review of concentrations, meteorological influences, chemical precursors, and effects, Sci. Total Environ., 575, 1582–1596, https://doi.org/10.1016/j.scitotenv.2016.10.081, 2017.

Wei, C., Han, Y., Bandowe, B. A. M., Cao, J., Huang, R.-J., Ni, H., Tian, J., and Wilcke, W.: Occurrence, gas/particle partitioning and carcinogenic risk of polycyclic aromatic hydrocarbons and their oxygen and nitrogen containing derivatives in Xi'an, central China, Sci. Total Environ., 505, 814–822, https://doi.org/10.1016/j.scitotenv.2014.10.054, 2015.

Yamasaki, H., Kuwata, K., and Miyamoto, H.: Effects of ambient temperature on aspects of airborne polycyclic aromatic hydrocarbons, Environ. Sci. Technol., 16, 189–194, https://doi.org/10.1021/es00098a003, 1982.

Zhang, H., Worton, D. R., Shen, S., Nah, T., Isaacman-VanWertz, G., Wilson, K. R., and Goldstein, A. H.: Fundamental time scales governing organic aerosol multiphase partitioning and oxidative aging, Environ. Sci. Technol., 49, 9768–9777, https://doi.org/10.1021/acs.est.5b02115, 2015.

Zhang, Q., Gao, R., Xu, F., Zhou, Q., Jiang, G., Wang, T., Chen, J., Hu, J., Jiang, W., and Wang, W.: Role of water molecule in the gas-phase formation process of nitrated polycyclic aromatic hydrocarbons in the atmosphere: A computational study, Environ. Sci. Technol., 48, 5051–5057, https://doi.org/10.1021/es500453g, 2014.

Škrdlíková, L., Landlová, L., Klánová, J., and Lammel, G.: Wet deposition and scavenging efficiency of gaseous and particulate phase polycyclic aromatic compounds at a central European suburban site, Atmos. Environ., 45, 4305–4312, https://doi.org/10.1016/j.atmosenv.2011.04.072, 2011.

2.2. Global Modeling of Nitrated PAHs

This chapter has already been published in Environmental Science and Technology (ES&T). I am the first author of this publication and my personal contribution included adapting code in the EMAC-SVOC global model to include nitrated PAHs (using Fortran 90), identifying important chemical processes and collecting physicochemical and kinetic parameters from the literature, developing the NO_2-dependent formation scheme using existing quantum mechanical calculations, running simulations (using supercomputers) and writing code to process, visualize, and statistically analyze geospatial data (using CDO, Ferret, and MATLAB). Alongside my coauthors, I played a primary role preparing figures, collecting observational data from the literature, analyzing results and writing the manuscript.

Environ. Sci. Tech. (2020).

Modeling the formation, degradation and spatiotemporal distribution of 2-nitrofluoranthene and 2-nitropyrene in the global atmosphere

Jake Wilson[1,†], Mega Octaviani[1,†,△], Benjamin A. Musa Bandowe[1], Marco Wietzoreck[1], Cornelius Zetzsch[1,2], Ulrich Pöschl[1], Thomas Berkemeier[1,*], and Gerhard Lammel[1,3,*]

[1]Multiphase Chemistry Department, Max Planck Institute for Chemistry, Mainz, Germany
[2]Bayreuth Centre for Ecology and Environmental Research, Bayreuth, Germany
[3]Research Centre for Toxic Compounds in the Environment, Brno, Czech Republic
[△]Now at Pacific Northwest National Laboratory, Richland, Washington, United States
[†,*]Equal contributions

Environmental Science & Technology

pubs.acs.org/est

Article

Modeling the Formation, Degradation, and Spatiotemporal Distribution of 2-Nitrofluoranthene and 2-Nitropyrene in the Global Atmosphere

Jake Wilson,[⊥] Mega Octaviani,[⊥] Benjamin A. Musa Bandowe, Marco Wietzoreck, Cornelius Zetzsch, Ulrich Pöschl, Thomas Berkemeier,* and Gerhard Lammel*

Cite This: https://dx.doi.org/10.1021/acs.est.0c04319

Read Online

ACCESS | Metrics & More | Article Recommendations | Supporting Information

ABSTRACT: Polycyclic aromatic hydrocarbons (PAHs) are common atmospheric pollutants and known to cause adverse health effects. Nitrated PAHs (NPAHs) are formed in combustion activities and by nitration of PAHs in the atmosphere and may be equally or more toxic, but their spatial and temporal distribution in the atmosphere is not well characterized. Using the global EMAC model with atmospheric chemistry and surface compartments coupled, we investigate the formation, abundance, and fate of two secondarily formed NPAHs, 2-nitrofluoranthene (2-NFLT) and 2-nitropyrene (2-NPYR). The default reactivity scenario, the model with the simplest interpretation of parameters from the literature, tends to overestimate both absolute concentrations and NPAH/PAH ratios at observational sites. Sensitivity scenarios indicate that NO_2-dependent NPAH formation leads to better agreement between measured and predicted NPAH concentrations and that photodegradation is the most important loss process of 2-NFLT and 2-NPYR. The highest concentrations of 2-NFLT and 2-NPYR are found in regions with strong PAH emissions, but because of continued secondary formation from the PAH precursors, these two NPAHs are predicted to be spread across the globe.

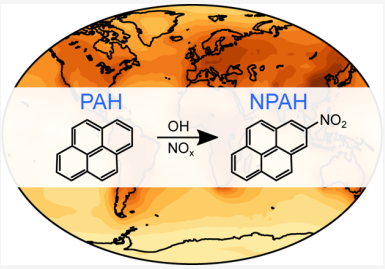

1. INTRODUCTION

Human exposure to polluted air is associated with severe health effects: asthma, chronic obstructive pulmonary disease, lung cancer, cardiovascular diseases, and mortality.[1−4] Polluted air contains a complex mixture of organic and inorganic chemical species including polycyclic aromatic hydrocarbons (PAHs) and their photochemical degradation products, which exhibit mutagenicity and other hazardous properties.[5−10]

Nitrated PAHs (NPAHs) are a group of PAH derivatives substantially contributing to the toxicity of polluted air.[7,11−17] Many NPAHs are emitted together with PAHs from primary combustion sources; for example, 9-nitroanthracene, 3-nitrofluoranthene, and 1-nitropyrene are produced and emitted upon diesel combustion.[18−20] Other NPAHs are produced in the atmosphere by chemical transformation of PAHs. Specifically, 2-nitrofluoranthene (2-NFLT) and 2-nitropyrene (2-NPYR) are both formed by radical-initiated (OH or NO_3) nitration of the parent PAH.[13,21−26] Unlike other isomers, 2-NFLT and 2-NPYR are not found in road and marine diesel emissions or only in minor amounts, for instance 2-NFLT/3-NFLT $\leq$ 0.05[20,27] and 2-NPYR/1-NPYR $\leq$ 0.01.[20,28] Nor are they emitted in coal or wood burning to any significant amount.[29−31]

Given the toxicity of NPAHs, there is a demand for assessing the exposure of humans and the environment. The biological effects of NPAHs are usually stronger than those of the parent PAHs. This has been documented for the mutagenicity of fluoranthene (FLT), pyrene (PYR), chrysene, and their nitrated derivatives[5,7,9,32,33] and for the developmental toxicity of phenanthrene, anthracene, PYR, and their nitrated derivatives.[17] The spatial and temporal distributions of 2-NFLT and 2-NPYR, however, have not yet been characterized. For these compounds, there is a lack of long-term air monitoring, and monitoring data are available only for few geographic locations.[16] As 2-NFLT and 2-NPYR are not directly emitted and their photochemical formation in air does not occur instantaneously, their distributions cannot be assumed to be identical to those of the parent PAHs. Because of long-range transport, both products[34−37] and their precursors[38,39] can be found in remote areas away from the source.[34,37,40]

Kinetic models have been used to explore the formation and loss of 2-NFLT and 2-NPYR,[41,42] while multimedia models have been used to quantify human exposure under steady-state conditions[33] or derive emission estimates for parent PAHs.[43] Regression models have been used to study 2-NPYR and 2-

Received: July 1, 2020
Revised: October 7, 2020
Accepted: October 16, 2020

NFLT on local[44] and regional[45] scales. So far, however, atmospheric transport and chemistry have not yet been studied on the large scale, and the global atmospheric burden and geographical distribution of these secondarily formed NPAHs have not been addressed.

In this study, we implement the chemistry of 2-NFLT and 2-NPYR into a global model (EMAC-SVOC) which has previously been used to simulate the spatiotemporal distributions of FLT and PYR in the global atmosphere.[46] Nitration of the precursors FLT and PYR in the gas phase yields 2-NFLT and 2-NPYR, which then partition into the particle phase where they are susceptible to photodegradation. We present modeled near-surface concentrations and vertical column densities of 2-NFLT and 2-NPYR in comparison to observational measurement data from the literature, including a long-term monitoring site on the Noto Peninsula, Japan. Alongside the results using the simplest interpretation of literature input parameters (the default reactivity scenario), we present results from sensitivity scenarios to explore two uncertainties related to the chemical formation and loss of NPAHs in the atmosphere: the concentration of NO_2 and the rate of photodegradation. Finally, we discuss the predicted spatial distributions of 2-NFLT and 2-NPYR column densities and near-surface concentrations.

2. METHODS

2.1. Model Description and Setup. To simulate the chemistry and transport of 2-NFLT and 2-NPYR, we used the global ECHAM5/MESSy atmospheric chemistry model,[47,48] which includes the recently developed SVOC submodel to describe the environmental cycling of semivolatile organic compounds.[46] EMAC simulates gas-phase chemical reactions through the MECCA submodel[49] and calculates photolysis rates through the JVAL submodel.[47] EMAC-SVOC simulates diffusive air−surface exchange through coupled surface compartments and was recently evaluated for PAHs with a wide range of physicochemical properties.[46] The oxidants OH, O_3, NO_2, and NO_3 are tracers formed and consumed in MECCA. The scavenging of gases and aerosols by clouds and rain is calculated by the SCAV submodel,[50] while their dry removal mechanism is calculated by DRYDEP.[51] Aerosol microphysics (external/internal mixing, nucleation, condensation, and coagulation) are treated by the GMXe submodel.[52] The primary aerosol components included are sulfate, black carbon (BC), organic matter (OM), sea salt, and mineral dust. Each aerosol species is described as seven log-normal size distributions, of which four modes (nucleation, Aitken, accumulation, and coarse) are soluble and three modes (Aitken, accumulation, and coarse) are insoluble. The nucleation hydrophilic mode is only used to describe the sulfate particles.[52] We neglect the treatment of the nitrate aerosol but include that of ammonium; consequently, the model assumes that all sulfate is in the form of ammonium sulfate.[52] The effect of ammonium nitrate aerosols on NPAH tracers is expected to be negligible as NPAH formation and photodegradation are independent of nitrate concentrations and even pH. The contribution of adsorption to NH_4NO_3 to gas/particle partitioning is minor as adsorption in total is minor compared to absorption in OM.[53] In the model aerosol, the NPAH is concentrated in the submicrometer size fraction (about 80% are associated with PM_1), in accordance with observations.[54−57]

The model was run on a T42 spectral grid resolution (corresponding to a Gaussian grid of approximately 2.8 × 2.8° lat-lon) and 19 vertical hybrid pressure levels extending to 10 h Pa. The simulations were performed for the years 2005−2008, including a 1 year spin-up period, and were nudged toward the European Centre for Medium-Range Weather Forecast (ECMWF) reanalysis data.[58]

The formation of 2-NFLT and 2-NPYR (from their parent PAHs) as well as their loss was implemented in this model as detailed below.

2.2. Formation of 2-NFLT and 2-NPYR. The dominant source of 2-NFLT and 2-NPYR is nitration of the respective gaseous PAH precursors FLT and PYR. Heterogeneous reactions of PYR and NO_2 on minerals form 1-NPYR only,[59−61] while from FLT, no 2-NFLT is formed under ambient NO_2 concentrations, unlike under unrealistically high NO_2.[62] It is now understood that the heterogeneous reactions of particle-bound FLT and PYR with ambient levels of NO_x and NO_2/O_3 and under realistic atmospheric conditions (e.g., relative humidity) do not allow for or only result in negligible formation of 2-NFLT and 2-NPYR.[62−64] Consequently, 2-NFLT and 2-NPYR in the atmosphere are mainly attributable to their gas-phase free-radical formation (described below).

Gas-phase formation of 2-NFLT and 2-NPYR is included in the model. Table 1 lists the reactions, and Table 2 lists the rate coefficients and yields used. This formation proceeds via a two-step reaction (Figure S1).[65] In the first step, a hydroxyl (OH) or nitrate (NO_3) radical reacts with the PAH to form a PAH-radical adduct. This intermediate may react with either NO_2 to form NPAH or O_2 to form other oxygenated products.[13,65] Note that 2-NFLT formation is initiated by either OH or NO_3, whereas 2-NPYR formation is initiated by OH attack only. Atkinson et al. empirically determined rate coefficients for the addition reactions and calculated the overall yields of 2-NFLT and 2-NPYR at NO_x concentrations (≈1−10 ppm) much higher than typical ambient conditions.[66] In addition, Brubaker and Hites experimentally determined the rate coefficient for the reaction of FLT with OH.[67] These rate coefficients and yields are used in the model as the default reactivity scenario in the model (Table 2, default reactivity scenario).

Table 1. Overview of Chemical Formation and Loss Reactions in the Model for 2-NFLT and 2-NPYR

reaction	rate expression
$FLT_{(g)} + OH_{(g)} \rightarrow 2\text{-}NFLT_{(g)}$	$Y_{2\text{-}NFLT,OH} \times k_{FLT+OH} \times [OH]_g \times [FLT]_g$
$PYR_{(g)} + OH_{(g)} \rightarrow 2\text{-}NPYR_{(g)}$	$Y_{2\text{-}NPYR,OH} \times k_{PYR+OH} \times [OH]_g \times [PYR]_g$
$FLT_{(g)} + NO_{3(g)} \rightarrow 2\text{-}NFLT_{(g)}$	$Y_{2\text{-}NFLT,NO_3} \times k_{FLT+NO_3} \times [NO_3]_g \times [FLT]_g$
$2\text{-}NFLT_{(p)} + h\nu \rightarrow$ products	$\alpha \times J_{NO_2} \times [2\text{-}NFLT]_p$
$2\text{-}NPYR_{(p)} + h\nu \rightarrow$ products	$\alpha \times J_{NO_2} \times [2\text{-}NPYR]_p$

As previously noted, a key step in the formation mechanism involves competition between NO_2 and O_2 for an intermediate (Figure S1). Therefore, under ambient and particularly low NO_x conditions, one would expect the yield of these compounds to decrease and to be dependent on NO_2 concentration. The yield determined by Atkinson et al. likely represents an upper limit[66]; therefore, using the default reactivity scenario in the model might overestimate the conversion of the PAH to the NPAH under low NO_x conditions. In order to explore this uncertainty in more detail, an alternative formation scenario, in which the yields of 2-

https://dx.doi.org/10.1021/acs.est.0c04319
Environ. Sci. Technol. XXXX, XXX, XXX−XXX

Table 2. Overview of Chemical Formation and Loss Reactions in the Default Reactivity Scenario for 2-NFLT and 2-NPYR and Three Sensitivity Scenarios (α = 0.005, NO_2-Dependent Yield with α = 0.05 and NO_2-Dependent Yield with α = 0.005)[a]

parameter	default α = 0.005	α = 0.05	NO_2-dependent yield/α = 0.05	NO_2-dependent yield/α = 0.005	units
k_{FLT+OH}	1.1×10^{-11}[b]	1.1×10^{-11}	1.1×10^{-11}	1.1×10^{-11}	$cm^3\ s^{-1}$
k_{PYR+OH}	5.0×10^{-11}[c]	5.0×10^{-11}	5.0×10^{-11}	5.0×10^{-11}	$cm^3\ s^{-1}$
$k_{NFLT+NO_3}$	$0.51 \times [NO_2] \times 10^{-27}$[c]	$0.51 \times [NO_2] \times 10^{-27}$	$0.51 \times [NO_2] \times 10^{-27}$	$0.51 \times [NO_2] \times 10^{-27}$	$cm^3\ s^{-1}$
$Y_{2\text{-NFLT,OH}}$	0.03	0.03	$0.03 \times \Omega$	$0.03 \times \Omega$	
$Y_{2\text{-NPYR,OH}}$	0.005	0.005	$0.005 \times \Omega$	$0.005 \times \Omega$	
$Y_{2\text{-NFLT,NO}_3}$	0.24	0.24	$0.24 \times \Omega$	$0.24 \times \Omega$	
α	0.05[d]	0.005	0.05	0.005	

[a] k_{FLT+OH}, k_{PYR+OH}, and k_{FLT+NO_3} are the rate coefficients for each reaction, and $Y_{2\text{-NFLT,OH}}$, $Y_{2\text{-NPYR,OH}}$, and $Y_{2\text{-NFLT,NO}_3}$ are the NPAH yields. In the NO_2-dependent simulation, a scaling factor is used, $\Omega = (k_{NO_2}/k_{O_2})\ ([NO_2]_g/[O_2]_g)/(1 + (k_{NO_2}/k_{O_2})\ ([NO_2]_g/[O_2]_g))$ with $k_{NO_2}/k_{O_2} = 1 \times 10^7$. α is a factor to scale NPAH photodegradation relative to the NO_2 photolysis rate (Figure S2). [b] Brubaker and Hites, 1998.[67] [c] Atkinson et al., 1990.[66] [d] Fan et al., 1996.[71]

NFLT and 2-NPYR are dependent on NO_2 concentration, is tested (Table 2, NO_2-dependent yield). Relative rate coefficients for the reactions between the intermediate and either O_2 or NO_2 are used to create an expression for the yield as a function of NO_2 concentration (detailed in the Supporting Information, Section S1, and Table 2; the explicit dependence of yield on NO_2 can be seen in Figure S2).

2.3. Gas-Particle Partitioning and Deposition. The mass fractions of the PAH and NPAH in the gas and particle phases are set to the predicted thermodynamic gas−particle partitioning equilibrium at each model time step. These equilibrium predictions are based on an implementation of the ppLFER approach,[53,68] for which detailed information is available in the Supporting Information. The physicochemical parameters of each PAH and NPAH species used in the model are given in Table S1.

In the gas phase, atmospheric sources of semivolatile organics (besides chemical formation) are primary emissions and revolatilization from ocean and terrestrial surfaces, while their sinks are wet scavenging and dry deposition.[46] In the particle phase, the dry deposition and wet deposition of PAHs and NPAHs are treated the same as that of other particle-phase species.

2.4. Chemical Losses of 2-NFLT and 2-NPYR. The most important loss pathway of 2-NFLT and 2-NPYR is sunlight-initiated photodegradation in the particle phase.[69] The exact mechanism for these two particular NPAHs is unknown, although 1-NPYR has been shown to have a complex degradation mechanism.[70] Photolysis in the gas phase was never observed.[23] Fan et al. quantified the photodegradation rates of 2-NFLT and 2-NPYR relative to the photolysis rate of NO_2 (J_{NO_2}).[71] This was parameterized using a scaling factor α, which was determined for several types of soot particles only. For wood smoke particles, α = 0.05 was found, but on diesel soot particles, 2-NFLT and 2-NPYR were slightly less reactive, with α = 0.025 and α = 0.04, respectively.

The sole chemical sink of the atmospheric NPAH implemented in this model is photolytic degradation, which was included only for 2-NFLT and 2-NPYR in the particle phase. For the default reactivity scenario, we adopt the scaling factor from the wood smoke aerosol (α = 0.05) for 2-NFLT or 2-NPYR (Table 2). J_{NO_2} is calculated for each grid cell based on available sunlight. The constant scaling factor is applied for all aerosols, despite the fact that particulate matter (PM) composition and color strongly influence the photochemical degradation process.[70,72−75] Photolysis with different efficiencies might be expected in aged, long-range transported aerosols and in natural aerosols (sea salt, mineral dust).

We explore this uncertainty using an alternative reactivity scenario with the loss rate due to photodegradation reduced by a factor of 10 (i.e., α = 0.005, Table 2) and also simulated with photolysis switched off (α = 0).

Another possible NPAH loss reaction is the homogeneous reaction with the OH radical. Second-order rate coefficients have not been determined experimentally, but estimates are available, that is, 4.93×10^{-12} and 6.25×10^{-12} molecules $cm^{-3}\ s^{-1}$ for 2-NFLT and 2-NPYR, respectively.[76] A sensitivity run including these reactions showed only a small effect on simulation results (Figure S3). Therefore, the homogeneous reaction of NPAHs with OH is not further included in simulations.

2.5. PAH Emissions. FLT and PYR emission data of the year 2008 were used in the model simulation.[77] The total global emissions of FLT and PYR were 2.8366×10^7 and 2.1827×10^7 kg yr^{-1}, respectively. These emissions comprise fossil fuel (coal, oil, and gas), biomass, and waste combustion for energy production, industry, transportation (including ships and aircraft), and agricultural and residential sources. Emissions from industrial processes and open fires are also included in the inventory. The emissions were projected from a country-level to a global grid (with a resolution of 0.1 × 0.1°) and represented as annual sums. For the simulations, we applied monthly variation of PAH emissions following the temporal profile of emissions of BC from the Hemispheric Transport of Air Pollutants (HTAP) v2.2 data set.[78] PAHs are largely coemitted with BC.[77,79] Emissions of other gas and aerosol species were the same as those in Octaviani et al. (2019).[46]

2.6. Comparison between Observational Measurements and Simulation. The model output was compared with measurement data of 2-NFLT, 2-NPYR, FLT, and PYR at different locations, spanning the years 2000−2017 (see Table S2 for details). Ambient air concentrations of PAHs and NPAHs in North America, Europe, and Japan have decreased strongly during the 1990s because of the introduction of emission control measures.[43,80−82] Hence, we used only measurements made since the year 2000 for comparison to the simulation/emission data in this study (2006−2008).

Note that the measurement data comprise total (gas phase and particle phase) as well as particle phase-only measurements. Similarly, not all studies analyzed the same size fractions of particulate matter, and in several studies, 2-

https://dx.doi.org/10.1021/acs.est.0c04319
Environ. Sci. Technol. XXXX, XXX, XXX−XXX

NFLT data included 3-nitrofluoranthene (3-NFLT) because of chromatographic coelution.[16] However, 3-NFLT abundance in ambient air is very low and can be considered negligible with respect to 2-NFLT.[20] Nevertheless, these inconsistencies may contribute to discrepancies between the model and observations.

For comparison with observational data, the simulated near-surface concentrations of the NPAH and PAH were bilinearly interpolated between grid cells and given as a monthly mean (see the Supporting Information, Section S4). This was done for both the particle-phase only and total near-surface concentrations. Furthermore, observational sites are categorized as either rural/remote, that is, sites away from the source where sampled air is aged or from unpolluted vicinity, or urban, that is, polluted sampling sites close to the source such as cities (Table S2). Because the coarse resolution of the large-scale model is unable to resolve the subgrid level heterogeneity induced by local sources, the model systematically underestimates the measured concentration of both 2-NFLT and 2-NPYR at the sites classified as urban (Figures S2 and S3). Hence, we focus on the sites classified as rural in the further discussion. The distinction between rural and urban sites was made by analyzing keywords from the original publications. Sites described by keywords such as "city", "suburban", and "highway" are classified as urban, while those described by "rural", "background", or "remote" are denoted as rural. A full list of the keywords associated with each site and their subsequent classification are shown in the Supporting Information (Table S2). Comparisons between simulated and measured near-surface concentrations at rural and urban sites for 2-NFLT and 2-NPYR are shown in the Supporting Information (Figures S4 and S5).

The correlation coefficient (R) and modified normalized mean bias (MNMB) are used to evaluate model performance. The MNMB has been previously used to evaluate predicted atmospheric concentrations that vary across orders of magnitude.[83−85] The MNMB is calculated in the following way

$$\mathrm{MNMB} = \frac{2}{N}\sum_i \left(\frac{f_i - o_i}{f_i - o_i}\right)$$

where N is the number of simulation−observation pairs and f_i and o_i are the numerical values of simulation and observation, respectively. The MNMB may also be expressed as a percentage and can range between −200% and +200%.

3. RESULTS AND DISCUSSION

3.1. Comparison with Field Observations across the Globe. *3.1.1. Default Reactivity Scenario.* Figure 1 shows a comparison of the simulated and measured near-surface concentrations for 2-NFLT and 2-NPYR for the default reactivity scenario and three alternative scenarios with different chemical formation and degradation parameters. The measured concentrations of 2-NFLT and 2-NPYR are spread across 5 and 3 orders of magnitude, respectively (6×10^{-2} to 4×10^{3} pg m^{-3} for 2-NFLT and 1×10^{-1} to 7×10^{1} pg m^{-3} for 2-NPYR). In the default reactivity scenario (α = 0.05, indicated by blue points), we find overestimation and underestimation of 2-NFLT contained within 1 order of magnitude. The MNMB is +10%, thus indicating that the concentration of 2-NFLT is slightly overestimated by the default reactivity scenario (Table 3). The measured 2-NFLT concentrations below 10 pg m^{-3} tend to be overestimated by up to 1 order of magnitude, while

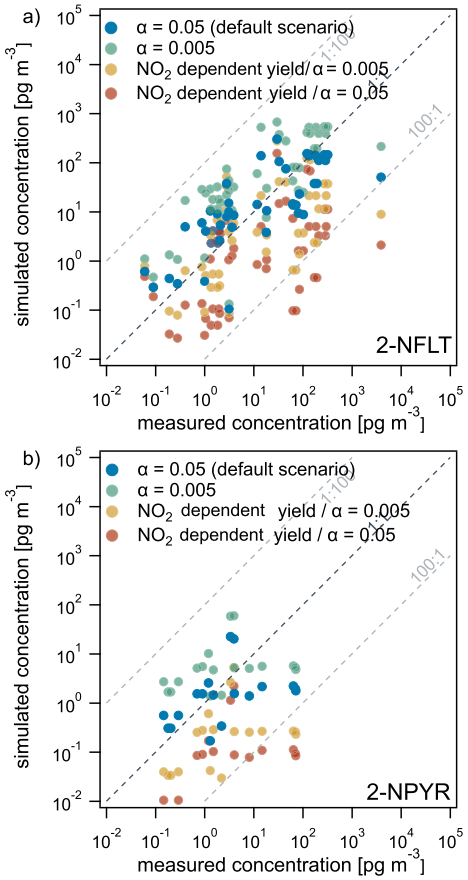

Figure 1. Comparison between simulated and measured near-surface concentrations [pg m^{-3}] at rural sites of (a) 2-NFLT and (b) 2-NPYR. The dashed lines marked 1:1, 100:1, and 1:100 represent where the measured concentrations are predicted, underestimated by a factor of 100, and overestimated by a factor of 100, respectively.

for concentrations higher than 10 pg m^{-3}, the model results are scattered above and below the 1:1 line (Figure 1a).

Importantly, FLT, the precursor to 2-NFLT, tends to be underestimated at these rural sites (Figure S6), suggesting that the true model overestimation of 2-NFLT may be even greater. In order to normalize for the effects of the parent PAH concentration, the ratio of NPAH/PAH near-surface concentrations is calculated. A comparison between the simulated and observed ratios of 2-NFLT to FLT concentration is shown (Figure 2). The default chemistry scenario systematically overestimates the 2-NFLT-to-FLT ratio and has an MNMB equal to +139% (Table 3).

Predictions of 2-NPYR using the default chemistry scenario are scattered within 1 order of magnitude above and below the 1:1 line with a small negative bias (MNMB = −27%). However, as in the case of 2-NFLT, the ratio of 2-NPYR to PYR is overestimated (MNMB = +117%).

Measurement data for observational sites where both the NPAH and the precursor PAH have been measured indicate that the NPAH/PAH ratio varies across 3 orders of magnitude (Figure 2). A spatially homogeneous ratio would indicate that the concentration of the precursor PAH is strongly correlated with the NPAH product, whereas both the measurement data and our simulation results clearly demonstrate that these ratios are highly variable. Apart from the distribution of PAH

https://dx.doi.org/10.1021/acs.est.0c04319
Environ. Sci. Technol. XXXX, XXX, XXX−XXX

Table 3. Correlation Coefficient (R; * = Significant at $P < 0.05$) and MNMB to Evaluate the Comparison between the Different Simulations and Measurement[a]

	2-NFLT$_{(p)}$		2-NFLT$_{(p)}$/FLT$_{(p)}$		2-NPYR$_{(p)}$		2-NPYR$_{(p)}$/PYR$_{(p}$	
scenario	R	MNMB (%)	R	MNMB (%)	R	MNMB (%)	R	MNMB (%)
α = 0.05	0.10	10	−0.10	+139	−0.09	−27	0.50	+117
α = 0.005	0.16	+89	−0.10	+168	−0.12	+51	0.71*	+170
NO_2-dependent yield/α = 0.05	−0.03	−115	−0.07	−2	−0.11	−173	0.19	−112
NO_2-dependent yield/α = 0.005	−0.01	−66	−0.07	+69	−0.11	−138	0.78*	−29

[a]For 2-NFLT (N = 48), 2-NFLT/FLT (N = 24), 2-NPYR (N = 18), and 2-NPYR/PYR (N = 10).

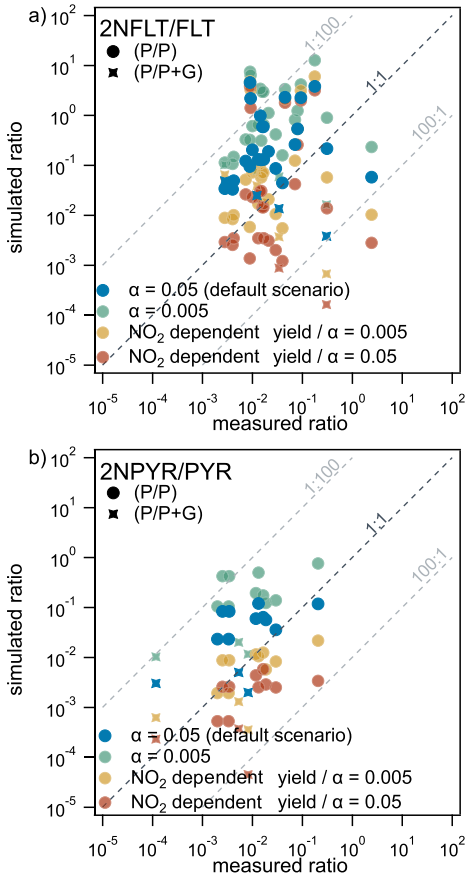

Figure 2. Comparison between the simulated and measured ratios of NPAH/PAH near-surface concentrations at rural sites of (a) 2-NFLT/FLT and (b) 2-NPYR/PYR. The dashed lines marked 1:1, 100:1, and 1:100 represent where the measured concentrations are predicted, underestimated by a factor of 100, and overestimated by a factor of 100, respectively.

emissions, NPAH variability is determined by the availability of oxidants, sunlight, NO_x, and aerosol mass concentrations (with the latter influencing the extent to which the PAH and NPAH partition between the gas and particle phases).

By dividing the global atmospheric burdens through the overall loss rates related to chemical and physical sinks, we obtain global mean atmospheric residence times of 2.6 h for 2-NFLT and 2.9 h for 2-NPYR (default reactivity scenario; Table 5). Dividing the global atmospheric burdens by the photodegradation loss rates gives photolytic lifetimes, for which we obtain global means of 2.8 h for 2-NFLT and 3.2 h for 2-NPYR. This comparison shows that the atmospheric fate of 2-NFLT and 2-NPYR under these reactivity scenarios is mostly driven by photodegradation, with significantly lower contribution from dry and wet deposition.

Given its importance, the photodegradation rate is rather poorly constrained and may strongly contribute to model uncertainty. Kinetic data describing the effects of particle composition, and possibly phase state, on heterogeneous photolysis would be needed but are not available. Quantum mechanical calculations have provided a detailed understanding of the photochemistry of 1-nitropyrene,[86,87] and similar approaches would be valuable for 2-NFLT and 2-NPYR.

3.1.2. Alternative Scenarios. To explore the overestimation bias and the lack of correlation between the simulated predictions of the default reactivity scenario and measured near-surface concentrations of 2-NFLT and 2-NPYR (Figure 1) and NPAH/PAH ratios (Figure 2), we present the results from three alternative reactivity scenarios. These include a NO_2-dependent NPAH formation scenario which should lead to a higher sensitivity of the model to local conditions, a scenario with a reduced photochemical loss of NPAH, and a combined NO_2-dependent/reduced photochemical loss scenario.

The NO_2-dependent reactivity scenarios account for reduced NPAH yields under low NO_x conditions. Their implementation leads to decreased atmospheric NPAH column densities in less polluted regions, while in regions with elevated NO_2 concentrations, the formation is similar to that in the default scenario (Figure S7). The global atmospheric burden of 2-NFLT decreases by a factor of 11, and the global atmospheric burden of 2-NPYR decreases by a factor of 48 (Table 5). Correspondingly, observed 2-NFLT and 2-NPYR concentrations are underestimated (MNMB = −115% and −173%, respectively, for α = 0; Table 3). In the source regions (Figure 1; almost all these rural sites are located in source regions), NPAH near-ground concentrations are underpredicted by up to 3 orders of magnitude, while at the remote site (Figure 3), NPAH concentrations are underpredicted by up to 1 order of magnitude. With the NO_2-dependent scenario, the MNMB of the 2-NFLT-to-FLT ratio is only −2%, which is thus much improved compared to that of the default scenario. For the 2-NPYR-to-PYR ratio, the MNMB does not improve significantly (−112%).

The two reduced photodegradation scenarios account for the large uncertainty connected with this model parameter. Slowing the rate of loss due to photodegradation by a factor of 10 leads to an increase in 2-NFLT and 2-NPYR concentrations at all observation sites (Figure 1). Relative to the default scenario (α = 0.05), this α = 0.005 scenario demonstrates even more overestimation by the model: the MNMBs are +89, +51, +168, and +170% for 2-NFLT, 2-NPYR, 2-NFLT/FLT, and 2-NPYR/PYR, respectively (Table 3, Figures 1 and 2). The only metric for which reducing the rate of photolysis resulted in a

https://dx.doi.org/10.1021/acs.est.0c04319
Environ. Sci. Technol. XXXX, XXX, XXX−XXX

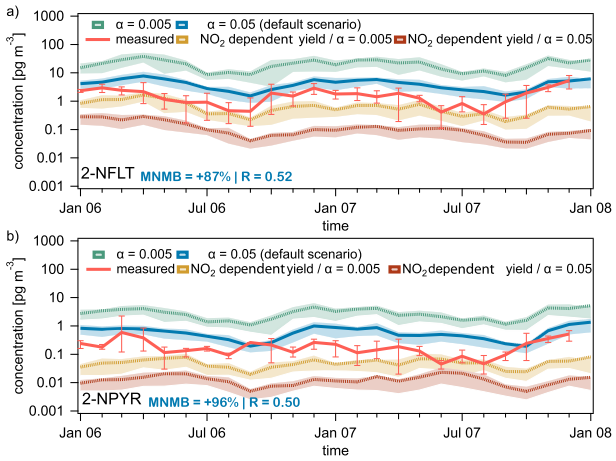

Figure 3. Comparison between simulation and observations for the Noto Peninsula in Japan (January 2006 to December 2007) for (a) 2-NFLT and (b) 2-NPYR particle-phase concentrations [pg m^{-3}]. Measurement data are from Tang et al. (2014)[88] and presented as monthly mean concentrations (solid red line). Error bars in the measurement data are the minimum and maximum weekly values for each month. The upper and lower quartiles of simulated concentrations each month are bounded by the shaded region. The modified normalized mean bias (MNMB) and Pearson correlation coefficient (R) are shown for the default simulation (α = 0.05, blue line).

statistically significant ($P < 0.05$) improvement in correlation is 2-NPYR/PYR (R = 0.71).

Note that fully neglecting photolytic degradation (α = 0, no photolysis) would lead to massive overestimation of atmospheric column densities of 2-NFLT and 2-NPYR by 2 orders of magnitude, as illustrated by a sensitivity test. Spatially, this is reflected as higher concentrations in the continental plumes from northern midlatitude and tropical source regions (Figure S7). Regions far from the source (e.g., Antarctica) tend to be the most sensitive to effects of photodegradation and have a column density of more than 3 (2-NFLT) and 4 (2-NPYR) orders of magnitude greater compared to that of the default reactivity scenario (Figure S7). In contrast, in source regions (e.g., Europe) increases are only up to 1 order of magnitude. These results demonstrate that the rate of photodegradation becomes more influential for the atmospheric column concentrations of 2-NFLT and 2-NPYR the farther air masses are transported.

Assuming both a NO_2-dependent formation of the NPAH and a low estimate for NPAH photodegradation (α = 0.005), the global atmospheric burden of 2-NFLT decreases by a factor of 3 and the global atmospheric burden of 2-NPYR decreases by a factor of 9 (Table 5), leading to underestimation of 2-NFLT and 2-NPYR concentrations (MNNB = −66 and −138%, respectively; Figure 1). However, among the four scenarios investigated, the combined NO_2-dependent/low photodegradation scenario leads to the lowest discrepancies of 2-NFLT/FLT (MNMB = −2 and +69% for α = 0.05 and 0.005, respectively) and 2-NPYR/PYR ratios (MNMB = −112 and −29% for α = 0.05 and 0.005, respectively).

In conclusion, a NO_2-dependent scenario is able to reduce some of the model overestimation that occurs for 2-NFLT in less polluted areas (discussed in Section 3.1.1 and seen in Figure 1a) and comes closest to observed NPAH/PAH ratios. Further exploration of the 2-NFLT and 2-NPYR formation kinetics at low NO_x concentrations with laboratory experiments may ultimately help to improve model performance.

3.2. Comparison with Observations at a Remote-Background Site with Long-Term Monitoring. The Wajima Air Monitoring Station on the Noto Peninsula, Japan (37°23′ N, 136°54′ E; Tang et al. 2014) represents one of very few long-term monitoring data sets of 2-NFLT and 2-NPYR and the only one at a remote-background location.[88] Remote-background locations are less likely to be influenced by strong local concentrations and are therefore particularly valuable for assessing the performance of global models. Monthly averages of 2-NFLT and 2-NPYR concentrations (Tang et al.) between January 2006 and December 2007 are shown in Figure 3 and compared with simulation predictions.

3.2.1. Default Reactivity Scenario. In the default reactivity scenario (α = 0.05), the model tends to overestimate the concentration of 2-NFLT and 2-NPYR at this site (MNMB = +87 and +96%, respectively); however, simulated particle-phase concentrations of 2-NFLT and 2-NPYR agree with measurements within 1 order of magnitude (Figure 3). For 2-NFLT, this overestimation is most prevalent in summer. The winter maximum of NPAHs (October to April) was attributed to transport from Northeast Asia, during the heating period in Northern China.[88] Measured 2-NFLT concentrations exhibit a clearer seasonal signal than 2-NPYR; the model thus captures this seasonal variability of 2-NFLT (Figure 3a, blue line, R = 0.52, $p < 0.05$) slightly better than that for 2-NPYR (Figure 3b, blue line, R = 0.50, $p < 0.05$). Throughout the 2-year period, simulated concentrations of 2-NFLT range between 2 and 8 pg m^{-3}. In agreement with measurements, the simulated concentrations of 2-NPYR are around a factor of 10 lower than those of 2-NFLT (≈0.2 to 1.4 pg m^{-3}).

The MNMB for the simulated ratio of concentrations is higher than that for absolute concentrations: 2-NFLT/FLT (+169%) and 2-NPYR/PYR (+174%). In contrast to the absolute concentration, 2-NFLT/FLT and 2-NPYR/PYR ratios show maxima in summer (Figure 4). The measured

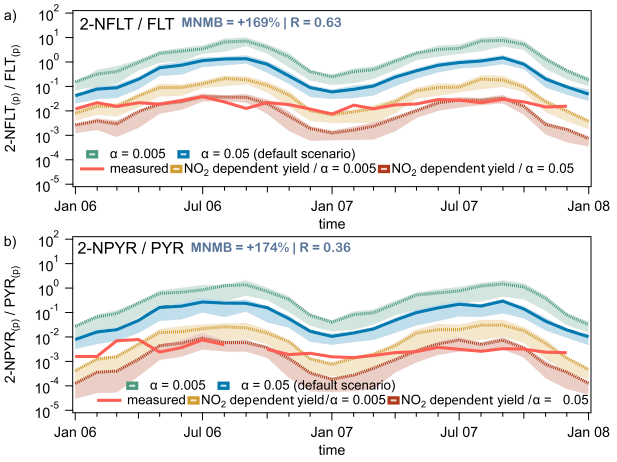

Figure 4. Comparison between simulation and observations for the Noto Peninsula in Japan (January 2006 to December 2007) for (a) 2-NFLT/FLT and (b) 2-NPYR/PYR ratio of particle-phase concentrations. Measurement data are from Tang et al. (2014)[88] and presented as monthly mean concentrations (solid red line). The modified normalized mean bias (MNMB) and Pearson correlation coefficient (R) are shown for the default simulation (α = 0.05, blue line).

https://dx.doi.org/10.1021/acs.est.0c04319
Environ. Sci. Technol. XXXX, XXX, XXX−XXX

Table 4. Correlation Coefficient (R; * = Significant at $P < 0.05$) and MNMB to Evaluate the Comparison between the Different Simulations and Measurement at the Noto Site[a]

	2-NFLT$_{(p)}$		2-NFLT$_{(p)}$/FLT$_{(p)}$		2-NPYR$_{(p)}$		2-NPYR$_{(p)}$/PYR$_{(p)}$	
scenario	R	MNMB (%)	R	MNMB (%)	R	MNMB (%)	R	MNMB (%)
α = 0.05	0.52*	+87	0.63*	+169	0.50*	+96	0.36	+174
α = 0.005	0.51*	+169	0.48*	+192	0.51*	+171	0.25	+193
NO_2-dependent yield/α = 0.05	0.21	−167	0.69*	−65	−0.02	−165	0.40	−48
NO_2-dependent yield/α = 0.005	0.30	−78	0.53*	+66	−0.01	−103	0.27	+56

[a]For 2-NFLT, 2-NFLT/FLT, 2-NPYR (N = 24), and 2-NPYR/PYR (N = 23).

ratios, calculated from the data of Tang et al.,[88] also exhibit maxima in summer but are less extreme. For example, the mean measured 2-NFLT/FLT ratios for January and July are 0.009 and 0.032, respectively. The model produces a similar pattern, with the simulated mean 2-NFLT/FLT ratios being 0.20 and 3.49 in January and July, respectively. Two processes in the model may explain the summer maxima of these ratios: (1) the increased availability of oxidants (OH and NO_3) and (2) higher temperatures causing a higher proportion of FLT and PYR to be in the gas phase and therefore convert to 2-NFLT and 2-NPYR.

PAH partitioning is crucial for the ability of the model to predict NPAH concentrations because NPAHs are formed in the gas phase but are primarily lost from the particle phase by photodegradation. Therefore, the transfer of mass between phases may be an important process controlling the atmospheric fate of the NPAH. The model predicts the near-surface gas-phase concentration of 2-NFLT and 2-NPYR to be lower compared to that in the particle phase (corresponding to a particulate mass fraction generally over 80%, even in summer). This is consistent with previous studies which have found these NPAHs almost exclusively in the particle phase.[53,89−91] The model predicts that on average over the 2-year period, only small fractions of the total mass of FLT and PYR in air are present in the particle phase (7 and 14%, respectively); in contrast, 2-NFLT and 2-NPYR are mainly associated with particles (91 and 90%, respectively). Also, the simulated parent PAH gas−particle partitioning is consistent with previous findings at other sites.[67,90,91]

3.2.2. Alternative Scenarios. The NO_2-dependent formation scenario, with default photodegradation (α = 0.05), underestimates absolute 2-NFLT and 2-NFLT concentrations at the Noto Peninsula site (Table 4, brown dotted line in Figure 3a) but better predicts 2-NFLT/FLT and 2-NPYR/PYR ratios compared to the default chemistry scenario (Table 4, brown dotted line in Figure 4). The scenario with reduced photodegradation (α = 0.005, green dotted lines in Figures 3 and 4) leads to more severe overestimation of absolute NPAH concentrations and NPAH/PAH compared to default chemistry scenario. Model performance improves when the NO_2-dependent formation scenario is used with reduced photodegradation (α = 0.005, yellow dotted line in Figures 3 and 4). A slight underestimation of absolute NPAH concentrations is still observed, but NPAH/PAH ratios are better predicted compared to the default scenario.

3.3. Global Atmospheric Burden, Near-Surface Concentrations, and Column Densities. Figure 5a shows the model-calculated near-surface concentrations of 2-NFLT and 2-NPYR averaged over 3 years, 2006−2008. They exhibit strong spatial variability, spanning over 6 orders of magnitude from near-source to remote marine environments and polar regions (from 10^{-3} to 10^{3} pg m^{-3}). The mean near-surface

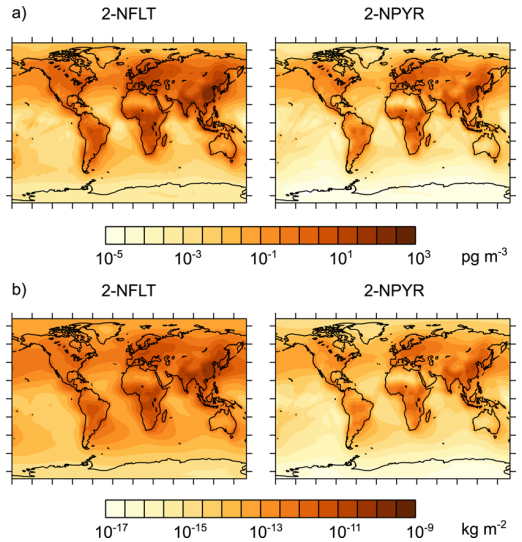

Figure 5. (a) Atmospheric concentrations at the near-surface level [pg m^{-3}] of 2-NFLT and 2-NPYR and (b) column densities [kg m^{-2}], averaged over 2006−2008, using the default reactivity scenario.

concentrations of 2-NFLT and 2-NPYR in the Arctic are ≈1 and ≈0.1 pg m^{-3}, respectively, and a factor of 3−5 higher in low-latitude remote regions such as the Amazon and Tibet. The mean concentrations of 2-NFLT and 2-NPYR over the midlatitude open North Atlantic are ≈10 and ≈1 pg m^{-3}, respectively, and 2 orders of magnitude lower over the midlatitude open North Pacific. The highest average concentration levels within a model grid cell range up to ∼1000 pg m^{-3} for 2-NFLT and ∼10 pg m^{-3} for 2-NPYR and are located in PAH source regions: Europe, Western Russia, Central Africa, and East and Southeast Asia. The simulated global mean concentrations of 2-NFLT and 2-NPYR at the near-surface level are 2.93 and 0.43 pg m^{-3}, respectively (Table 5). Between individual years, the global mean near-surface concentrations differed by less than 20% for 2-NFLT and less than 15% for 2-NPYR.

The column densities, that is, the vertically integrated concentration per unit area, of 2-NFLT and 2-NPYR exhibit a similar geographic distribution to the near-surface concentrations (Figure 5b) and range across at least 6 orders of magnitude, from 10^{-16} to 10^{-10} kg m^{-2}. The highest column densities are located in PAH source regions, ∼10^{-10} kg m^{-2} for 2-NFLT and ∼10^{-11} kg m^{-2} for 2-NPYR. The global atmospheric burdens, that is, the total masses of 2-NFLT and 2-NPYR stored in the global atmosphere, are 929 and 100 kg, respectively (averaged over 2006−2008, Table 5). These correspond to 0.7 and 0.2%, respectively, of the parent PAHs' global atmospheric burden. The global atmospheric burden

https://dx.doi.org/10.1021/acs.est.0c04319
Environ. Sci. Technol. XXXX, XXX, XXX−XXX

Table 5. Total Emission Fluxes of Precursors (FLT and PYR)[77] and Global Mean Parameters for the Atmospheric Cycling of 2-NFLT and 2-NPYR for the Years 2006−2008 (over Land/over Ocean) Using the Default Reactivity Scenario and the Three Additional Sensitivity Scenarios

species	scenario	precursor emission flux ($\times 10^3$ kg yr^{-1})	global atmospheric burden (kg)	near-surface concentration (pg m^{-3})	atmospheric residence time (h)	photolytic lifetime (h)
2-NFLT	α = 0.05	FLT: 28366 (27255/1111)	929	2.93 (8.24/0.84)	2.59	2.81
	α = 0.005		4170	10.9	17.2	27.9
	NO_2-dependent yield/α = 0.05		86.2	0.5	3.01	3.26
	NO_2-dependent yield/α = 0.005		288	1.04	18.7	31.3
2-NPYR	α = 0.05 default	PYR: 21827 (20533/1294)	100.1	0.43 (1.39/0.06)	2.87	3.15
	α = 0.005		510	1.59	18.1	30.8
	NO_2-dependent yield/α = 0.05		2.08	0.0173	2.57	2.8
	NO_2-dependent yield/α = 0.005		10.7	0.048	17.6	29.2

differed between individual years by less than 8% for 2-NFLT and less than 9% for 2-NPYR. In spite of the low mean atmospheric residence times (2.6 and 2.9 h), 2-NFLT and 2-NPYR are spread across the globe. This is due to continuous formation of the NPAHs from photochemical reactions in the atmosphere that take place as the PAH precursors are transported away from source regions (Figure 4). This can be highlighted by the lifetimes of the precursors toward their main chemical sink, homogeneous reaction with the OH radical, of approximately 24 h and 5 h for FLT and PYR, respectively (using [OH] = 1.16 × 10^6 cm^{-3} [65] with $k_{FLT\text{-}OH}$ and $k_{PYR\text{-}OH}$ in Table 2), causing the parent compounds to be transported farther than their nitrated degradation products.

Figure 6 shows the ratio of near-surface concentrations for (a) 2-NFLT to FLT and (b) 2-NPYR to PYR, averaged over the years 2006−2008. The spatial distributions of these ratios vary across the globe, ranging across at least 3 orders of magnitude. The ratio of 2-NFLT to FLT tends to be around 0.1−1% over continental source regions, whereas the highest ratio occurs in plumes being transported away from sources. Particularly high ratios occur over the ocean and in some cases exceed 10%. A similar tendency was seen for the 2-NPYR-to-PYR ratio, which is generally around 0.1% in near-source regions but increases up to 1% in plumes being transported to more remote regions.

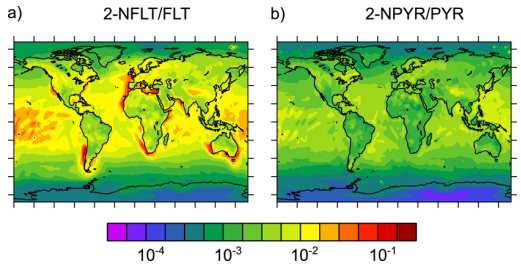

Figure 6. Ratio of NPAH to parent PAH near-surface concentrations, (a) 2-NFLT/FLT and (b) 2-NPYR/PYR, averaged over 2006−2008.

In conclusion, our model predicts the highest concentrations of 2-NFLT and 2-NPYR to be found in regions with high PAH emissions, but because of formation along long-range atmospheric transport, the two NPAHs are distributed worldwide.

■ ASSOCIATED CONTENT

Supporting Information

The Supporting Information is available free of charge at https://pubs.acs.org/doi/10.1021/acs.est.0c04319.

Further details regarding formation chemistry, partitioning, and particle-phase loss; physicochemical properties used for the model input; full list of observational sites and additional details about model evaluation; and column densities relative to the default scenario (PDF)

■ AUTHOR INFORMATION

Corresponding Authors

Thomas Berkemeier − *Multiphase Chemistry Department, Max Planck Institute for Chemistry, 55128 Mainz, Germany;* orcid.org/0000-0001-6390-6465; Email: t.berkemeier@mpic.de

Gerhard Lammel − *Multiphase Chemistry Department, Max Planck Institute for Chemistry, 55128 Mainz, Germany; Research Centre for Toxic Compounds in the Environment, Masaryk University, 62500 Brno, Czech Republic;* orcid.org/0000-0003-2313-0628; Email: g.lammel@mpic.de

Authors

Jake Wilson − *Multiphase Chemistry Department, Max Planck Institute for Chemistry, 55128 Mainz, Germany;* orcid.org/0000-0002-2342-6966

Mega Octaviani − *Multiphase Chemistry Department, Max Planck Institute for Chemistry, 55128 Mainz, Germany*

Benjamin A. Musa Bandowe − *Multiphase Chemistry Department, Max Planck Institute for Chemistry, 55128 Mainz, Germany;* orcid.org/0000-0003-0605-2285

Marco Wietzoreck − *Multiphase Chemistry Department, Max Planck Institute for Chemistry, 55128 Mainz, Germany*

Cornelius Zetzsch − *Multiphase Chemistry Department, Max Planck Institute for Chemistry, 55128 Mainz, Germany; Bayreuth Centre for Ecology and Environmental Research, University of Bayreuth, 95448 Bayreuth, Germany*

Ulrich Pöschl − *Multiphase Chemistry Department, Max Planck Institute for Chemistry, 55128 Mainz, Germany;* orcid.org/0000-0003-1412-3557

Complete contact information is available at: https://pubs.acs.org/10.1021/acs.est.0c04319

Author Contributions

[⊥]J.W. and M.O. contributed equally.

https://dx.doi.org/10.1021/acs.est.0c04319
Environ. Sci. Technol. XXXX, XXX, XXX−XXX

Notes

The authors declare no competing financial interest.

■ ACKNOWLEDGMENTS

The EMAC model simulations were performed at the Max Planck Computing and Data Facility (MPCDF), Garching, Germany. We thank the MESSy community and MESSy submodel developers for providing technical support. We thank Luc Vereecken (Research Centre Jülich) for discussion. This work was funded by the Max Planck Society (MPG) and the Czech Science Foundation (#P503 20-07117S).

■ REFERENCES

(1) Pope, C. A., III; Burnett, R. T.; Thun, M. J.; Calle, E. E.; Krewski, D.; Ito, K.; Thurston, G. D. Lung cancer, cardiopulmonary mortality, and long-term exposure to fine particulate air pollution. *JAMA* **2002**, *287*, 1132−1141.

(2) Loomis, D.; Grosse, Y.; Lauby-Secretan, B.; Ghissassi, F. E.; Bouvard, V.; Benbrahim-Tallaa, L.; Guha, N.; Baan, R.; Mattock, H.; Straif, K. The carcinogenicity of outdoor air pollution. *Lancet Oncol.* **2013**, *14*, 1262−1263.

(3) Shiraiwa, M.; Ueda, K.; Pozzer, A.; Lammel, G.; Kampf, C. J.; Fushimi, A.; Enami, S.; Arangio, A. M.; Fröhlich-Nowoisky, J.; Fujitani, Y.; Furuyama, A.; Lakey, P. S. J.; Lelieveld, J.; Lucas, K.; Morino, Y.; Pöschl, U.; Takahama, S.; Takami, A.; Tong, H.; Weber, B.; Yoshino, A.; Sato, K. Aerosol health effects from molecular to global scales. *Environ. Sci. Technol.* **2017**, *51*, 13545−13567.

(4) Lelieveld, J.; Klingmüller, K.; Pozzer, A.; Pöschl, U.; Fnais, M.; Daiber, A.; Münzel, T. Cardiovascular disease burden from ambient air pollution in Europe reassessed using novel hazard ratio functions. *Eur. Heart J.* **2019**, *40*, 1590−1596.

(5) Siak, J.; Chan, T. L.; Gibson, T. L.; Wolff, G. T. Contribution to bacterial mutagenicity from nitro-PAH compounds in ambient aerosols. *Atmos. Environ.* **1967**, *19*, 369−376.

(6) Boström, C.-E.; Gerde, P.; Hanberg, A.; Jernström, B.; Johansson, C.; Kyrklund, T.; Rannug, A.; Törnqvist, M.; Victorin, K.; Westerholm, R. Cancer risk assessment, indicators, and guidelines for polycyclic aromatic hydrocarbons in the ambient air. *Environ. Health Perspect.* **2002**, *110*, 451−499.

(7) IARC. *Diesel and Gasoline Engine Exhausts and Some Nitroarenes. IARC Monographs on the Evaluation of Carciogenic Risks to Humans*, 2014; Vol. *105*,pp 9−699.

(8) Abdel-Shafy, H. I.; Mansour, M. S. M. A review on polycyclic aromatic hydrocarbons: source, environmental impact, effect on human health and remediation. *Egypt. J. Pet.* **2016**, *25*, 107−123.

(9) Misaki, K.; Takamura-Enya, T.; Ogawa, H.; Takamori, K.; Yanagida, M. Tumour-promoting activity of polycyclic aromatic hydrocarbons and their oxygenated or nitrated derivatives. *Mutagenesis* **2016**, *31*, 205−213.

(10) Idowu, O.; Semple, K. T.; Ramadass, K.; O'Connor, W.; Hansbro, P.; Thavamani, P. Beyond the obvious: environmental health implications of polar polycyclic aromatic hydrocarbons. *Environ. Int.* **2019**, *123*, 543−557.

(11) Rosenkranz, H. S.; Mermelstein, R. Mutagenicity and genotoxicity of nitroarenes. *Mutat. Res., Rev. Genet. Toxicol.* **1983**, *114*, 217−267.

(12) Feilberg, A.; Kamens, R. M.; Strommen, M. R.; Nielsen, T. Modeling the formation, decay, and partitioning of semivolatile nitro-polycyclic aromatic hydrocarbons (nitronaphthalenes) in the atmosphere. *Atmos. Environ.* **1999**, *33*, 1231−1243.

(13) Finlayson-Pitts, B. J.; Pitts, J. N. *Chemistry of the Upper and Lower Atmosphere*; Academic Press: San Diego, USA, 2000; 969 pp.

(14) Kielhorn, J.; Wahnschaffe, U.; Mangelsdorf, I. *Selected Nitro- and Nitro-Oxy-Polycyclic Aromatic Hydrocarbons*; World Health Organization, 2003.

(15) Albinet, A.; Leoz-Garziandia, E.; Budzinski, H.; Villenave, E. Polycyclic aromatic hydrocarbons (PAHs), nitrated PAHs and oxygenated PAHs in ambient air of the Marseilles area (South of France): concentrations and sources. *Sci. Total Environ.* **2007**, *384*, 280−292.

(16) Bandowe, B. A. M.; Meusel, H. Nitrated polycyclic aromatic hydrocarbons (nitro-PAHs) in the environment − a review. *Sci. Total Environ.* **2017**, *581*−*582*, 237−257.

(17) Geier, M. C.; Chlebowski, A. C.; Truong, L.; Massey Simonich, S. L.; Anderson, K. A.; Tanguay, R. L. Comparative developmental toxicity of a comprehensive suite of polycyclic aromatic hydrocarbons. *Arch. Toxicol.* **2018**, *92*, 571−586.

(18) Rosenkranz, H. S. Direct-acting mutagens in diesel exhausts: Magnitude of the problem. *Mutat. Res.* **1982**, *101*, 1−10.

(19) Salmeen, I.; Durisin, A. M.; Prater, T. J.; Riley, T.; Schuetzle, D. Contribution of 1-nitropyrene to direct-acting Ames assay mutagenicities of diesel particulate extracts. *Mutat. Res. Lett.* **1982**, *104*, 17−23.

(20) Bamford, H. A.; Bezabeh, D. Z.; Schantz, M. M.; Wise, S. A.; Baker, J. E. Determination and comparison of nitrated-polycyclic aromatic hydrocarbons measured in air and diesel particulate reference materials. *Chemosphere* **2003**, *50*, 575−587.

(21) Bamford, H. A.; Baker, J. E. Nitro-polycyclic aromatic hydrocarbon concentrations and sources in urban and suburban atmospheres of the Mid-Atlantic region. *Atmos. Environ.* **2003**, *37*, 2077−2091.

(22) Kameda, T.; Takenaka, N.; Bandow, H.; Inazu, K.; Hisamatsu, Y. Determination of atmospheric nitro-polycyclic aromatic hydrocarbons and their precursors at a heavy traffic roadside and at a residential area in Osaka, Japan. *Polycyclic Aromat. Compd.* **2004**, *24*, 657−666.

(23) Reisen, F.; Arey, J. Atmospheric reactions influence seasonal PAH and nitro-PAH concentrations in the Los Angeles Basin. *Environ. Sci. Technol.* **2005**, *39*, 64−73.

(24) Zimmermann, K.; Jariyasopit, N.; Massey Simonich, S. L.; Tao, S.; Atkinson, R.; Arey, J. Formation of nitro-PAHs from the heterogeneous reaction of ambient particle-bound PAHs with N_2O_5/NO_3/NO_2. *Environ. Sci. Technol.* **2013**, *47*, 8434−8442.

(25) Huang, B.; Liu, M.; Bi, X.; Chaemfa, C.; Ren, Z.; Wang, X.; Sheng, G.; Fu, J. Phase distribution, sources and risk assessment of PAHs, NPAHs and OPAHs in a rural site of Pearl River Delta Region, China. *Atmos. Pollut. Res.* **2014**, *5*, 210−218.

(26) Li, X.; Zheng, Y.; Guan, C.; Cheung, C. S.; Huang, Z. Effect of biodiesel on PAH, OPAH, and NPAH emissions from a direct injection diesel engine. *Environ. Sci. Pollut. Res.* **2018**, *25*, 34131−34138.

(27) Zimmermann, K.; Atkinson, R.; Arey, J.; Kojima, Y.; Inazu, K. Isomer distributions of molecular weight 247 and 273 nitro-PAHs in ambient samples, NIST Diesel SRM, and from radical-initiated chamber reactions. *Atmos. Environ.* **2012**, *55*, 431−439.

(28) Zhao, J.; Zhang, Y.; Chang, J.; Peng, S.; Hong, N.; Hu, J.; Lv, J.; Wang, T.; Mao, H. Emission characteristics and temporal variation of PAHs and their derivatives from an ocean-going cargo vessel. *Chemosphere* **2020**, *249*, 126194.

(29) Huang, W.; Huang, B.; Bi, X.; Lin, Q.; Liu, M.; Ren, Z.; Zhang, G.; Wang, X.; Sheng, G.; Fu, J. Emission of PAHs, NPAHs and OPAHs from residential honeycomb coal briquette combustion. *Energy Fuels* **2014**, *28*, 636−642.

(30) Nalin, F.; Golly, B.; Besombes, J.-L.; Pelletier, C.; Aujay-Plouzeau, R.; Verlhac, S.; Dermigny, A.; Fievet, A.; Karoski, N.; Dubois, P.; Collet, S.; Favez, O.; Albinet, A. Fast oxidation processes from emission to ambient air introduction of aerosol emitted by residential log wood stoves. *Atmos. Environ.* **2016**, *143*, 15−26.

(31) Orakij, W.; Chetiyanukornkul, T.; Kasahara, C.; Boongla, Y.; Chuesaard, T.; Furuuchi, M.; Hata, M.; Tang, N.; Hayakawa, K.; Toriba, A. Polycyclic aromatic hydrocarbons and their nitro derivatives from indoor biomass-fueled cooking in two rural areas of Thailand: a case study. *Air Qual Atmos Hlth* **2017**, *10*, 747−761.

(32) Howard, P. C.; Hecht, S. S.; Beland, F. A. *Nitroarenes: Occurrence, Metabolism, and Biological Impact*; Springer Science & Business Media, 1990.

https://dx.doi.org/10.1021/acs.est.0c04319
Environ. Sci. Technol. XXXX, XXX, XXX−XXX

(33) Yaffe, D.; Cohen, Y.; Arey, J.; Grosovsky, A. J. Multimedia analysis of PAHs and nitro-PAH daughter products in the Los Angeles Basin. *Risk Anal.* **2001**, *21*, 275−294.
(34) Ciccioli, P.; Cecinato, A.; Brancaleoni, E.; Frattoni, M.; Zacchei, P.; Miguel, A. H.; de Castro Vasconcellos, P. Formation and transport of 2-nitrofluoranthene and 2-nitropyrene of photochemical origin in the troposphere. *J. Geophys. Res.* **1996**, *101*, 19567.
(35) Nielsen, T.; Seitz, B.; Ramdahl, T. Occurrence of nitro-PAH in the atmosphere in a rural area. *Atmos. Environ.* **1984**, *18*, 2159−2165.
(36) Tsapakis, M.; Stephanou, E. G. Diurnal cycle of PAHs, nitro-PAHs, and oxy-PAHs in a high oxidation capacity marine background atmosphere. *Environ. Sci. Technol.* **2007**, *41*, 8011−8017.
(37) Lammel, G.; Mulder, M. D.; Shahpoury, P.; Kukučka, P.; Lišková, H.; Přibylová, P.; Prokeš, R.; Wotawa, G. Nitro-polycyclic aromatic hydrocarbons - gas-particle partitioning, mass size distribution, and formation along transport in marine and continental background air. *Atmos. Chem. Phys.* **2017**, *17*, 6257−6270.
(38) Becker, S.; Halsall, C. J.; Tych, W.; Hung, H.; Attewell, S.; Blanchard, P.; Li, H.; Fellin, P.; Stern, G.; Billeck, B.; Friesen, S. Resolving the long-term trends of polycyclic aromatic hydrocarbons in the Canadian Arctic atmosphere. *Environ. Sci. Technol.* **2006**, *40*, 3217−3222.
(39) Lohmann, R.; Klanova, J.; Pribylova, P.; Liskova, H.; Yonis, S.; Bollinger, K. PAHs on a West-to-East transect across the tropical Atlantic Ocean. *Environ. Sci. Technol.* **2013**, *47*, 2570−2578.
(40) Ramdahl, T.; Zielinska, B.; Arey, J.; Atkinson, R.; Winer, A. M.; Pitts, J. N., Jr. Ubiquitous occurrence of 2-nitroftuoranthene and 2-nitropyrene in air. *Nature* **1986**, *321*, 425−427.
(41) Fan, Z.; Chen, D.; Birla, P.; Kamens, R. M. Modeling of nitro-polycyclic aromatic hydrocarbon formation and decay in the atmosphere. *Atmos. Environ.* **1995**, *29*, 1171−1181.
(42) Mulder, M. D.; Dumanoglu, Y.; Efstathiou, C.; Kukučka, P.; Matejovičová, J.; Maurer, C.; Přibylová, P.; Prokeš, R.; Sofuoglu, A.; Sofuoglu, S. C.; Wilson, J.; Zetzsch, C.; Wotawa, G.; Lammel, G. Fast formation of nitro-PAHs in the marine atmosphere constrained in a regional-scale Lagrangian field experiment. *Environ. Sci. Technol.* **2019**, *53*, 8914−8924.
(43) Huang, L.; Batterman, S. A. Multimedia model for polycyclic aromatic hydrocarbons (PAHs) and nitro-PAHs in Lake Michigan. *Environ. Sci. Technol.* **2014**, *48*, 13817−13825.
(44) Schulte, J. K.; Fox, J. R.; Oron, A. P.; Larson, T. V.; Simpson, C. D.; Paulsen, M.; Beaudet, N.; Kaufman, J. D.; Magzamen, S. Neighborhood-scale spatial models of diesel exhaust concentration profile using 1-nitropyrene and other nitroarenes. *Environ. Sci. Technol.* **2015**, *49*, 13422−13430.
(45) Lin, Y.; Qiu, X.; Ma, Y.; Ma, J.; Zheng, M.; Shao, M. Concentrations and spatial distribution of polycyclic aromatic hydrocarbons (PAHs) and nitrated PAHs (NPAHs) in the atmosphere of North China, and the transformation from PAHs to NPAHs. *Environ. Pollut.* **2015**, *196*, 164−170.
(46) Octaviani, M.; Tost, H.; Lammel, G. Global simulation of semivolatile organic compounds − development and evaluation of the MESSy submodel SVOC (v1.0). *Geosci. Model Dev.* **2019**, *12*, 3585−3607.
(47) Jöckel, P.; Tost, H.; Pozzer, A.; Brühl, C.; Buchholz, J.; Ganzeveld, L.; Hoor, P.; Kerkweg, A.; Lawrence, M. G.; Sander, R.; Steil, B.; Stiller, G.; Tanarhte, M.; Taraborrelli, D.; van Aardenne, J.; Lelieveld, J. The atmospheric chemistry general circulation model ECHAM5/MESSy1: Consistent simulation of ozone from the surface to the mesosphere. *Atmos. Chem. Phys.* **2006**, *6*, 5067−5104.
(48) Jöckel, P.; Kerkweg, A.; Pozzer, A.; Sander, R.; Tost, H.; Riede, H.; Baumgaertner, A.; Gromov, S.; Kern, B. Development cycle 2 of the Modular Earth Submodel System (MESSy2). *Geosci. Model Dev.* **2010**, *3*, 717−752.
(49) Sander, R.; Baumgaertner, A.; Gromov, S.; Harder, H.; Jöckel, P.; Kerkweg, A.; Kubistin, D.; Regelin, E.; Riede, H.; Sandu, A.; Taraborrelli, D.; Tost, H.; Xie, Z.-Q. The atmospheric chemistry box model CAABA/MECCA-3.0. *Geosci. Model Dev.* **2011**, *4*, 373−380.
(50) Tost, H.; Jöckel, P.; Kerkweg, A.; Sander, R.; Lelieveld, J. Technical note: A new comprehensive SCAVenging submodel for global atmospheric chemistry modelling. *Atmos. Chem. Phys.* **2006**, *6*, 565−574.
(51) Kerkweg, A.; Buchholz, J.; Ganzeveld, L.; Pozzer, A.; Tost, H.; Jöckel, P. Technical note: An implementation of the dry removal processes DRY DEPosition and SEDImentation in the modular Earth submodel system (MESSy). *Atmos. Chem. Phys.* **2006**, *6*, 4617−4632.
(52) Pringle, K. J.; Tost, H.; Message, S.; Steil, B.; Giannadaki, D.; Nenes, A.; Fountoukis, C.; Stier, P.; Vignati, E.; Lelieveld, J. Description and evaluation of GMXe: A new aerosol submodel for global simulations (V1). *Geosci. Model Dev.* **2010**, *3*, 391−412.
(53) Tomaz, S.; Shahpoury, P.; Jaffrezo, J.-L.; Lammel, G.; Perraudin, E.; Villenave, E.; Albinet, A. One-year study of polycyclic aromatic compounds at an urban site in Grenoble (France): Seasonal variations, gas/particle partitioning and cancer risk estimation. *Sci. Total Environ.* **2016**, *565*, 1071−1083.
(54) Albinet, A.; Leoz-Garziandia, E.; Budzinski, H.; Villenave, E.; Jaffrezo, J.-L. Nitrated and oxygenated derivatives of polycyclic aromatic hydrocarbons in the ambient air of two French alpine valleys Part 2: Particle size distribution. *Atmos. Environ.* **2008**, *42*, 55−64.
(55) Ringuet, J.; Leoz-Garziandia, E.; Budzinski, H.; Villenave, E.; Albinet, A. Particle size distribution of nitrated and oxygenated polycyclic aromatic hydrocarbons (NPAHs and OPAHs) on traffic and suburban sites of a European megacity: Paris (France). *Atmos. Chem. Phys.* **2012**, *12*, 8877−8887.
(56) Kitanovski, Z.; Shahpoury, P.; Samara, C.; Voliotis, A.; Lammel, G. Composition and mass size distribution of nitrated and oxygenated aromatic compounds in ambient particulate matter from Southern and Central Europe − implications for the origin. *Atmos. Chem. Phys.* **2020**, *20*, 2471−2487.
(57) Lammel, G.; Kitanovski, Z.; Kukučka, P.; Novák, J.; Arangio, A. M.; Codling, G. P.; Filippi, A.; Hovorka, J.; Kuta, J.; Leoni, C.; Příbylová, P.; Prokeš, R.; Sáňka, O.; Shahpoury, P.; Tong, H.; Wietzoreck, M. Oxygenated and nitrated polycyclic aromatic hydrocarbons in ambient air—levels, phase partitioning, mass size distributions, and inhalation bioaccessibility. *Environ. Sci. Technol.* **2020**, *54*, 2615−2625.
(58) Dee, D. P.; Uppala, S. M.; Simmons, A. J.; Berrisford, P.; Poli, P.; Kobayashi, S.; Andrae, U.; Balmaseda, M. A.; Balsamo, G.; Bauer, P.; Bechtold, P.; Beljaars, A. C. M.; van de Berg, L.; Bidlot, J.; Bormann, N.; Delsol, C.; Dragani, R.; Fuentes, M.; Geer, A. J.; Haimberger, L.; Healy, S. B.; Hersbach, H.; Hólm, E. V.; Isaksen, L.; Kållberg, P.; Köhler, M.; Matricardi, M.; McNally, A. P.; Monge-Sanz, B. M.; Morcrette, J.-J.; Park, B.-K.; Peubey, C.; de Rosnay, P.; Tavolato, C.; Thépaut, J.-N.; Vitart, F. The ERA-Interim reanalysis: Configuration and performance of the data assimilation System. *Q. J. R. Meteorol. Soc.* **2011**, *137*, 553−597.
(59) Miet, K.; le Menach, K.; Flaud, P.-M.; Budzinski, H.; Villenave, E. Heterogeneous reactivity of pyrene and 1-nitropyrene with NO2: Kinetics, product yields and mechanism. *Atmos. Environ.* **2009**, *43*, 837−843.
(60) Cochran, R. E.; Jeong, H.; Haddadi, S.; Fisseha Derseh, R.; Gowan, A.; Beránek, J.; Kubátová, A. Identification of products formed during the heterogeneous nitration and ozonation of polycyclic aromatic hydrocarbons. *Atmos. Environ.* **2016**, *128*, 92−103.
(61) Kameda, T.; Azumi, E.; Fukushima, A.; Tang, N.; Matsuki, A.; Kamiya, Y.; Toriba, A.; Hayakawa, K. Mineral dust aerosols Promote the formation of toxic nitropolycyclic aromatic compounds. *Sci. Rep.* **2016**, *6*, 24427.
(62) Cazoir, D.; Brigante, M.; Ammar, R.; D'Anna, B.; George, C. Heterogeneous photochemistry of gaseous NO2 on solid fluoranthene films: A source of gaseous nitrous acid (HONO) in the urban environment. *J. Photochem. Photobiol., A* **2014**, *273*, 23−28.
(63) Zhang, P.; Sun, W.; Li, N.; Wang, Y.; Shu, J.; Yang, B.; Dong, L. Effects of Humidity and [NO3]/[N2O5] Ratio on the Heterogeneous Reaction of Fluoranthene and Pyrene with N2O5/NO3/NO2. *Environ. Sci. Technol.* **2014**, *48*, 13130−13137.

https://dx.doi.org/10.1021/acs.est.0c04319
Environ. Sci. Technol. XXXX, XXX, XXX−XXX

(64) Zhang, P.; Sun, W.; Yang, B.; Shu, J.; Dong, L. Effect of the blocked-sites phenomenon on the heterogeneous reaction of pyrene with N2O5/NO3/NO2. *RSC Adv.* **2016**, *6*, 10358−10364.
(65) Atkinson, R.; Arey, J. Mechanisms of the gas-phase reactions of aromatic hydrocarbons and PAHs with OH and NO_3 radicals. *Polycyclic Aromat. Compd.* **2007**, *27*, 15−40.
(66) Atkinson, R.; Arey, J.; Zielinska, B.; Aschmann, S. M. Kinetics and nitro-products of the gas-phase OH and NO_3 radical-initiated reactions of naphthalene-d8, fluoranthene-d10, and pyrene. *Int. J. Chem. Kinet.* **1990**, *22*, 999−1014.
(67) Brubaker, W. W.; Hites, R. OH reaction kinetics of polycyclic aromatic hydrocarbons and polychlorinated dibenzo-p-dioxins and dibenzofurans. *J. Phys. Chem. A* **1998**, *102*, 915−921.
(68) Shahpoury, P.; Lammel, G.; Albinet, A.; Sofuoğlu, A.; Dumanoğlu, Y.; Sofuoğlu, S. C.; Wagner, Z.; Ždimal, V. Evaluation of a conceptual model for gas-particle partitioning of polycyclic aromatic hydrocarbons using polyparameter linear free energy relationships. *Environ. Sci. Technol.* **2016**, *50*, 12312−12319.
(69) Arce, R.; Pino, E. F.; Valle, C.; Ágreda, J. Photophysics and photochemistry of 1-nitropyrene. *J. Phys. Chem. A* **2008**, *112*, 10294−10304.
(70) García-Berríos, Z. I.; Arce, R. Photodegradation mechanisms of 1-nitropyrene, an environmental pollutant: The effect of organic solvents, water, oxygen, phenols, and polycyclic aromatics on the destruction and product yields. *J. Phys. Chem. A* **2012**, *116*, 3652−3664.
(71) Fan, Z.; Kamens, R. M.; Hu, J.; Zhang, J.; McDow, S. Photostability of nitro-polycyclic aromatic hydrocarbons on combustion soot particles in sunlight. *Environ. Sci. Technol.* **1996**, *30*, 1358−1364.
(72) Feilberg, A.; Nielsen, T. Effect of aerosol chemical composition on the photodegradation of nitro-polycyclic aromatic hydrocarbons. *Environ. Sci. Technol.* **2000**, *34*, 789−797.
(73) Plaza-Medina, E. F.; Rodríguez-Córdoba, W.; Peon, J. Role of upper triplet states on the photophysics of nitrated polyaromatic compounds: S(1) lifetimes of singly nitrated pyrenes. *J. Phys. Chem. A* **2011**, *115*, 9782−9789.
(74) García-Berríos, Z. I.; Arce, R.; Burgos-Martínez, M.; Burgos-Polanco, N. D. Phototransformations of environmental contaminants in models of the aerosol: 2 and 4-nitropyrene. *J. Photochem. Photobiol., A* **2017**, *332*, 131−140.
(75) Warner, S. D.; Farant, J.-P.; Butler, I. S. Photochemical degradation of selected nitropolycyclic aromatic hydrocarbons in solution and adsorbed to solid particles. *Chemosphere* **2004**, *54*, 1207−1215.
(76) *AOPWIN of Estimation Programs Interface suite for Microsoft Windows, v4.11*; US Environmental Protection Agency, 2012.
(77) Shen, H.; Huang, Y.; Wang, R.; Zhu, D.; Li, W.; Shen, G.; Wang, B.; Zhang, Y.; Chen, Y.; Lu, Y.; Chen, H.; Li, T.; Sun, K.; Li, B.; Liu, W.; Liu, J.; Tao, S. Global atmospheric emissions of polycyclic aromatic hydrocarbons from 1960 to 2008 and future predictions. *Environ. Sci. Technol.* **2013**, *47*, 6415−6424.
(78) Janssens-Maenhout, G.; Crippa, M.; Guizzardi, D.; Dentener, F.; Muntean, M.; Pouliot, G.; Keating, T.; Zhang, Q.; Kurokawa, J.; Wankmüller, R.; Denier van der Gon, H.; Kuenen, J. J. P.; Klimont, Z.; Frost, G.; Darras, S.; Koffi, B.; Li, M. HTAP_v2.2: A mosaic of regional and global emission grid maps for 2008 and 2010 to study hemispheric transport of air pollution. *Atmos. Chem. Phys.* **2015**, *15*, 11411−11432.
(79) Lammel, G.; Sehili, A. M.; Bond, T. C.; Feichter, J.; Grassl, H. Gas/particle partitioning and global distribution of polycyclic aromatic hydrocarbons − a modelling approach. *Chemosphere* **2009**, *76*, 98−106.
(80) EEA. *European Union Emission Inventory Report 1990−2016 under the UNECE Convention on Long-Range Transboundary Air Pollution (LRTAP)*; European Environment Agency: Copenhagen, Rep. No 6/18, 2018.
(81) Hayakawa, K. Environmental behaviors and toxicities of polycyclic aromatic hydrocarbons and nitropolycyclic aromatic hydrocarbons. *Chem. Pharm. Bull.* **2016**, *64*, 83−94.
(82) Hayakawa, K.; Tang, N.; Nagato, E. G.; Toriba, A.; Sakai, S.; Kano, F.; Goto, S.; Endo, O.; Arashidani, K.-i.; Kakimoto, H. Long term trends in atmospheric concentrations of polycyclic aromatic hydrocarbons and nitropolycyclic aromatic hydrocarbons: A study of Japanese cities from 1997 to 2014. *Environ. Pollut.* **2018**, *233*, 474−482.
(83) Elguindi, N.; Clark, H.; Ordóñez, C.; Thouret, V.; Flemming, J.; Stein, O.; Huijnen, V.; Moinat, P.; Inness, A.; Peuch, V.-H.; Stohl, A.; Turquety, S.; Athier, G.; Cammas, J.-P.; Schultz, M. Current status of the ability of the GEMS/MACC models to reproduce the tropospheric CO vertical distribution as measured by MOZAIC. *Geosci. Model Dev.* **2010**, *3*, 501−518.
(84) Wagner, A.; Blechschmidt, A.-M.; Bouarar, I.; Brunke, E.-G.; Clerbaux, C.; Cupeiro, M.; Cristofanelli, P.; Eskes, H.; Flemming, J.; Flentje, H.; George, M.; Gilge, S.; Hilboll, A.; Inness, A.; Kapsomenakis, J.; Richter, A.; Ries, L.; Spangl, W.; Stein, O.; Weller, R.; Zerefos, C. Evaluation of the MACC operational forecast system − potential and challenges of global near-real-time modelling with respect to reactive gases in the Troposphere. *Atmos. Chem. Phys.* **2015**, *15*, 14005−14030.
(85) Shrivastava, M.; Lou, S.; Zelenyuk, A.; Easter, R. C.; Corley, R. A.; Thrall, B. D.; Rasch, P. J.; Fast, J. D.; Massey Simonich, S. L.; Shen, H.; Tao, S. Global long-range transport and lung cancer risk from polycyclic aromatic hydrocarbons shielded by coatings of organic aerosol. *Proc. Natl. Acad. Sci. U.S.A.* **2017**, *114*, 1246−1251.
(86) Giussani, A. Toward the Understanding of the photophysics and photochemistry of 1-nitronaphthalene under solar radiation: The first theoretical evidence of a photodegradation intramolecular rearrangement mechanism involving the triplet states. *J. Chem. Theory Comput.* **2014**, *10*, 3987−3995.
(87) Giussani, A.; Worth, G. A. Insights into the complex photophysics and photochemistry of the simplest nitroaromatic compound: A CASPT2//CASSCF study on nitrobenzene. *J. Chem. Theory Comput.* **2017**, *13*, 2777−2788.
(88) Tang, N.; Sato, K.; Tokuda, T.; Tatematsu, M.; Hama, H.; Suematsu, C.; Kameda, T.; Toriba, A.; Hayakawa, K. Factors affecting atmospheric 1-, 2-nitropyrenes and 2-nitrofluoranthene in winter at Noto peninsula, a remote background site, Japan. *Chemosphere* **2014**, *107*, 324−330.
(89) Arey, J.; Zielinska, B.; Atkinson, R.; Winer, A. M. Polycyclic aromatic hydrocarbon and nitroarene concentrations in ambient air during a wintertime high-NO_x episode in the Los Angeles Basin. *Atmos. Environ.* **1967**, *21*, 1437−1444.
(90) Atkinson, R.; Arey, J. Atmospheric chemistry of gas-phase polycyclic aromatic hydrocarbons: Formation of atmospheric mutagens. *Environ. Health Perspect.* **1994**, *102*, 117−126.
(91) Albinet, A.; Leoz-Garziandia, E.; Budzinski, H.; Villenave, E.; Jaffrezo, J.-L. Nitrated and oxygenated derivatives of polycyclic aromatic hydrocarbons in the ambient air of two French alpine valleys. Part 1: Concentrations, sources and gas/particle partitioning. *Atmos. Environ.* **2008**, *42*, 43−54.

https://dx.doi.org/10.1021/acs.est.0c04319
Environ. Sci. Technol. XXXX, XXX, XXX−XXX

Supporting Information

Modeling the Formation, Degradation and Spatiotemporal Distribution of 2-Nitrofluoranthene and 2-Nitropyrene in the Global Atmosphere

Jake Wilson[1,‡], Mega Octaviani[1,†,‡], Benjamin A. Musa Bandowe[1], Marco Wietzoreck[1], Cornelius Zetzsch[1,2], Ulrich Pöschl[1], Thomas Berkemeier[1,*], Gerhard Lammel[1,3,*]

[1] Multiphase Chemistry Department, Max Planck Institute for Chemistry, 55128 Mainz Germany

[2] Bayreuth Centre for Ecology and Environmental Research, University of Bayreuth, 95448 Bayreuth, Germany

[3] Masaryk University, Research Centre for Toxic Compounds in the Environment, Kamenice 5, 62500 Brno, Czech Republic

[†] Now at Pacific Northwest National Laboratory, Richland, Washington 99352, United States

[‡] Equal contribution

* Corresponding authors: Gerhard Lammel (g.lammel@mpic.de), Thomas Berkemeier (t.berkemeier@mpic.de)

Content including: 24 pages, 2 tables and 7 figures

Contents of Supporting Information

Additional information

Tables

Figures

S1. Formation Chemistry of 2-NFLT and 2-NPYR

$Y_{2\text{-NFLT,OH}}$, $Y_{2\text{-NPYR,OH}}$ and $Y_{2\text{-NFLT,NO3}}$ is the total yield of either 2-nitrofluoranthene (2-NFLT) or 2-nitroyprene (2-NPYR) from the amount consumed of fluoranthene (FLT) or pyrene (PYR), by their respective reactions. Experimental values can be seen in Table S1 and ranged between 0.5-24%.[1] One key factor contributing to this value of total yield is the % conversion of the PAH-radical adduct into NPAH (reaction with NO_2) instead of other oxygenated products (reaction with O_2) (Fig. S1). Several other factors conflate to reduce the empirical $Y_{NPAH/PAH}$ of 2-NFLT and 2-NPYR. These likely include: (1) further reaction and loss of NPAH and (2) formation of other NPAH isomers. The contribution of (2) may be estimated from the theoretical calculations of Zhang et al. (2014), by accounting for the fact that only certain adducts may lead to the formation of 2-NFLT or 2-NPYR (≈ 20-60%).[2]

Initial radical addition is described by experimentally determined rate coefficients (Table S1).[1] The kinetics of reaction of FLT with OH has been measured by Brubaker and Hites.[3] These rate coefficients are in reasonable agreement with theoretical calculations for the reaction of OH and NO_3 at specific positions on FLT and PYR.[2] Notably, the rate of reaction between FLT and NO_3 is dependent on NO_2.

With respect to fate of the PAH-radical adduct, Ghigo et al. (2006), calculated theoretically the ratio k_{NO2}/k_{O2} of rate coefficients for benzene and naphthalene (9×10^3 and 8×10^4 respectively).[4] This is in good agreement with the experimentally determined value, 3.6×10^4, for $k_{NO2\text{-naphthalene}}/k_{O2\text{-benzene}}$ (i.e. rate coefficient for reaction with NO_2 and O_2 is for the naphthalene- and benzene-OH adducts, respectively).[5–7] The ratio k_{NO2}/k_{O2} for the pyrene-OH and pyrene-NO_3 adducts were calculated as 5×10^9 and 2×10^9, respectively.[4] By using the concentration of NO_2 and O_2, an analytical expression for the yield scaling factor (Ω) may be obtained from the ratio of rate coefficients k_{NO2}/k_{O2} (equation 1). In the NO_2-dependent scheme, the yield scaling factor is multiplied by the empirically determined yield to ensure that (a) the model yield is equivalent to the empirically determined one at high NO_2 concentrations and (b) decreases towards lower NO_2 concentrations.

$$(1)\ \Omega = (k_{NO2}/k_{O2})(\ [NO_2] / [O_2])\ /\ (1 + (k_{NO2}/k_{O2})(\ [NO_2] / [O_2])\ )$$

Results from a sensitivity study using a formation scheme in which $Y_{2\text{-NFLT,OH}}$, $Y_{2\text{-NPYR,OH}}$ and $Y_{2\text{-NFLT,NO3}}$ were dependent on NO_2 are shown in Fig. S2. In this scheme the value of k_{NO2}/k_{O2} was set as 1×10^7 (see Table S1). The dependence of $Y_{2\text{-NFLT,OH}}$, $Y_{2\text{-NPYR,OH}}$ and $Y_{2\text{-NFLT,NO3}}$ on NO_2 in this scheme is shown (Fig. S5) as well as the spatial distribution of $Y_{2\text{-NFLT,OH}}$ for an illustrative month (Fig. S6).

S2. Partitioning Between Gas and Particle Phase

Semi-volatile compounds are distributed to significant mass fractions between the particle and gas phases of aerosols. Polyparameter linear free energy relationships (ppLFERs) are suitable to predict the mass distribution of NPAHs.[8] Experimentally determined ppLFER solute specific descriptors for 1-nitropyrene are used in the model.[9] These parameters are expected to be reasonably well representative for both 2-NFLT and 2-NPYR. Phase equilibrium is re-established at each model time step (30 min).

S3. Particle-phase Loss of 2-NFLT and 2-NPYR

In the gas-phase, NPAHs are generally less reactive than their precursors.[10] Ringuet et al. investigated the reactivity of different NPAH species and found the O_3 reaction to be negligible for 2-NFLT (Ringuet et al., 2012).[11] The same reaction was never reported for 2-NPYR. Particle phase 1-nitropyrene was shown to be less reactive than PYR with O_3 or NO_2.[12,13]

S4. Comparing Simulated and Measured Concentrations

In order to minimize incommensurability issues, model simulated concentration values were compared with observed values in the following ways:

- Bilinear interpolation within the model grid cell is used to obtain simulated concentrations that better represents the location of each observational site.
- Comparison between model and observations is now solely presented at rural rather than urban sites. Rural sites are less affected by local sources, and make for more representable comparison.

Temporal incommensurability is addressed by:

- Comparing measured concentrations with simulated concentrations from the same months (even if not same year).
- Observation sites where data was available over multiple seasons, were split into separate data points in order to prevent seasonal information being lost by averaging over time.

Table S1. Physicochemical properties and degradation rate coefficients of 2-NFLT and 2-NPYR used.

Parameter	Units	2-NFLT	2-NPYR	Reference
Molar mass	g mol^{-1}	247.25	247.25	-
Molar volume at boiling point	cm^3 mol^{-1}	245.8	242.3	Le Bas method[14]
Total (biotic and abiotic) decay rate in soil	s^{-1}	2.08×10^{-8}	3.13×10^{-8}	Estimate. Value for parent compound adopted due lack of data.
Total (biotic and abiotic) decay rate in ocean	s^{-1}	4.20×10^{-8}	2.80×10^{-9}	Estimate. Value for parent compound adopted due lack of data.
Water solubility (at 298K)	mg L^{-1}	0.019	0.021	[15,16]
Vapor pressure	Pa	9.91×10^{-7}	4.40×10^{-6}	[16]
Enthalpy of dissolution. $\Delta_{sol}H$	J mol^{-1}	6.595×10^4	6.546×10^4	COSMO-RS[17]
Heat of vaporization	J mol^{-1}	7.64×10^4	7.64×10^4	[18]
Heat of sublimation	J mol^{-1}	1.25×10^5	1.25×10^5	[19]
Octanol-water partition coefficient, $\log_{10}(K_{OW})$	-	4.69	4.69	[16,20]

Octanol-air partitioning coefficient, $\log_{10}(K_{OA})$ [a]		A = 5.2236 B = 1222.62 [K]	A = 5.1659 B = 1220.86 [K]	COSMO-RS[17]
Henry's constant. H(T) [b]		$H^{\ominus}$ = 8545 [M atm^{-1}] $-\Delta_{sol}H/R$ = 7932 [K]	$H^{\ominus}$ = 9354 [M atm^{-1}] $-\Delta_{sol}H/R$ = 7874 [K]	COSMO-RS[17]
ppLFER solute descriptors		E = 2.81 S = 2.07 A = 0 B = 0.33 V = 10.46 L = 1.76	E = 2.81 S = 2.07 A = 0 B = 0.33 V = 10.46 L = 1.76	Adopted from 1-nitropyrene[9]
Enthalpy of adsorption on black carbon	J mol^{-1}	1.25×10^5	1.25×10^5	Estimated for 1-nitropyrene using a predictive model and the estimated $K_{soot/air}$.[9,21]

[a] Temperature dependence of K_{OA} is in the form $K_{OA}(T) = A + B/T$

[b] $H(T) = H^{\ominus} \times \exp((- \Delta_{sol}H / R) \times (1 / T - 1 / T^{\ominus}))$ where $H^{\ominus}$ is Henry's constant at the reference temperature $T^{\ominus}$ = 298.15 K, $\Delta_{sol}H$ is the enthalpy of dissolution, R is the gas constant and T is temperature.[22]

Table S2. Full collection of NPAH observations used for comparison with the model.

Location	Time Start	Time End	Keywords	Classification	Reference
Marseilles_France_A	Jul-2004	Jul-2004	'Urban'	Urban	[23]
Marseilles_France_B	Jul-2004	Jul-2004	'Suburban'	Urban	[23]
Marseilles_France_C	Jul-2004	Jul-2004	'Rural'	Rural	[23]
Los_Angeles_US	Aug-2002	Aug-2002	'Source', 'Urban'	Urban	[24]
Los_Angeles_US	Jan-2003	Jan-2003	'Source', 'Urban'	Urban	[24]
Riverside_US	Aug-2002	Aug-2002	'Downwind receptor'	Urban	[24]
Riverside_US	Jan-2003	Jan-2003	'Downwind receptor'	Urban	[24]
São_Paulo_Brazil	Aug-2002	Aug-2002	'City'	Urban	[25]
São_Paulo_Brazil	Jul-2003	Jul-2003	'City'	Urban	[25]
Araraquara_Brazil	Aug-2002	Aug-2002	'Urban'	Urban	[25]
Araraquara_Brazil	Jul-2003	Jul-2003	'Urban'	Urban	[25]
Piracicaba_Brazil	Jul-2003	Jul-2003	'Sugarcane burning pollution'	Urban	[25]
Paulínia_Brazil	Aug-2002	Aug-2002	'Industries', 'Sugarcane crop emissions'	Urban	[25]
Araraquara_Brazil	Jun-2010	Jun-2010	'Rural', 'Sugar cane burning', 'Vehicular emissions'	Urban	[26]
Rayes_Saudia_Arabia	Sep-2013	Sep-2013	'Petrochemical works'	Urban	[27]
Rabegh_Saudia_Arabia	Sep-2013	Sep-2013	'Residential area', 'Local industry'	Urban	[27]
Abhur_Saudia_Arabia	Sep-2013	Sep-2013	'Suburb'	Urban	[27]
Baltimore_US	Jan-2001	Jan-2001	'Urban'	Urban	[28]
Baltimore_US	Jul-2001	Jul-2001	'Urban'	Urban	[28]
Fort_Meade_US	Jan-2001	Jan-2001	'Suburban'	Urban	[28]
Fort_Meade_US	Jul-2001	Jul-2001	'Suburban'	Urban	[28]
Finokalia_Crete	Jul-2012	Jul-2012	'Marine background'	Rural	[29]
Puszta_Hungary	Aug-2013	Aug-2013	'Continental background'	Rural	[29]
Chamonix_Valley_1_France	Jan-2003	Jan-2003	'Suburban'	Urban	[30]
Chamonix_Valley_2_France	Jan-2003	Jan-2003	'Traffic'	Urban	[30]
Chamonix_Valley_3_France	Jan-2003	Jan-2003	'Altitude'	Rural	[30]

Chamonix_Valley_4_France	Jan-2003	Jan-2003	'Rural'	Rural	30
Chamonix_Valley_1_France	Jul-2003	Jul-2003	'Suburban'	Urban	30
Chamonix_Valley_2_France	Jul-2003	Jul-2003	'Traffic'	Urban	30
Chamonix_Valley_3_France	Jul-2003	Jul-2003	'Altitude'	Rural	30
Chamonix_Valley_4_France	Jul-2003	Jul-2003	'Rural'	Rural	30
Maurienne_Valley_1_France	Jan-2003	Jan-2003	'Rural'	Rural	30
Maurienne_Valley_3_France	Jan-2003	Jan-2003	'Suburban'	Urban	30
Maurienne_Valley_4_France	Jan-2003	Jan-2003	'Rural'	Rural	30
Maurienne_Valley_1_France	Jun-2003	Jul-2003	'Rural'	Rural	30
Maurienne_Valley_2_France	Jun-2003	Jul-2003	'Suburban'	Urban	30
Maurienne_Valley_3_France	Jun-2003	Jul-2003	'Suburban'	Urban	30
Maurienne_Valley_4_France	Jun-2003	Jul-2003	'Rural'	Rural	30
Wanqingsha_China	Nov-2010	Nov-2010	'Rural', 'Coal-fired electric power plant'	Urban	31
Rouiba_Algeria	Jul-2006	Jul-2006	'Urban', 'Industrial'	Urban	32
Ouled_Moussa_Algeria	Jul-2006	Jul-2006	'Moderate or scarce vehicle traffic'	Urban	32
Bouzareah_Algeria	Jul-2006	Jul-2006	'Urban'	Urban	32
Chrea_Algeria	Jul-2006	Jul-2006	'Park', 'Forest'	Rural	32
Grenoble, France	Jan-2013	Jan-2014	'Urban'	Urban	8
Agra, India_1	Oct-2015	Feb-2016	'Rural'	Rural	33
Agra, India_2	Oct-2015	Feb-2016	'Traffic-dominated'	Urban	33
China_Wuwei_1	Apr-2010	Mar-2011	'Urban'	Urban	34
China_Yinchuan_1	Apr-2010	Mar-2011	'Urban'	Urban	34
China_Taiyuan_1	Apr-2010	Mar-2011	'Urban'	Urban	34
China_Beijing	Apr-2010	Mar-2011	'Urban'	Urban	34
China_Dezhou_1	Apr-2010	Mar-2011	'Urban'	Urban	34
China_Yantai_1	Apr-2010	Mar-2011	'Urban'	Urban	34
China_Dalian_1	Apr-2010	Mar-2011	'Urban'	Urban	34
China_Rural_Wuwei_2	Apr-2010	Mar-2011	'Rural field'	Rural	34
China_Rural_Yinchuan_2	Apr-2010	Mar-2011	'Rural field'	Rural	34

China_Rural_Taiyuan_2	Apr-2010	Mar-2011	'Rural field'	Rural	[34]
China_Rural _Dezhou_2	Apr-2010	Mar-2011	'Rural field'	Rural	[34]
China_Rural _Yantai _2	Apr-2010	Mar-2011	'Rural field'	Rural	[34]
China_Rural _Wuwei_3	Apr-2010	Mar-2011	'Rural village'	Rural	[34]
China_Rural field_Yinchuan_3	Apr-2010	Mar-2011	'Rural village'	Rural	[34]
China_Rural field_Taiyuan_3	Apr-2010	Mar-2011	'Rural village'	Rural	[34]
China_Rural field_Dezhou_3	Apr-2010	Mar-2011	'Rural village'	Rural	[34]
China_Rural field_Yantai_3	Apr-2010	Mar-2011	'Rural village'	Rural	[34]
China_Rural field_Dalian_2	Apr-2010	Mar-2011	'Rural field'	Rural	[34]
Nepal_Kathmandu	Aug-2014	Oct-2014	'City'	Urban	[35,36]
Nepal_Pokhara	Aug-2014	Oct-2014	'City'	Urban	[35,36]
Nepal_Birgunj	Aug-2014	Oct-2014	'City'	Urban	[35,36]
Nepal_Biratnajor	Aug-2014	Oct-2014	'City'	Urban	[35,36]
Lampang_Thailand	Mar-2013	Mar-2013	'Urban'	Urban	[37]
ChiangMai_Thailand_DrySeason	Feb-2010	Apr-2010	'City'	Urban	[38]
ChiangMai_Thailand_TransitionSeason	May-2010	May-2010	'City'	Urban	[38]
ChiangMai_Thailand_WetSeason	Aug-2010	Sep-2010	'City'	Urban	[38]
HoChiMinh_VNU_Vietnam	Jan-2005	Mar-2006	'Urban area'	Urban	[39]
HoChiMinh_ITTE_Vietnam	Jan-2005	Feb-2006	'Urban area'	Urban	[39]
HoChiMinh_DOSTE_Vietnam	Jan-2005	Feb-2006	'Urban area'	Urban	[39]
Elms_EROS_Birmingham	Sep-2012	Sep-2012	'Urban background'	Urban	[40]
Coyhaique_Chile	Mar-2007	Apr-2007	'Remote'	Rural	[41]
Concepcion_Chile	Mar-2007	Apr-2007	'Urban'	Urban	[41]
Xujiahui_Shanghai_China_Spring	Dec-2007	Jan-2008	'Urban', 'Busy highway'	Urban	[42]
Xujiahui_Shanghai_China_Summer	Dec-2007	Jan-2008	'Urban', 'Busy highway'	Urban	[42]
Xujiahui_Shanghai_China_Autumn	Dec-2007	Jan-2008	'Urban', 'Busy highway'	Urban	[42]
Xujiahui_Shanghai_China_Winter	Dec-2007	Jan-2008	'Urban', 'Busy highway'	Urban	[42]
Baoshan_Shanghai_China_Spring	Dec-2007	Jan-2008	'Busy highway', 'Residential', 'Industrial'	Urban	[42]
Baoshan_Shanghai_China_Summer	Dec-2007	Jan-2008	'Busy highway', 'Residential', 'Industrial'	Urban	[42]

Baoshan_Shanghai_China_Autumn	Dec-2007	Jan-2008	'Busy highway', 'Residential', 'Industrial'	Urban	42
Baoshan_Shanghai_China_Winter	Dec-2007	Jan-2008	'Busy highway', 'Residential', 'Industrial'	Urban	42
Linan_China_Spring	Dec-2007	Jan-2008	'Regional background'	Rural	42
Linan_China_Summer	Dec-2007	Jan-2008	'Regional background'	Rural	42
Linan_China_Autumn	Dec-2007	Jan-2008	'Regional background'	Rural	42
Linan_China_Winter	Dec-2007	Jan-2008	'Regional background'	Rural	42
HongKong_WholeYearAverage	Sep-2011	Aug-2012	'Urban'	Urban	43
Beijing_China	Mar-2012	Mar-2013	'Urban'	Urban	44
Jinan_China_(Urban)	Jun-2015	Jul-2015	'Urban'	Urban	45
MountTai_China	Jul-2015	Jul-2015	'Background', 'Mountain summit'	Rural	45
TuojiIsland_China	Jun-2015	Jun-2015	'Background', 'Marine'	Rural	45
CordobaCity_Argentina_Fall	Mar-2008	Apr-2008	'City'	Urban	46
CordobaCity_Argentina_Winter	Jun-2008	Jul-2008	'City'	Urban	46
CordobaCity_Argentina_Summer	Nov-2008	Dec-2008	'City'	Urban	46
SaoPaulo_Brazil	Jan-2014	Sep-2014	'Expressway', 'Campus'	Urban	47
SaoPaulo_Brazil	Jan-2014	Dec-2014	'Expressway', 'Campus'	Urban	47
TlalneplantaNW_MexicoValley_Mexico	Jan-2006	Dec-2006	'Metropolitan zone', 'Residential', 'Commercial', 'Factories', 'Vehicular avenues'	Urban	48
SanAgustinNE_MexicoValley_Mexico	Jan-2006	Dec-2006	'Metropolitan zone', 'Residential', 'Vehicular avenues'	Urban	48
MercedCentral_MexicoValley_Mexico	Jan-2006	Dec-2006	'Metropolitan zone', 'Residential', 'Commercial', 'Vehicular avenues'	Urban	48
CoyoacanSW_MexicoValley_Mexico	Jan-2006	Dec-2006	'Metropolitan zone', 'Residential', 'Vehicular avenues'	Urban	48
UniversidadAutonomous_MexicoValley_Mexico	Jan-2006	Dec-2006	'Metropolitan zone', 'Residential', 'Commercial', 'Vehicular avenues'	Urban	48
NorthMexicoCity_Mexico	Apr-2006	Feb-2007	'City'	Urban	49
Palaiseau_Paris_France	Jun-2009	Jul-2009	'Suburban'	Urban	50
PorteDAuteuil_Paris_France	Jun-2010	Aug-2010	'Traffic'	Urban	50

Rao_EMEPstation_Sweden	Dec-2008	Feb-2009	'Background'	Rural	[51]
Rao_EMEPstation_Sweden	Mar-2009	Mar-2009	'Background'	Rural	[51]
Rao_EMEPstation_Sweden	Apr-2009	Apr-2009	'Background'	Rural	[51]
Pallas_AMAPstation_Finland	Feb-2009	Mar-2009	'Background'	Rural	[51]
Pallas_AMAPstation_Finland	Mar-2009	Mar-2009	'Background'	Rural	[51]
Pallas_AMAPstation_Finland	Mar-2009	Apr-2009	'Background'	Rural	[51]
GoteborgFolketsHus_Sweden	Dec-2008	Dec-2008	'Urban', 'City/traffic'	Urban	[51]
GoteborgFolketsHus_Sweden	Feb-2009	Mar-2009	'Urban', 'City/traffic'	Urban	[51]
GoteborgGarda_Sweden	Jan-2009	Feb-2009	'Urban', 'City/traffic'	Urban	[51]
GoteborgGarda_Sweden	Jan-2009	Feb-2009	'Urban', 'City/traffic'	Urban	[51]
Lycksele_North_Sweden	Feb-2009	Feb-2009	'Urban', 'Wood combustion', 'Traffic'	Urban	[51]
Lycksele_North_Sweden	Mar-2009	Mar-2009	'Urban', 'Wood combustion', 'Traffic'	Urban	[51]
Lycksele_North_Sweden	Apr-2009	Apr-2009	'Urban', 'Wood combustion', 'Traffic'	Urban	[51]
KanazawaCity_Japan_Autumn	Nov-2016	Nov-2016	'City'	Urban	[52]
KanazawaCity_Japan_Spring	Mar-2017	Mar-2017	'City'	Urban	[52]
KanazawaCity_Japan_Summer	Aug-2016	Aug-2016	'City'	Urban	[52]
KanazawaCity_Japan_Winter	Jan-2017	Jan-2017	'City'	Urban	[52]
Wajima_Japan_Autumn	Nov-2016	Nov-2016	'Rural background'	Rural	[52]
Wajima_Japan_Spring	Mar-2017	Mar-2017	'Rural background'	Rural	[52]
Wajima_Japan_Summer	Jan-2017	Jan-2017	'Rural background'	Rural	[52]
Wajima_Japan_Winter	Jul-2016	Jul-2016	'Rural background'	Rural	[52]
Kigali_Rwanda_Dry season	Jun-2017	Jun-2017	'Urban background'	Urban	[53]
Kigali_Rwanda_Wet season	Apr-2017	Apr-2017	'Urban background'	Urban	[53]
Kigali_Rwanda_Dry season	Jun-2017	Jun-2017	'Urban roadside'	Urban	[53]
Kigali_Rwanda_Wet season	May-2017	May-2017	'Urban roadside'	Urban	[53]
Rwanda_Wet season	Apr-2017	May-2017	'Rural'	Rural	[53]
AucklandCity_New Zealand_Autumn	Apr-2016	Apr-2016	'City'	Urban	[52]
AucklandCity_New Zealand_Spring	Oct-2016	Oct-2016	'City'	Urban	[52]

Auckland_City_New Zealand Summer	Mar-2017	Mar-2017	'City'	Urban	[52]
Auckland_City_New Zealand_Winter	Jul-2016	Jul-2016	'City'	Urban	[52]
Tapora_New Zealand_Autumn	Apr-2016	Apr-2016	'Rural background'	Rural	[52]
Tapora_New Zealand_Spring	Oct-2016	Oct-2016	'Rural background'	Rural	[52]
Tapora_New Zealand_Summer	Feb-2017	Feb-2017	'Rural background'	Rural	[52]
Tapora_New Zealand_Winter	Jul-2016	Jul-2016	'Rural background'	Rural	[52]

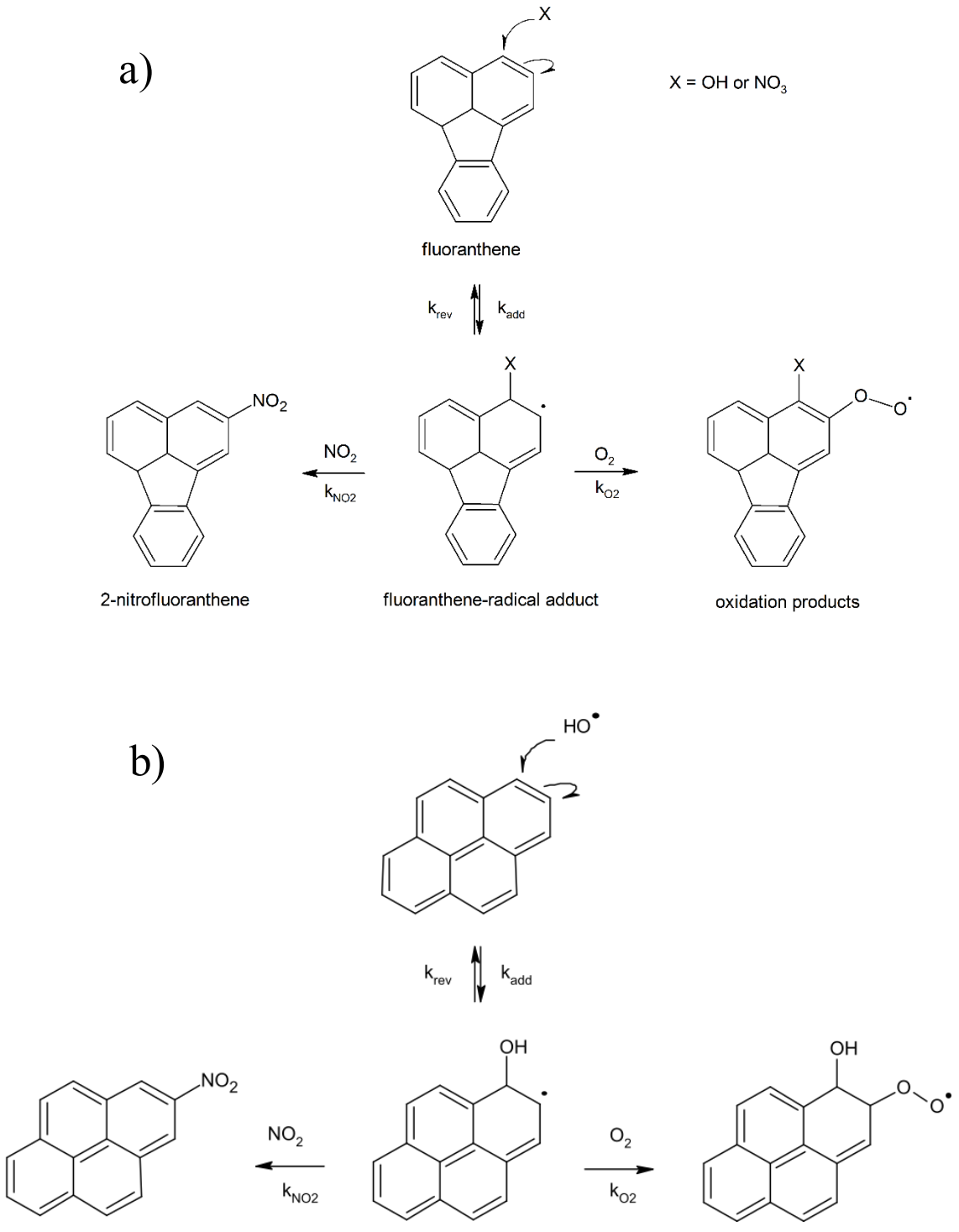

Figure S1. a) Mechanism of 2-nitrofluoranthene formation by the addition of a radical (X = OH or NO_3). Following initial radical addition (k_{add}), three processes compete for the fluoranthene-radical adduct: unimolecular decomposition (k_{rev}), reaction with O_2 to form oxygenated products (k_{O2}) or reaction with NO_2 to form 2-nitrofluoranthene. b) The same scheme is applicable for 2-nitropyrene with addition of an OH radical.

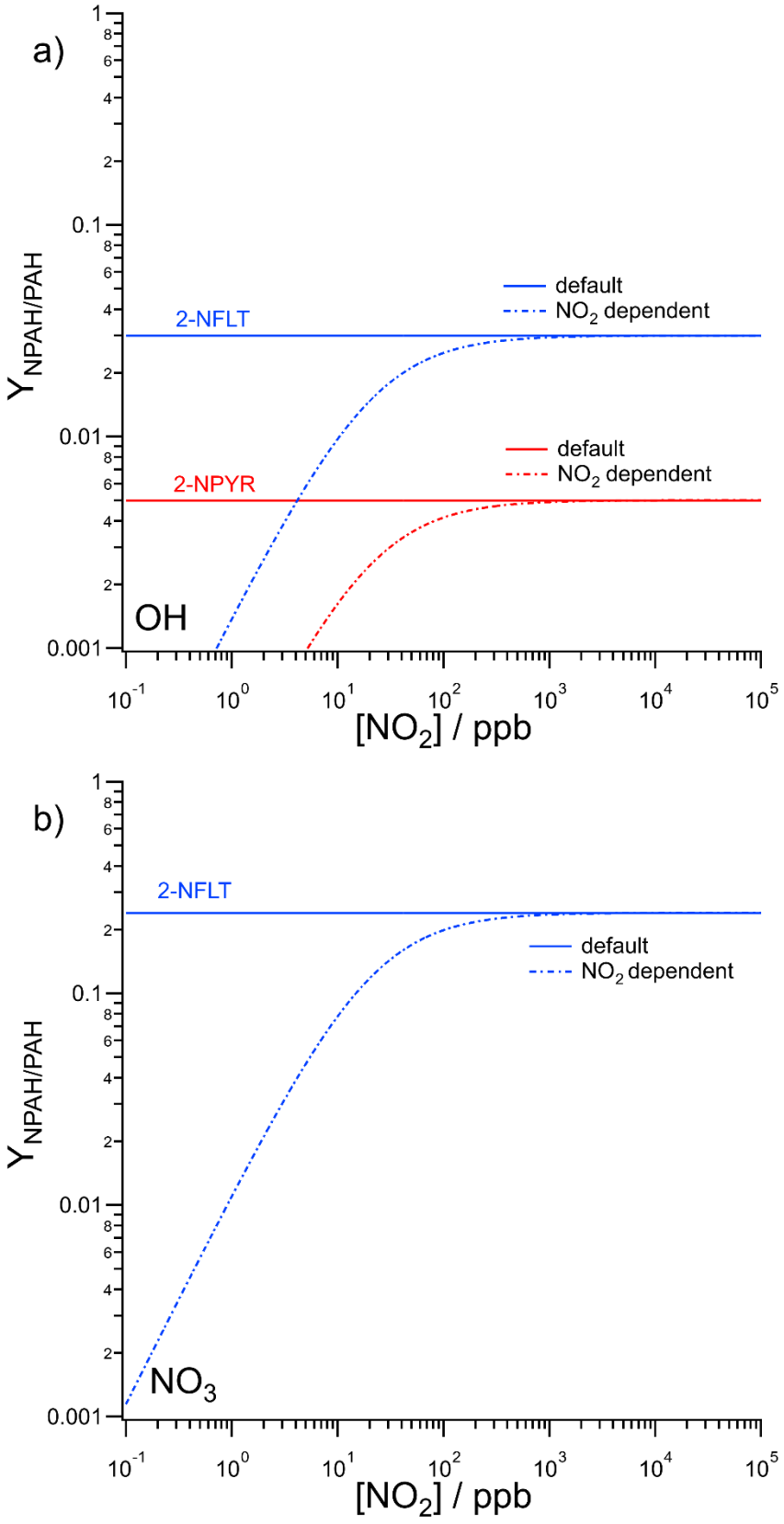

Figure S2. Dependence of yield on NO_2 mixing ratio in the NO_2-dependent reactivity schemes for the reaction of FLT or PYR with a) OH or b) NO_3.

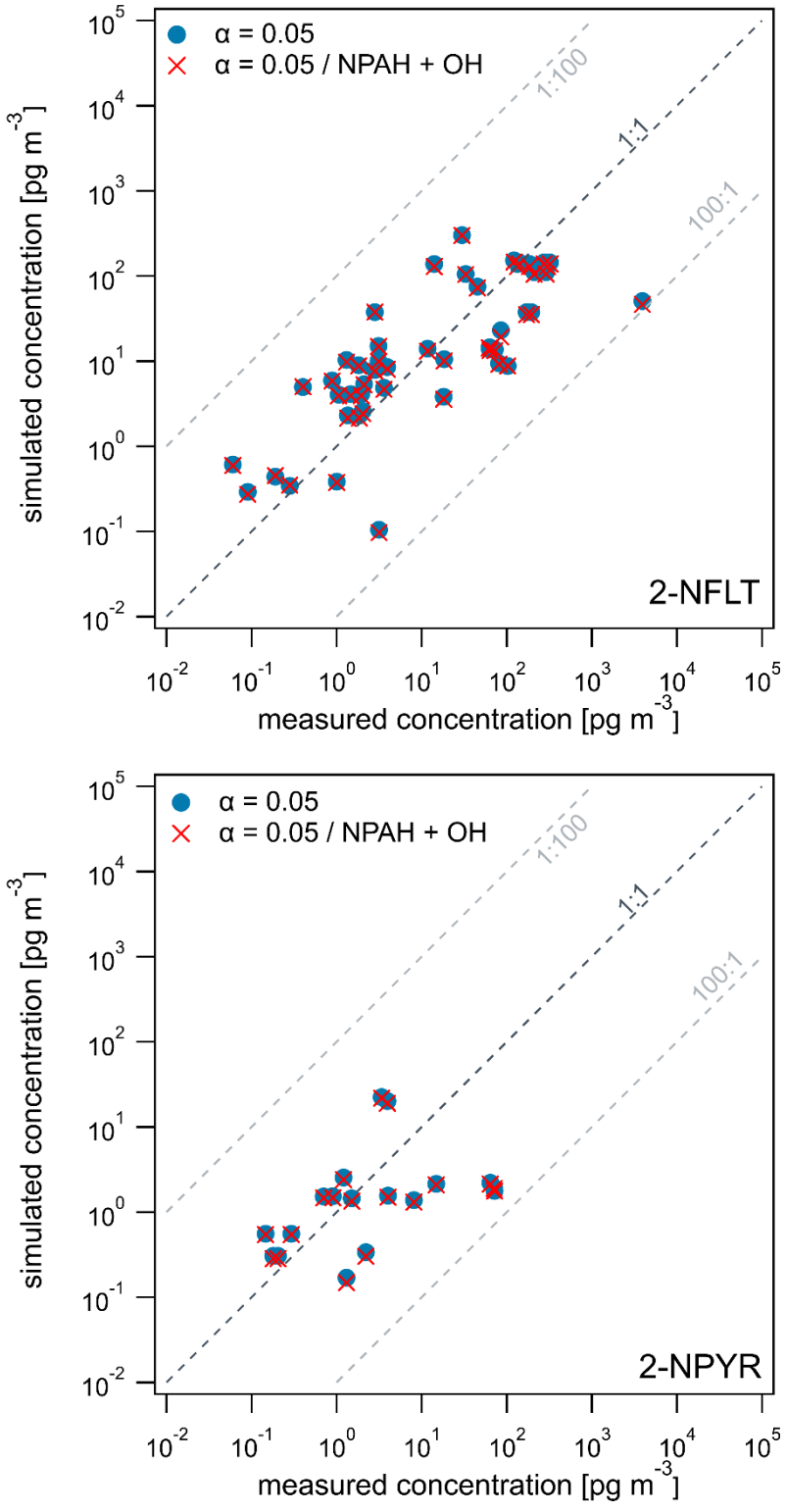

Figure S3. Comparison between simulated and measured near-surface concentrations [pg m^{-3}] of 2-NFLT (above) and 2-NPYR (below) using the default reactivity scenario and sensitivity test with homogeneous reaction of NPAH with the OH radical.

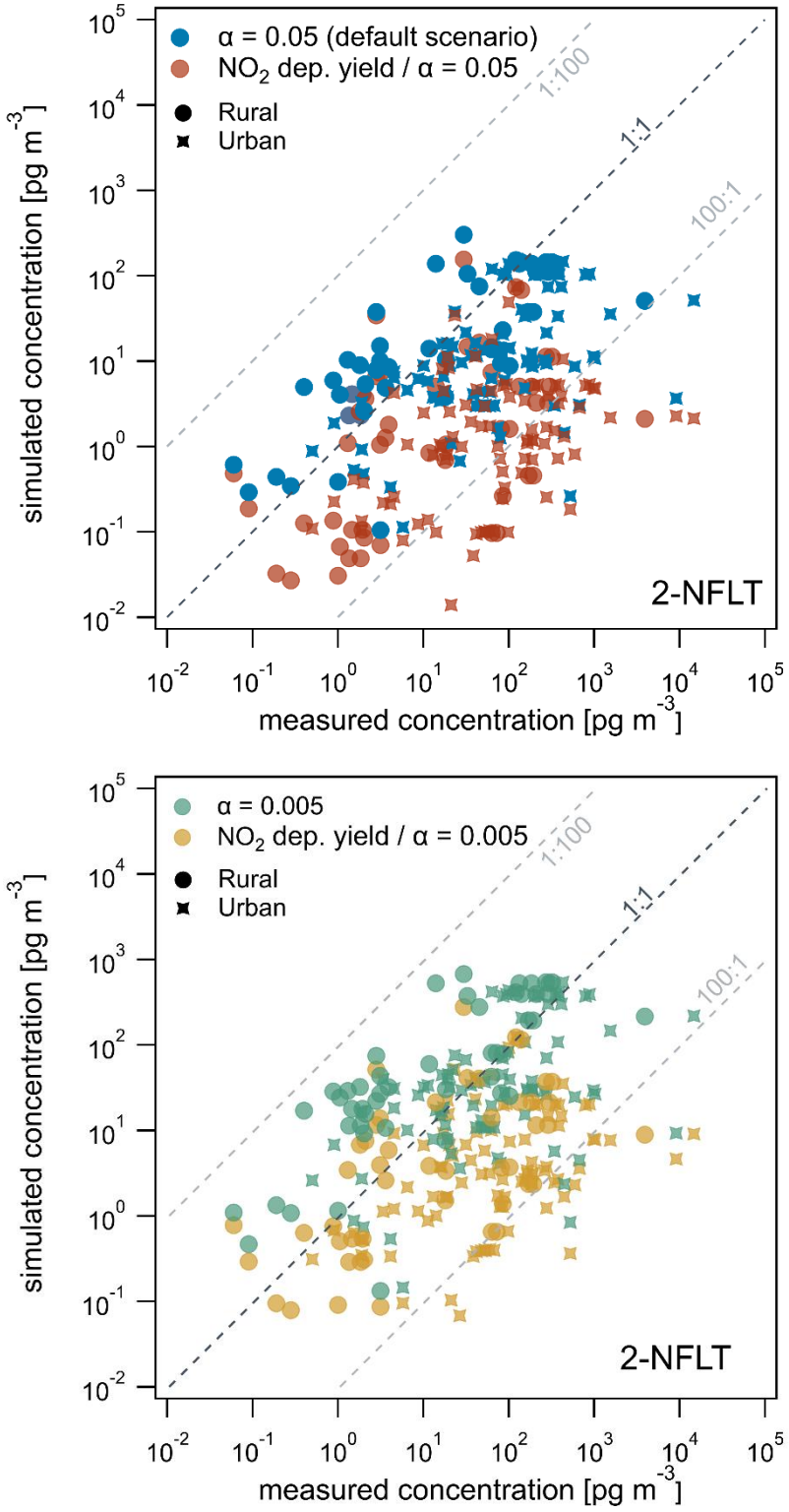

Figure S4. Comparison between simulated and measured near-surface concentrations [pg m^{-3}] at rural and urban sites of 2-NFLT comparing alternative scenarios with α = 0.05 (above) and α = 0.005 (below).

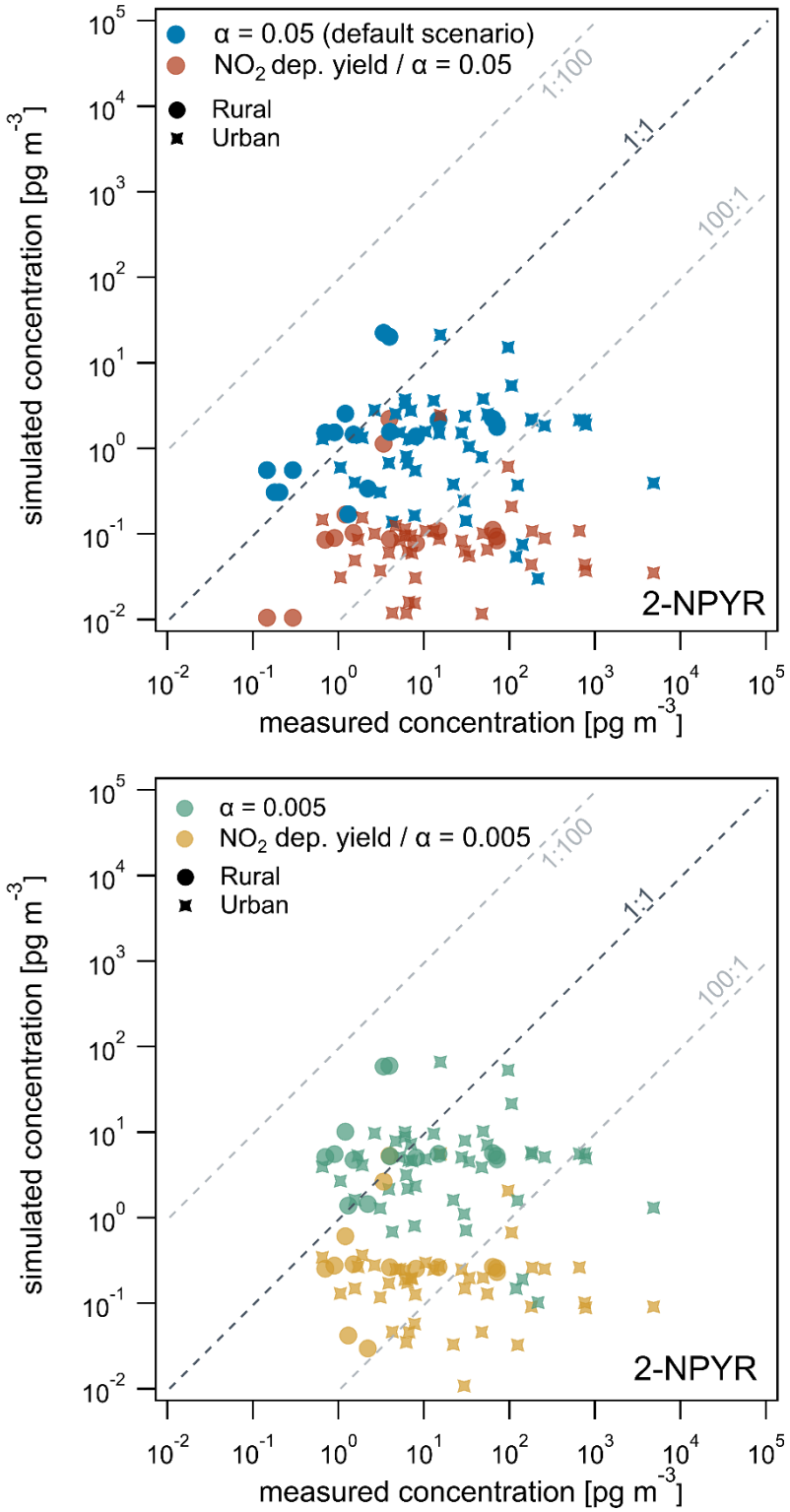

Figure S5. Comparison between simulated and measured near-surface concentrations [pg m^{-3}] at rural and urban sites of 2-NPYR comparing alternative scenarios with α = 0.05 (above) and α = 0.005 (below).

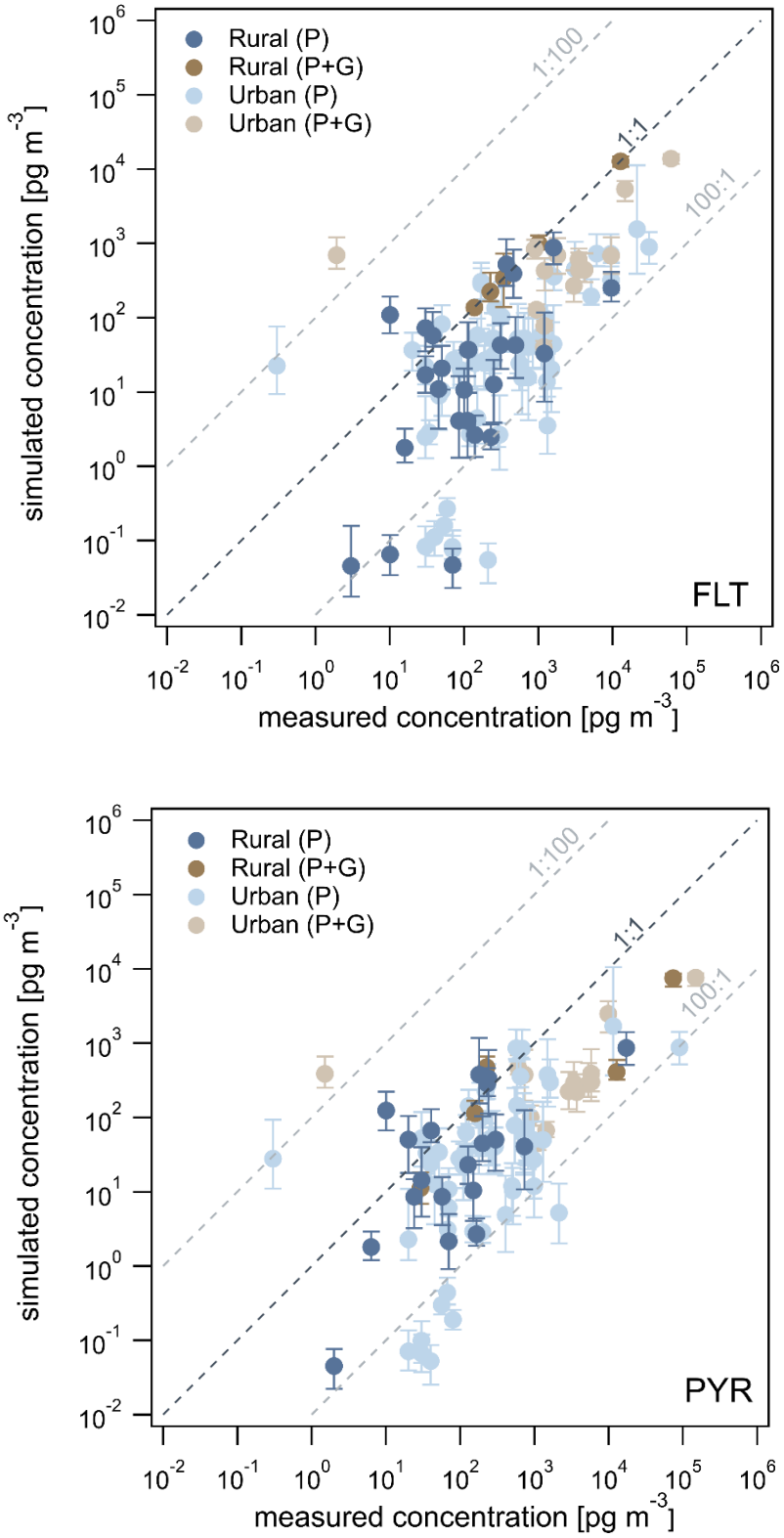

Figure S6. Comparison between simulated and measured concentrations [pg m^{-3}] of FLT (above) and PYR (below). Observations at rural sites (including remote) are distinguished from urban sites. Error bars represent the upper and lower quartile for simulated results across the entire time period. P = particle phase concentration, P+G = total concentration.

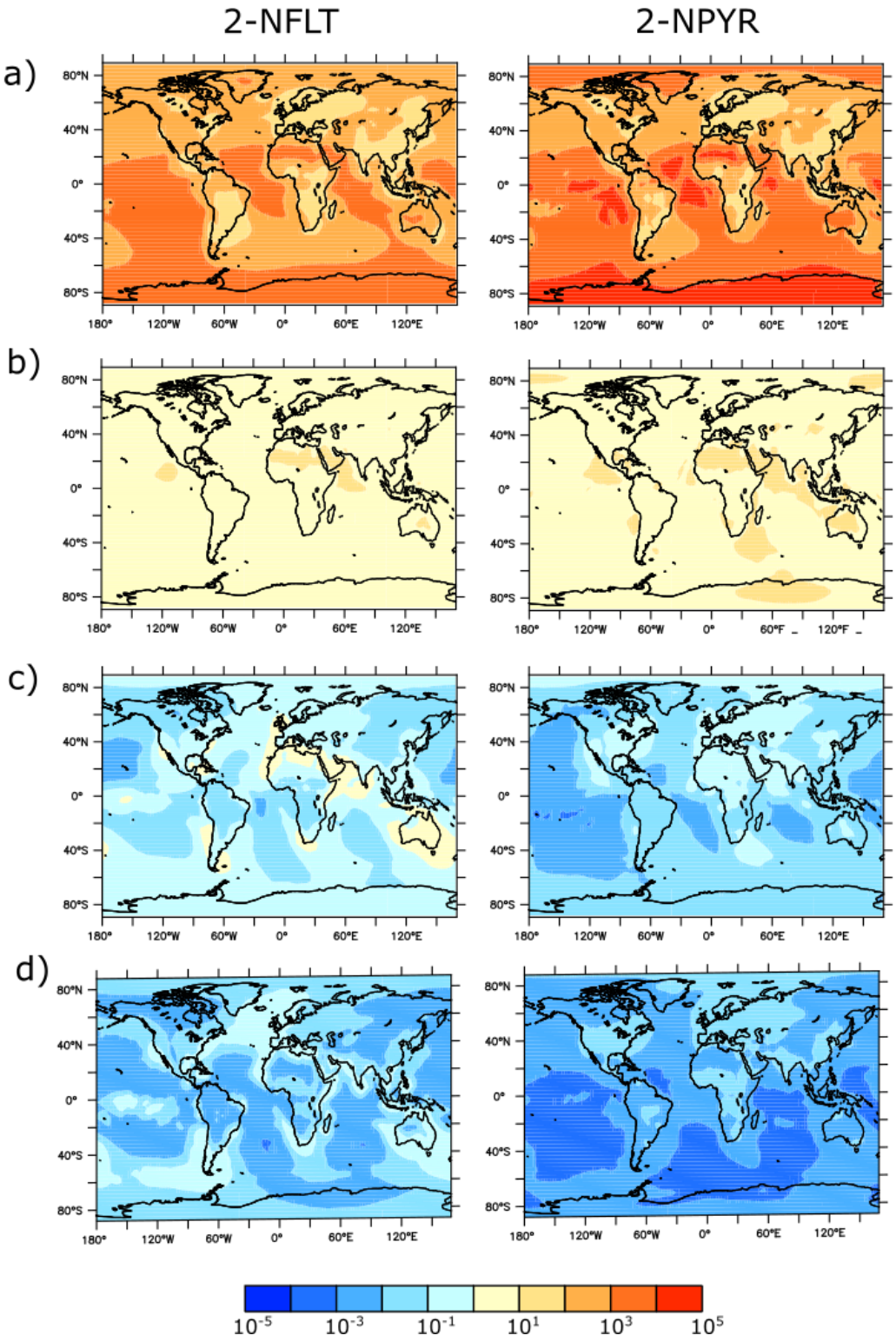

Figure S7. Column densities of 2-NFLT (left) and 2-NPYR (right) of sensitivity study averaged over 2006 – 2008 relative to the default scenario averaged over 2006 - 2008, $NPAH_{sensitivity}/NPAH_{default}$. For the scenarios with a) no photodegradation, b) with reduced photodegradation ($\alpha = 0.005$), c) with NO_2-dependent formation ($\alpha = 0.005$) and d) with NO_2-dependent formation (0.05), averaged over 2006 - 2008.

References

(1) Atkinson, R.; Arey, J.; Zielinska, B.; Aschmann, S. M. Kinetics and nitro-products of the gas-phase OH and NO_3 radical-initiated reactions of naphthalene-d8, fluoranthene-d10, and pyrene. *Int. J. Chem. Kinet.* **1990**, *22*, 999–1014. https://doi.org/10.1002/kin.550220910.

(2) Zhang, Q.; Gao, R.; Xu, F.; Zhou, Q.; Jiang, G.; Wang, T.; Chen, J.; Hu, J.; Jiang, W.; Wang, W. Role of water molecule in the gas-phase formation process of nitrated polycyclic aromatic hydrocarbons in the atmosphere: A computational study. *Environ. Sci. Technol.* **2014**, *48*, 5051–5057. https://doi.org/10.1021/es500453g.

(3) Brubaker, W. W.; Hites, R. OH reaction kinetics of polycyclic aromatic hydrocarbons and polychlorinated dibenzo-p-dioxins and dibenzofurans. *J. Phys. Chem. A* **1998**, *102*, 915–921. https://doi.org/10.1021/jp9721199.

(4) Ghigo, G.; Causà, M.; Maranzana, A.; Tonachini, G. Aromatic hydrocarbon nitration under tropospheric and combustion conditions. A theoretical mechanistic study. *J. Phys. Chem. A* **2006**, *110*, 13270–13282. https://doi.org/10.1021/jp064459c.

(5) Knispel, R.; Koch, R.; Siese, M.; Zetzsch, C. Adduct formation of OH radicals with benzene, toluene, and phenol and consecutive reactions of the adducts with NO_x and O_2. *Ber. Bunsenges. Physik. Chem.* **1990**, *94*, 1375–1379.

(6) Feilberg, A.; Kamens, R. M.; Strommen, M. R.; Nielsen, T. Modeling the formation, decay, and partitioning of semivolatile nitro-polycyclic aromatic hydrocarbons (nitronaphthalenes) in the atmosphere. *Atmos. Environ.* **1999**, *33*, 1231–1243. https://doi.org/10.1016/S1352-2310(98)00275-1.

(7) Koch, R.; Knispel, R.; Elend, M.; Siese, M.; Zetzsch, C. Consecutive reactions of aromatic–OH adducts with NO, NO_2 and O_2: Benzene, toluene, m- and p-cylene, hexamethylbenzene, phenol, m-cresol and aniline. *Atmos. Chem. Phys.* **2007**, *6*, 2057–2071. https://doi.org/10.5194/acpd-6-7623-2006.

(8) Tomaz, S.; Shahpoury, P.; Jaffrezo, J.-L.; Lammel, G.; Perraudin, E.; Villenave, E.; Albinet, A. One-year study of polycyclic aromatic compounds at an urban Site in Grenoble (France): Seasonal variations, gas/particle partitioning and cancer risk estimation. *Sci. Total Environ.* **2016**, *565*, 1071–1083. https://doi.org/10.1016/j.scitotenv.2016.05.137.

(9) Ariyasena, T. C.; Poole, C. F. Determination of descriptors for polycyclic aromatic hydrocarbons and related compounds by chromatographic methods and liquid-liquid partition in totally organic biphasic systems. *J. Chromatogr. A* **2014**, *1361*, 240–254. https://doi.org/10.1016/j.chroma.2014.08.008.

(10) Atkinson, R.; Arey, J. Atmospheric chemistry of gas-phase polycyclic aromatic hydrocarbons: Formation of atmospheric mutagens. *Environ. Health Perspect.* **1994**, *102* (Suppl 4), 117–126.

(11) Ringuet, J.; Albinet, A.; Leoz-Garziandia, E.; Budzinski, H.; Villenave, E. Reactivity of polycyclic aromatic compounds (PAHs, NPAHs and OPAHs) adsorbed on natural aerosol particles exposed to atmospheric oxidants. *Atmos. Environ.* **2012**, *61*, 15–22. https://doi.org/10.1016/j.atmosenv.2012.07.025.

(12) Miet, K.; Le Menach, K.; Flaud, P.-M.; Budzinski, H.; Villenave, E. Heterogeneous reactivity of pyrene and 1-nitropyrene with NO_2: Kinetics, product yields and mechanism. *Atmos. Environ.* **2009**, *43*, 837–843. https://doi.org/10.1016/j.atmosenv.2008.10.041.

(13) Miet, K.; Le Menach, K.; Flaud, P. M.; Budzinski, H.; Villenave, E. Heterogeneous reactions of ozone with pyrene, 1-hydroxypyrene and 1-nitropyrene adsorbed on particles. *Atmos. Environ.* **2009**, *43*, 3699–3707. https://doi.org/10.1016/j.atmosenv.2009.04.032.

(14) Poling, B. E.; Prausnitz, J. M.; O'Connell, J. P. *The Properties of Gases and Liquids*; McGraw-Hill, 2001.

(15) Yu, G.; Xu, X. Investigation of aqueous solubilities of nitro-PAH by dynamic couple-column HPLC. *Chemosphere* **1992**, *24*, 1699–1705. https://doi.org/10.1016/0045-6535(92)90224-F.

(16) Yaffe, D.; Cohen, Y.; Arey, J.; Grosovsky, A. J. Multimedia analysis of PAHs and nitro-PAH daughter products in the Los Angeles Basin. *Risk Anal* **2001**, *21*, 275–94. https://doi.org/10.1111/0272-4332.212111.

(17) Parnis, J. M.; Mackay, D.; Harner, T. Temperature dependence of Henry's Law constants and K_{OA} for simple and heteroatom-substituted PAHs by COSMO-RS. *Atmos. Environ.* **2015**, *110*, 27–35. https://doi.org/10.1016/j.atmosenv.2015.03.032.

(18) Joback, K. G.; Reid, R. C. Estimation of pure-component properties from group-contributions. *Chem. Eng. Commun.* **1987**, *57*, 233–243. https://doi.org/10.1080/00986448708960487.

(19) Goldfarb, J. L.; Suuberg, E. M. Vapor pressures and thermodynamics of oxygen-containing polycyclic aromatic hydrocarbons measured using knudsen effusion. *Environ. Toxicol. Chem.* **2008**, *27*, 1244–9. https://doi.org/10.1897/07-486.1

(20) Hansch, C.; Leo, A. *Substituent constants for correlation analysis in chemistry and biology*; Wiley, 1979.

(21) Arp, H. P. H.; Goss, K.-U.; Schwarzenbach, R. P. Evaluation of a predictive model for air/surface adsorption equilibrium constants and enthalpies. *Environ. Toxicol. Chem.* **2006**, *25*, 45–51. https://doi.org/10.1897/05-291r.1.

(22) Sander, R. Compilation of Henry's Law constants (version 4.0) for water as solvent. *Atmos. Chem. Phys.* **2015**, *15*, 4399–4981. https://doi.org/10.5194/acp-15-4399-2015.

(23) Albinet, A.; Leoz-Garziandia, E.; Budzinski, H.; Villenave, E. Polycyclic aromatic hydrocarbons (PAHs), nitrated PAHs and oxygenated PAHs in ambient air of the Marseilles area (South of France): Concentrations and sources. *Sci. Total Environ.* **2007**, *384*, 280–292. https://doi.org/10.1016/j.scitotenv.2007.04.028.

(24) Reisen, F.; Arey, J. Atmospheric reactions influence seasonal PAH and nitro-PAH concentrations in the Los Angeles Basin. *Environ. Sci. Technol.* **2005**, *39*, 64–73. https://doi.org/10.1021/es035454l.

(25) De Castro Vasconcellos, P.; Sanchez-Ccoyllo, O.; Balducci, C.; Mabilia, R.; Cecinato, A. Occurrence and concentration levels of nitro-PAH in the air of three Brazilian cities experiencing different emission impacts. *Water Air Soil Pollut.* **2008**, *190*, 87–94. https://doi.org/10.1007/s11270-007-9582-y.

(26) Souza, K. F.; Carvalho, L. R. F.; Allen, A. G.; Cardoso, A. A. Diurnal and nocturnal measurements of PAH, nitro-PAH, and oxy-PAH compounds in atmospheric particulate matter of a sugar cane burning region. *Atmos. Environ.* **2014**, *83*, 193–201. https://doi.org/10.1016/j.atmosenv.2013.11.007.

(27) Harrison, R. M.; Alam, M. S.; Dang, J.; Ismail, I. M.; Basahi, J.; Alghamdi, M. A.; Hassan, I. A.; Khoder, M. Relationship of polycyclic aromatic hydrocarbons with oxy(quinone) and nitro derivatives during air mass transport. *Sci. Total Environ.* **2016**, *572*, 1175–1183. https://doi.org/10.1016/j.scitotenv.2016.08.030.

(28) Bamford, H. A.; Baker, J. E. Nitro-polycyclic aromatic hydrocarbon concentrations and sources in urban and suburban atmospheres of the Mid-Atlantic Region. *Atmos. Environ.* **2003**, *37*, 2077–2091. https://doi.org/10.1016/S1352-2310(03)00102-X.

(29) Lammel, G.; Mulder, M. D.; Shahpoury, P.; Kukuaka, P.; Lišková, H.; Přibylová, P.; Prokeš, R.; Wotawa, G. Nitro-polycyclic aromatic hydrocarbons - gas-particle partitioning, mass size distribution, and formation along transport in marine and continental background air. *Atmos. Chem. Phys.* **2017**, *17*, 6257–6270. https://doi.org/10.5194/acp-17-6257-2017.

(30) Albinet, A.; Leoz-Garziandia, E.; Budzinski, H.; Villenave, E.; Jaffrezo, J. L. Nitrated and oxygenated derivatives of polycyclic aromatic hydrocarbons in the ambient air of two French Alpine valleys. Part 1: Concentrations, sources and gas/particle Partitioning. *Atmos. Environ.* **2008**, *42*, 43–54. https://doi.org/10.1016/j.atmosenv.2007.10.009.

(31) Huang, B.; Liu, M.; Bi, X.; Chaemfa, C.; Ren, Z.; Wang, X.; Sheng, G.; Fu, J. Phase distribution, sources and risk assessment of PAHs, NPAHs and OPAHs in a rural Site of Pearl River Delta Region, China. *Atmos. Pollut. Res.* **2014**, *5*, 210–218. https://doi.org/10.5094/APR.2014.026.

(32) Moussaoui, Y.; Balducci, C.; Cecinato, A.; Meklati, B. Y. Atmospheric particulate organic matter at urban and forest sites of Northern Algeria. *Urban Clim.* **2013**, *4*, 85–101. https://doi.org/10.1016/j.uclim.2013.05.001.

(33) Kumar Verma, P.; Sah, D.; Maharaj Kumari, K.; Lakhani, A. Atmospheric concentrations and gas–particle partitioning of polycyclic aromatic hydrocarbons (PAHs) and nitro-PAHs at Indo-Gangetic sites. *Environ. Sci. Process Impacts* **2017**, *19*, 1051–1060. https://doi.org/10.1039/C7EM00168A.

(34) Li, W.; Wang, C.; Shen, H.; Su, S.; Shen, G.; Huang, Y.; Zhang, Y.; Chen, Y.; Chen, H.; Lin, N.; Zhuo, S.; Zhong, Q.; Wang, X.; Liu, J.; Li, B.; Liu, W.; Tao, S. Concentrations and origins of nitro-polycyclic aromatic hydrocarbons and oxy-polycyclic aromatic hydrocarbons in ambient air in urban and rural areas in Northern China. *Environ. Pollut.* **2015**, *197*, 156–164. https://doi.org/10.1016/j.envpol.2014.12.019.

(35) Yadav, I. C.; Devi, N. L.; Singh, V. K.; Li, J.; Zhang, G. Concentrations, sources and health risk of nitrated- and oxygenated-polycyclic aromatic hydrocarbon in urban indoor air and dust from four cities of Nepal. *Sci. Total Environ.* **2018**, *643*, 1013–1023. https://doi.org/10.1016/j.scitotenv.2018.06.265.

(36) Yadav, I. C.; Devi, N. L.; Li, J.; Zhang, G. Altitudinal and spatial variations of polycyclic aromatic hydrocarbons in Nepal: Implications on source apportionment and

risk assessment. *Chemosphere* **2018**, *198*, 386–396. https://doi.org/10.1016/j.chemosphere.2018.01.075.

(37) Orakij, W.; Chetiyanukornkul, T.; Chuesaard, T.; Kaganoi, Y.; Uozaki, W.; Homma, C.; Boongla, Y.; Tang, N.; Hayakawa, K.; Toriba, A. Personal inhalation exposure to polycyclic aromatic hydrocarbons and their nitro-derivatives in rural residents in Northern Thailand. *Environ. Monit. Assess.* **2017**, *189*, 510. https://doi.org/10.1007/s10661-017-6220-z.

(38) Chuesaard, T.; Chetiyanukornkul, T.; Kameda, T.; Hayakawa, K.; Toriba, A. Influence of biomass burning on the levels of atmospheric polycyclic aromatic hydrocarbons and their nitro derivatives in Chiang Mai, Thailand. *Aerosol Air Qual. Res.* **2014**, *14*, 1247–1257. https://doi.org/10.4209/aaqr.2013.05.0161.

(39) Hien, T. T.; Thanh, L. T.; Kameda, T.; Takenaka, N.; Bandow, H. Nitro-polycyclic aromatic hydrocarbons and polycyclic aromatic hydrocarbons in particulate matter in an urban area of a tropical region: Ho Chi Minh City, Vietnam. *Atmos. Environ.* **2007**, *41*, 7715–7725. https://doi.org/10.1016/j.atmosenv.2007.06.020.

(40) Keyte, I. J.; Albinet, A.; Harrison, R. M. On-road traffic emissions of polycyclic aromatic hydrocarbons and their oxy- and nitro- derivative compounds measured in road tunnel environments. *Sci. Total Environ.* **2016**, *566–567*, 1131–1142. https://doi.org/10.1016/j.scitotenv.2016.05.152.

(41) Scipioni, C.; Villanueva, F.; Pozo, K.; Mabilia, R. Preliminary characterization of polycyclic aromatic hydrocarbons, nitrated polycyclic aromatic hydrocarbons and polychlorinated dibenzo-p-dioxins and furans in atmospheric PM_{10} of an urban and a remote area of Chile. *Environ. Technol.* **2012**, *33*, 809–820. https://doi.org/10.1080/09593330.2011.597433.

(42) Wang, W.; Liu, D.; Wang, B.; Zhan, J.; Zhang, D.; Sun, Y.; Li, H.; Yang, Y.; Zhao, J.; Jing, L.; Feng, J. Spatial and temporal variations of nitro-polycyclic aromatic hydrocarbons in $PM_{2.5}$ aerosols in Yangtze River Delta Region, China. *World Rev. Sci. Technol. Sustain. Dev.* **2013**, *10*, 228–241. https://doi.org/10.1504/WRSTSD.2013.057694.

(43) Ma, Y.; Cheng, Y.; Qiu, X.; Lin, Y.; Cao, J.; Hu, D. A Quantitative assessment of source contributions to fine particulate matter ($PM_{2.5}$)-bound polycyclic aromatic hydrocarbons (PAHs) and their nitrated and hydroxylated derivatives in Hong Kong. *Environ. Pollut.* **2016**, *219*, 742–749. https://doi.org/10.1016/j.envpol.2016.07.034.

(44) Lin, Y.; Ma, Y.; Qiu, X.; Li, R.; Fang, Y.; Wang, J.; Zhu, Y.; Hu, D. Sources, transformation, and health implications of PAHs and their nitrated, hydroxylated, and oxygenated derivatives in $PM_{2.5}$ in Beijing. *J. Geophys. Res. Atmospheres* **2015**, *120*, 7219–7228. https://doi.org/10.1002/2015JD023628.

(45) Zhang, J.; Yang, L.; Mellouki, A.; Chen, J.; Chen, X.; Gao, Y.; Jiang, P.; Li, Y.; Yu, H.; Wang, W. Diurnal concentrations, sources, and cancer risk assessments of $PM_{2.5}$-bound PAHs, NPAHs, and OPAHs in urban, marine and mountain environments. *Chemosphere* **2018**, *209*, 147–155. https://doi.org/10.1016/j.chemosphere.2018.06.054.

(46) Carreras, H. A.; Calderón-Segura, M. E.; Gómez-Arroyo, S.; Murillo-Tovar, M. A.; Amador-Muñoz, O. Composition and mutagenicity of PAHs associated with urban

airborne particles in Córdoba, Argentina. *Environ. Pollut.* **2013**, *178*, 403–410. https://doi.org/10.1016/j.envpol.2013.03.016.

(47) Pereira, G. M.; Teinilä, K.; Custódio, D.; Gomes Santos, A.; Xian, H.; Hillamo, R.; Alves, C. A.; Bittencourt de Andrade, J.; Olímpio da Rocha, G.; Kumar, P.; Balasubramanian, R.; Andrade, M. de F.; Castro Vasconcellos, P. de. Particulate pollutants in the Brazilian city of São Paulo: 1-Year investigation for the chemical composition and source apportionment. *Atmos. Chem. Phys.* **2017**, *17*, 11943–11969. https://doi.org/https://doi.org/10.5194/acp-17-11943-2017.

(48) Amador-Muñoz, O.; Villalobos-Pietrini, R.; Miranda, J.; Vera-Avila, L. E. Organic compounds of $PM_{2.5}$ in Mexico Valley: Spatial and temporal patterns, behavior and sources. *Sci. Total Environ.* **2011**, *409*, 1453–1465. https://doi.org/10.1016/j.scitotenv.2010.11.026.

(49) Valle-Hernández, B. L.; Mugica-Álvarez, V.; Salinas-Talavera, E.; Amador-Muñoz, O.; Murillo-Tovar, M. A.; Villalobos-Pietrini, R.; De Vizcaya-Ruíz, A. Temporal variation of nitro-polycyclic aromatic hydrocarbons in PM_{10} and $PM_{2.5}$ collected in Northern Mexico City. *Sci. Total Environ.* **2010**, *408*, 5429–5438. https://doi.org/10.1016/j.scitotenv.2010.07.065.

(50) Ringuet, J.; Albinet, A.; Leoz-Garziandia, E.; Budzinski, H.; Villenave, E. Diurnal/nocturnal concentrations and sources of particulate-bound PAHs, OPAHs and NPAHs at traffic and suburban sites in the region of Paris (France). *Sci. Total Environ.* **2012**, *437*, 297–305. https://doi.org/10.1016/j.scitotenv.2012.07.072.

(51) Results from the Swedish national screening programme 2008. Subreport 4: Screening of unintentionally produced organic contaminants. https://www.nilu.no/en//apub/27184/.

(52) Kalisa, E.; Nagato, E.; Bizuru, E.; Lee, K.; Tang, N.; Pointing, S.; Hayakawa, K.; Archer, S.; Lacap-Bugler, D. Pollution characteristics and risk assessment of ambient $PM_{2.5}$-bound PAHs and NPAHs in typical Japanese and New Zealand cities and rural Sites. *Atmos. Pollut. Res.* **2019**, *10*, 1396–1403. https://doi.org/10.1016/j.apr.2019.03.009.

(53) Kalisa, E.; Nagato, E. G.; Bizuru, E.; Lee, K. C.; Tang, N.; Pointing, S. B.; Hayakawa, K.; Archer, S. D. J.; Lacap-Bugler, D. C. Characterization and risk assessment of atmospheric $PM_{2.5}$ and PM_{10} particulate-bound PAHs and NPAHs in Rwanda, Central-East Africa. *Environ. Sci. Technol.* **2018**, *52*, 12179–12187. https://doi.org/10.1021/acs.est.8b03219.

2.3. Visualizing Chemical Reactions as a Weighted Network

This chapter will eventually be submitted as a manuscript for peer review. I am the first author and my personal contribution included designing the *KinViz* tool, writing the code (using MATLAB), identifying intuitive modes of visualization, optimizing the graphical appearance of networks, selecting and processing an illustrative case study (the oscillating Belousov-Zhabotinsky reaction), preparing figures and writing the manuscript.

KinViz - Visualization of systems of chemical reactions as weighted networks

Jake Wilson, Thomas Berkemeier, Steven Lelieveld, and Ulrich Pöschl

Multiphase Chemistry Department, Max Planck Institute for Chemistry, Mainz, Germany

KinViz - VISUALIZATION OF SYSTEMS OF CHEMICAL REACTIONS AS WEIGHTED NETWORKS

A PREPRINT

Jake Wilson
Multiphase Chemistry Department
Max Planck Institute for Chemistry
55128 Mainz, Germany
j.wilson@mpic.de

Thomas Berkemeier
Multiphase Chemistry Department
Max Planck Institute for Chemistry
55128 Mainz, Germany

Steven Lelieveld
Multiphase Chemistry Department
Max Planck Institute for Chemistry
55128 Mainz, Germany

Ulrich Pöschl
Multiphase Chemistry Department
Max Planck Institute for Chemistry
55128 Mainz, Germany

November 11, 2020

ABSTRACT

Kinetic models are used to study the time-dependent concentrations of chemical species in systems consisting of multiple chemical reactions. Time-concentration graphs are the most common approach to present and analyze the output of kinetic models. While time-concentrations graphs are valuable for simple systems containing a handful of chemical reactions, they become a less effective as the number of reactions and coupling between chemical species increases. In order to overcome these challenges, we present an intuitive visualization tool that is designed to improve the interpretation, analysis and presentation of kinetic-model output for systems of chemical reactions (*KinViz*). The tool presents a system of chemical reactions in the form of a network. Specifically, this consists of a directed graph in which vertices and edges represent species and reactions, respectively. Using model output data, *KinViz* determines edge weightings by estimating reaction rates at each time point in the simulation. The dynamic evolution of the network is graphically illustrated by adjusting color and line thickness. To demonstrate this capability, we use *KinViz* to visualize two different chemical states of in the oscillatory Belousov-Zhabotinsky (BZ) reaction.

***K*eywords** Kinetic Modeling · Visualization · System of Chemical Reactions · Weighted Network

1 Background

Kinetic models are used to investigate systems of chemical reactions in a wide range of fields, from quantifying the generation of reactive oxygen species by air pollution particles [1], to optimizing the starting conditions for Fenton chemistry [2] and elucidating the controlling parameters of an oscillating reaction [3]. The development and analysis of such kinetic models is uniquely challenging as they often contain numerous coupled chemical reactions with rates spanning orders of magnitude. One particular challenge is the visualization of kinetic model output, which is necessary to analyze and present results. Conventionally, a time-concentration profile is used to illustrate how the concentration of each chemical species evolves in time. In such a plot, the x-axis represents time and the y-axis represents concentration. This approach is intuitive for systems with a handful of chemical reactions, but is of limited use for more complicated systems due to a loss of mechanistic information. To overcome this problem, a novel set of visualization tools are required.

Similar challenges have been overcome in the field of bioinformatics with the application of network methods to visualize and analyze complicated systems [4], for instance to study metabolic networks [5] and to predict the interactions of

drug molecules [6]. For chemical systems, it has previously been proposed that system of reactions may be analyzed using chemical reaction network theory [7, 8]. Within this graph-theory framework, nodes represent chemical species and the edges between them represent chemical reactions. Herein, we outline a tool *KinVis* that combines this network representation with the quantitative output of kinetic models in order to intuitively visualize systems of chemical reactions and their change with time.

2 Overview of *KinViz*

The *KinViz* algorithm converts a system of chemical reactions into a directed graph (digraph). The vertices in the digraph represent chemical species and the edges represent chemical reactions. Specifically, each directed edge connects a chemical reactant to a chemical product. *KinViz* then reanalyzes the time-concentration output of a kinetic model and combines this with the digraph so that users can observe the time evolution of the system.

2.1 Directed graph representation

In graph theory, an adjacency matrix $A(G)$ represents the connectivity between a set of vertices $V(G)$ and a set of edges $E(G)$ and can be represented as a directed graph G (Fig. 1) [9]. An adjacency matrix and directed graph can thus be used to describe a system of chemical reactions. In this form, chemical species are represented by a set of vertices, and the reactions connecting these chemical species by a set of edges [8].

$$A(G) = \begin{bmatrix} 0 & 1 & 0 \\ 1 & 0 & 0 \\ 1 & 1 & 0 \end{bmatrix}$$

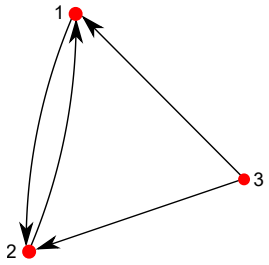

Figure 1: An example of a directed graph G and the corresponding adjacency matrix $A(G)$.

The directed graph of a system of chemical reactions is useful for model development, even in this simple form. For example, unexpected reactions or chemical species that are entirely disconnected from the graph may be more easily identified compared with a list of reactions. This helps to reduce the number of human errors that are made during model development and permits missing reactions in the model to be identified more intuitively.

2.2 Dynamic weighting of graph edges

The directed graph of a system of chemical reactions becomes most useful when combined with the time-concentration output of kinetic model. While there are several approaches to represent this data, using the rate of each reaction is perhaps the most intuitive and is therefore outlined here. The rate of each reaction $R_i(t)$ at time t, with units of concentration per unit time (e.g. $\text{cm}^{-3}\ \text{s}^{-1}$) is used to determine the edge weighting $R_{rp}(t)$ between reactant r and product p. The rate of reaction i with a rate coefficient k_i depends on the order of the reaction. For example, the dependence of a first-order reaction (Eq. 1) and a second-order reaction (Eq. 2) on the concentrations C_m and C_n of two chemical species m and n is shown.

$$R_i(t) = k_i C_m(t) \tag{1}$$

$$R_i(t) = k_i C_m(t) C_n(t) \tag{2}$$

These reaction rates are applied as a set of weightings $W(G)$ to each edge in the directed graph. In cases where more than one reaction connects a reactant and product, two alternatives approaches are possible. One option is that multiple edges between a reactant and product can be used, so that each edge represents a unique reaction. Alternatively, the rates of all reactions that convert a reactant into a product can be summed to give the total conversion rate $T_{rp}(t)$ for a given reactant-product edge at time t (Eq. 3). N is the number of reactions that converting r into p.

$$T_{rp}(t) = \sum_{i=1}^{N} R_i(t) \tag{3}$$

In principle, visualization of the edge weightings at this stage may already yield useful information. Generally however, standardizing the weightings permits far clearer presentation.

2.3 Standardization of weighted edges

As the weight of each edge may vary across orders of magnitude, the reaction rates must first be scaled in order to achieve effective visualization. One approach to scaling is to first take the logarithm of weightings and then standardize them. Here we propose three approaches to standardization, each provides a different perspective on the system of study. It should be noted that the most effective visual representation depends on the exact system, and eventually additional options can be added.

To compare the chemical reaction network at different points in time and therefore detect important chemical pathways, the edge weightings are firstly log transformed and then standardized across the entire time domain. The standardized edge weighting $Z_{rp}(t)$ (Eq. 4) for reactant-product combination rp at time t is determined from the calculated edge weighting $R_{rp}(t)$. μ and σ are the mean and standard deviation, respectively, of edge weightings across all reactant-product combinations and the entire time domain.

$$Z_{rp}(t) = \frac{R_{rp}(t) - \mu}{\sigma} \tag{4}$$

Alternatively, to view the time evolution of a single reactant-product combination, each reactant-product edge weighting $R_{rp}(t)$ may be standardized with respect to time (Eq. 5). In this case, μ_{rp} and σ_{rp} are the mean and standard deviation, respectively, of edge weights for a single reactant-product combination rp across the entire time domain.

$$Z_{rp}(t) = \frac{R_{rp}(t) - \mu_{rp}}{\sigma_{rp}} \tag{5}$$

To identify the most important chemical pathways in a system, each reactant-product edge weighting can be standardized with respect to other reactant-product edge weightings at specific time point t (Eq. 6). It should be noted that this approach is not suitable for comparing the network across two time points. $\mu(t)$ and $\sigma(t)$ are the mean and standard deviation, respectively, of all reactant-product edge weights for a given moment in time.

$$Z_{rp}(t) = \frac{R_{rp}(t) - \mu(t)}{\sigma(t)} \tag{6}$$

2.4 Color and line thickness

To complete the visualization, the standardized weightings are represented by color and line thickness. Many color combinations are possible, but one particularly distinctive approach is use the color blue to highlight *inactive* edges with negatives values of $Z_{rp}(t)$ and the color red to highlight *active* edges with positive values of $Z_{rp}(t)$. To complement this, reactant-product edges with negligibly small values of $R_{rp}(t)$ may be represented with a dashed-grey line to indicate that they are fully deactivated. Besides color, line thickness may also be scaled. The optimal form of visualization will depend on the dynamics of the system of study and the specific feature being investigated.

3 Example Visualization

KinViz is demonstrated using the ourput of a kinetic model for the oscillating Belousov-Zhabotinsky (BZ) reaction [3]. The full list of reactions, rate coefficients and starting concentrations are shown in Table 1. The time-concentration

profile provides useful information about the concentrations of each species (Fig. 2), but provides very little insight into the underlying chemical mechanisms governing the BZ system, even when only four chemical species are shown (e.g. Br_2, Ce^{4+}, Br^- and $HBrO_2$).

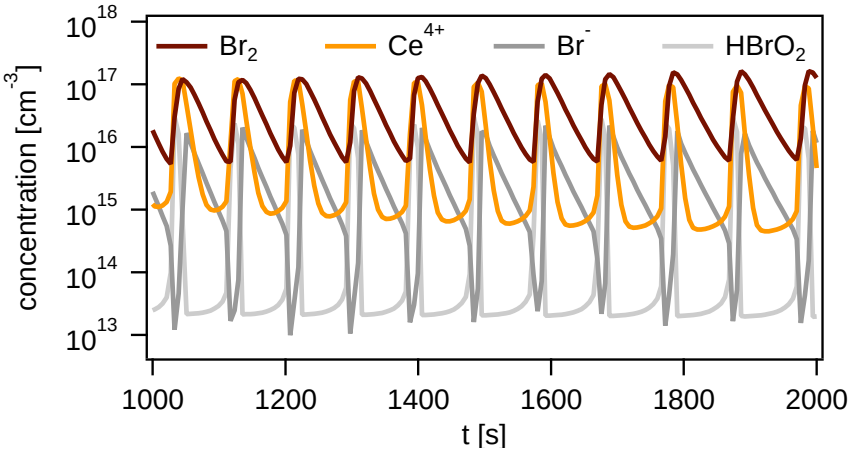

Figure 2: The time-concentration profile of the BZ reaction, predicted by a kinetic model. Even with four species selected (Br_2, Ce^{4+}, Br^- and $HBrO_2$) from the total of fifteen involved in the reaction, the behavior of the system remains difficult to understand.

Compared to a list of chemical reactions (Table 1), the relationships between chemical species can be better interpreted in the form of a directed graph (Fig. 3). For instance, highly connected species such as $HBrO_2$ are more easily distinguishable from less connected species, such as P_1, P_1 and $Br_{2(g)}$, which are not involved in further reactions. Another key advantage is that redox couples can easily be identified (e.g. Ce^{3+} and Ce^{4+}) and the reactions affecting them more clearly seen.

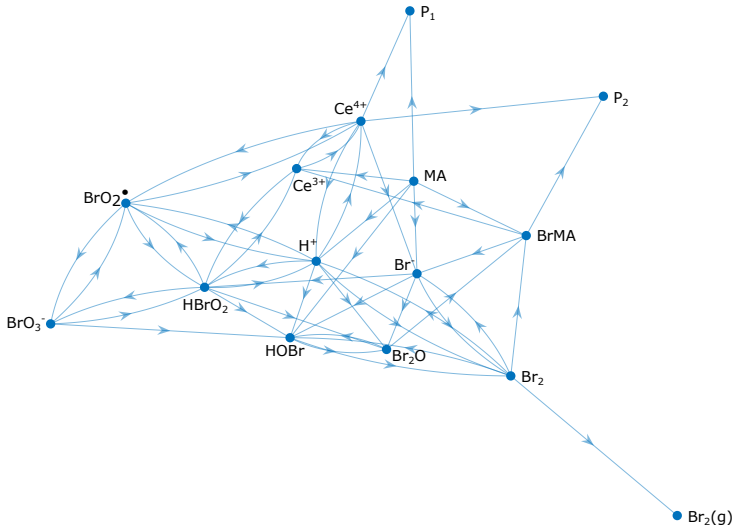

Figure 3: Directed graph showing the connections between chemical reactions and products.

KinViz is used to illustrate the BZ system at a) 1360 and b) 1400 s, these two time points represent two extremes in the oscillating cycle (Fig. 4). The reaction between BrO_3^- and $HBrO_2$ to form HOBr proceeds at a negligibly slow rate and is therefore marked with a dashed-grey edge. The line connecting MA to Ce^{3+} is blue at t = 1360 s, but becomes red at t = 1400 s. This indicates that the rate of the reaction between MA and Ce^{4+} switches from being *inactivate* to becoming *active*.

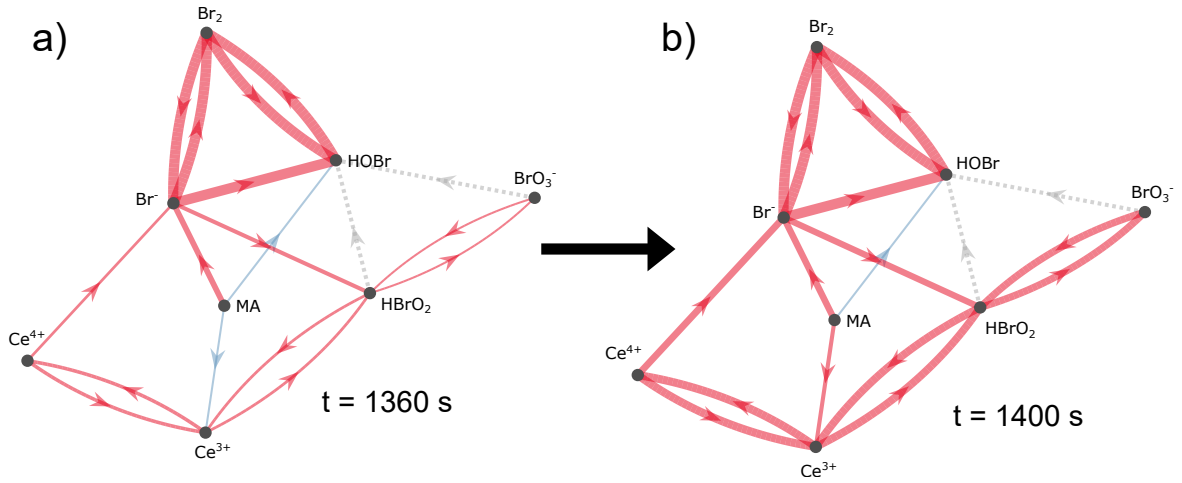

Figure 4: Two states of the oscillatory Belousov-Zhabotinsky (BZ) reaction visualized as a chemical reaction network with *KinViz*, at a) 1360 and b) 1400 s.

Table 1: Reactions and rate coefficients for kinetic modeling of the Belousov-Zhabotinsky reaction from Blagojevic et al. [3]. Malonic acid (MA) and bromomalonicacid (BrMA). The following starting concentrations are used: $[MA]_0 = 2.6 \times 10^{19}$ cm^{-3}, $[H^+]_0 = 7.8 \times 10^{20}$ cm^{-3}, $[BrO_3{}^-]_0 = 3.7 \times 10^{19}$ cm^{-3}, $[Br^-]_0 = 9.0 \times 10^{15}$ cm^{-3}, $[Ce^{3+}]_0 = 1.5 \times 10^{18}$ cm^{-3} and $[HOBr]_0 = 9.0 \times 10^{12}$ cm^{-3}.

Label	Reaction	Rate coefficient	Units
R1	$Br^- + HOBr + H^+ \longrightarrow Br_2 + H_2O$	7.03×10^{-33}	$cm^6 s^{-1}$
R-1	$Br_2 + H_2O \longrightarrow HOBr + H^+$	3.18	s^{-1}
R2	$HBrO_2 + Br^- + H^+ \longrightarrow Br_2O + H_2O$	1.64×10^{-35}	$cm^6 s^{-1}$
R3	$Br_2O + H_2O \longrightarrow 2\,HOBr$	3.21×10^{3}	s^{-1}
R-3	$2\,HOBr \longrightarrow Br_2O + H_2O$	5.35×10^{-13}	$cm^3 s^{-1}$
R4	$Br^- + BrO_3{}^- + 2\,H^+ \longrightarrow HOBr + HBrO_2$	2.17×10^{-83}	$cm^9 s^{-1}$
R5	$2\,HBrO_2 \longrightarrow BrO_3{}^- + HOBr + H^+$	5.80×10^{-18}	$cm^3 s^{-1}$
R6	$BrO_3{}^- + HBrO_2 + H^+ \longrightarrow 2\,BrO_2{}^\bullet + H_2O$	1.23×10^{-40}	$cm^6 s^{-1}$
R-6	$2\,BrO_2{}^\bullet + H_2O \longrightarrow BrO_3{}^- + HBrO_2 + H^+$	1.11×10^{-13}	$cm^3 s^{-1}$
R7	$Ce^{3+} + BrO_2{}^\bullet + H^+ \longrightarrow Ce^{4+} + HBrO_2$	8.82×10^{-38}	$cm^6 s^{-1}$
R-7	$Ce^{4+} + HBrO_2 \longrightarrow Ce^{3+} + BrO_2{}^\bullet + H^+$	1.86×10^{-17}	$cm^3 s^{-1}$
R8	$MA + Br_2 \longrightarrow BrMA + Br^- + H^+$	7.04×10^{-21}	$cm^3 s^{-1}$
R9	$MA + Ce^{4+} \longrightarrow Ce^{3+} + P_1 + H^+$	5.98×10^{-22}	$cm^3 s^{-1}$
R10	$BrMA + Ce^{4+} \longrightarrow Ce^{3+} + Br^- + P_2$	7.83×10^{-20}	$cm^3 s^{-1}$
R11	$Br_2O + MA \longrightarrow BrMA + HOBr$	7.02×10^{-23}	$cm^3 s^{-1}$
R12	$Br_2(sol) \longrightarrow Br_2(g)$	1.10×10^{-2}	s^{-1}

References

[1] Pascale S. J. Lakey, Thomas Berkemeier, Haijie Tong, Andrea M. Arangio, Kurt Lucas, Ulrich Pöschl, and Manabu Shiraiwa. Chemical exposure-response relationship between air pollutants and reactive oxygen species in the human respiratory tract. *Sci. Rep.*, 6:1–6, 2016.

[2] Christopher K. Duesterberg and T. David Waite. Process optimization of fenton oxidation using kinetic modeling. *Environ. Sci. Technol.*, 40:4189–4195, 2006.

[3] Slavica M. Blagojević, Slobodan R. Anić, Željko D. Čupić, Nataša D. Pejić, and Ljiljana Z. Kolar-Anić. Malonic acid concentration as a control parameter in the kinetic analysis of the Belousov–Zhabotinsky reaction under batch conditions. *Phys. Chem. Chem. Phys*, 10:6658–6664, 2008.

[4] Georgios A. Pavlopoulos, Maria Secrier, Charalampos N. Moschopoulos, Theodoros G. Soldatos, Sophia Kossida, Jan Aerts, Reinhard Schneider, and Pantelis G. Bagos. Using graph theory to analyze biological networks. *BioData Min.*, 4:10, 2011.

[5] Andreas Wagner and David A. Fell. The small world inside large metabolic networks. *Proc. R. Soc. B*, 2001.

[6] D. K. Arrell and A. Terzic. Network systems biology for drug discovery. *Clin. Pharmacol. Ther.*, 88:120–125, 2010.

[7] Martin Feinberg. Chemical reaction network structure and the stability of complex isothermal reactors—I. The deficiency zero and deficiency one theorems. *Chem. Eng. Sci.*, 42:2229–2268, 1987.

[8] M. Feinberg. *Foundations of chemical reaction network theory*. Applied Mathematical Sciences. Springer International Publishing, 2019.

[9] Douglas B. West. Introduction to graph theory - second edition. 2001.

2.4. Other Related Studies

Alongside these three key studies, this PhD project intersects nine further studies that are either published or in preparation for peer-reviewed journals (Appendix A). These studies each fall into one of two main topics: (1) the generation of reactive oxygen species by air pollution and (2) the adsorption and partitioning of small molecules and anthropogenic pollutants on graphitic materials.

In the human body, the overproduction of reactive oxygen species (ROS) such as hydroxyl radicals (OH), superoxide ($O_2^{\bullet -}$), and hydrogen peroxide (H_2O_2) is associated with adverse health effects (Chapple, 1997; Mudway et al., 2020). It is necessary to establish whether the generation of ROS following inhalation of air pollution is a significant pathway to disease. The mechanisms by which the chemical components generate ROS are complex, as illustrated by mixtures of hydroperoxides, fulvic and humic acids, and transition metals (Tong et al., in review). Redox reactions on the surface of particles play an important role in the generation of ROS, as in the case of cerium oxide nanoparticles (CeNPs; Filippi et al., 2019). The complex chemical mechanisms involved in chemical reactions can be resolved in kinetic models, for example, investigating the reactions between mixtures of particulate matter and antioxidants such as glutathione (GSH) in the lung-lining fluid, (Lelieveld et al., in preparation). Alongside laboratory experiments, it is useful to screen air pollutants for toxicity using their physicochemical properties. The electrochemical reduction potential and the lowest unoccupied molecular orbital (LUMO) energy are two such properties for which extensive data sets exist. Both relate to the transfer of electrons and are thus particularly suitable to predict redox reactions, such as the generation of ROS by oxidized PAHs in simulated lung fluid (Wietzoreck et al., in preparation). Beyond predicting the toxicity of pure compounds, the electrochemical reduction potential can also be measured in complex mixtures of aerosol particles and antioxidants (Shahpoury et al., 2019).

For a given molecule, the energy of adsorption on the surface of a particle is a key variable determining its distribution between the gas and the particle phase. Using quantum mechanical calculations (CCSD[T] and DFT), the energy of adsorption of carbon monoxide (CO) and methane (CH_4) on PAHs representative of graphene is shown to strongly depend on the orientation of the adsorbing molecule (Wilson et al., 2018; Vekeman et al., 2018). Besides orientation, the three-dimensional structure of a molecule influences its adsorption and therefore also its partitioning onto aerosol particles. For two polybrominated diphenyl ethers (PBDEs), observational data suggests that the more planar stereoisomer tends to more preferentially partition onto aerosol particles than its structurally-bent stereoisomer (Degrendele et al., 2018). While in most cases the dependence of adsorption and desorption on molecular orientation does not need to be explicitly resolved in kinetic models, such studies help to interpret and perhaps eventually predict mass-transport parameters that are normally obtained with experiment.

3. Conclusions and Outlook

Non-equilibrium Partitioning of PAHs

A kinetic model describes the adsorptive gas-particle partitioning and multiphase chemistry of polycyclic aromatic hydrocarbons (PAHs) on soot particles. In contrast to models that assume PAHs to be in equilibrium with aerosol particles, a time-dependent description of partitioning permits non-equilibrium behavior to be resolved. The kinetic model shows that the timescale needed for PAHs to equilibrate ranges from seconds to hours, depending on the temperature and the concentration of particles. Moreover, the PAHs with fewer rings, such as anthracene, are shown to equilibrate far more rapidly that larger PAHs such as benzo(a)pyrene. Further analysis reveals that this equilibration timescale depends on one of two controlling molecular processes: either adsorption or desorption. Alongside these numerical results, an equation is given to estimate these timescales, thus permitting observational data to be interpreted without a kinetic model.

The inclusion of chemical reactions in the model allows the timescales of chemical loss to be compared with the timescales of gas-particle partitioning. The surface reaction between PAHs and typical atmospheric concentrations of O_3 causes the gas-particle distribution of PAHs to be perturbed far from its equilibrium state. In one example, an O_3 concentration of 100 ppb causes the particulate fraction of pyrene to decrease from 0.24 to 0.05. The origin of this perturbation is explored using phase portraits, a geometric representation of the time evolution of the system. The phase portraits graphically illustrate the relative timescales of chemical loss and gas-particle partitioning. Given that chemical loss is sufficiently fast to influence the gas-particle distribution of PAHs, the implications for chemical transport models (CTMs) that treat partitioning and chemical loss separately with operator splitting are investigated. Specifically, the size of the error resulting from this treatment is shown to depend on the model time step and concentration of oxidants. Although this study focuses in-depth on the partitioning of PAHs, the tools and approaches contained within may be adapted to study the adsorptive partitioning of other semi-volatile compounds.

Global Modeling of Nitrated PAHs

For the first time, the formation and loss chemistry of two nitrated PAHs (NPAHs) are included in a global CTM (EMAC-SVOC). Accurately modeling the secondary formation of 2-nitrofluoranthene (2-NFLT) and 2-nitropyrene (2-NPYR) in the atmosphere requires detailed descriptions of their chemical reactions as well as those of their precursor PAHs.

The global CTM reveals important trends about the spatial distribution of 2-NFLT and 2-NPYR, for instance the model-calculated concentrations vary over 6 orders of magnitude across the globe. While the highest concentrations of NPAHs are predicted to be in regions where their precursor PAHs are emitted, analysis shows that the fraction of PAHs converted to NPAHs tends to be highest in air masses that are being transported away from source. Crucially, the model predicts that due to continuous formation, NPAHs will be spread across the globe, including remote regions such as the Arctic.

Simulations reveal that NPAHs are primarily removed from atmosphere by photolytic degradation rather than by deposition. Concentrations of 2-NFLT and 2-NPYR are therefore particularly sensitive to the rate coefficient for photolytic degradation. Future studies that focus on the effect of solvent, particle type and oxygen content on this rate coefficient would be beneficial.

At many observation sites, the global CTM overestimates the observed concentrations of 2-NFLT and 2-NPYR, most notably in less-polluted regions that have lower concentrations of NO_2. In part, this overestimation is attributed to using kinetic parameters obtained under high-NO_x conditions to describe the chemical formation of NPAHs. To resolve this, existing quantum mechanical calculations are adapted to develop a formation scheme in which the yield of NPAHs depends explicitly on the concentration of ambient NO_2. Inclusion of this novel formation scheme in the global CTM, alongside a reduced photolytic degradation rate, greatly improves prediction of NPAH concentrations and the fraction of PAHs converted into NPAHs. This improvement is particularly evident at a remote-monitoring site on the Noto Peninsula in Japan where long-term monitoring data is available. The identification of key processes that control the concentrations of NPAHs within the model helps to inform future experiments that better resolve kinetic parameters.

Visualizing Chemical Reactions as a Weighted Network

A computational tool *KinViz* is developed to graphically visualize the output of kinetic models in the form of a weighted network. The network dynamically evolves in time, representing the state of the chemical system at each point in the model output. In the

first part of the algorithm, a system of chemical reactions is converted into a directed graph in which chemical species are represented as vertices and chemical reactions as edges. In the second step, time-concentration output from the kinetic model is reanalyzed to estimate reaction rates at each point in time. Reaction rates are then standardized before being conveyed graphically using color and line thicknesses in order to distinguish between active and inactive reactions. Two states of the oscillating Belousov-Zhabotinsky reaction are illustrated to exemplify the capability of *KinViz*.

Summary and Outlook

A complete mathematical description of chemical processes in the atmosphere may only be achieved by investigating and integrating models across spatial levels. This PhD project addresses three key topics to examine the processes affecting atmospheric concentrations of PAHs and NPAHs, from the molecular to the global scale.

Firstly, a kinetic model reveals that the time needed for PAHs to equilibrate with the surface of soot particles is, depending on temperature and the number of particles, controlled primarily by either adsorption or desorption. Moreover, this equilibration time can be approximated with a time-independent equation that only requires parameters available from experiment. Apart from the surface of soot, a comprehensive model of the partitioning process requires descriptions of other types of aerosols, in particular the absorption of PAHs into liquid and viscous particles. Beyond PAHs, this kinetic model should also be extended to study the partitioning of other semi-volatile species such as NPAHs and PBDEs. One efficient approach to determine kinetic parameters is with quantum mechanical calculations, for instance the energy of adsorption on graphitic surfaces (e.g. Ding et al., 2014; Tang et al., 2018; Leonardi et al., 2020). Another key finding of the kinetic model is that chemical loss perturbs the distribution of PAHs far from its equilibrium state, increasingly so as the concentration of oxidants increase. For global CTMs, novel and computationally efficient approaches are required to avoid the errors that occur when describing chemistry and partitioning separately. One promising set of solutions emerge from the field of machine learning, where methods such as random forests and neural networks can be used to represent kinetic models in global CTMs (Keller and Evans, 2019; Silva et al., 2019; Zheng et al., 2019). Such techniques could be used to accurately describe the gas-particle partitioning of PAHs and other semi-volatile pollutants in such models.

Secondly, using a global CTM, the highest concentrations of two secondarily-formed NPAHs are predicted to be near to the emission sources of their precursors, however, continuous formation during transport spreads these NPAHs across much of the globe. Building on toxicology and epidemiological studies, the spatial distribution of atmospheric pollutants may be used to assess their exposure to humans and subsequent

health effects on a global scale (e.g. Lelieveld et al., 2015; Shrivastava et al., 2017). As these two NPAHs are both carcinogens, the next step would be to combine quantitative estimates of toxicity and population data with the spatial distribution of atmospheric concentrations obtained in this study. Assessing the impact of NPAHs on human health is an important step towards regulating its concentration in the atmosphere.

Finally, on the molecular scale, *KinViz* permits visualization of a complex system of chemical reactions in the intuitive form of a weighted network. As an alternative to time-concentration profiles, the interpretation and analysis of kinetic models is greatly enhanced. As kinetic models are used to study increasingly complex and extensive chemical systems, such as the generation of ROS by air pollutants, it becomes more challenging to identify important chemical pathways. Approaches developed to overcome similar challenges in the field of bioinformatics could be adapted in order to study chemical systems, for instance the use of cluster analysis to characterize the relationships between species and identify reoccurring network motifs (e.g. Pavlopoulos et al., 2011). Ultimately, a new generation of tools is required to automatically analyze large chemical systems; *KinViz* would provide one such useful platform to visualize these results.

4. Bibliography

Abbatt, J. P. D., Lee, A. K. Y., and Thornton, J. A.: Quantifying trace gas uptake to tropospheric aerosol: recent advances and remaining challenges, Chem. Soc. Rev., 41, 6555–6581, 2012.

Albinet, A., Leoz-Garziandia, E., Budzinski, H., Villenave, E., and Jaffrezo, J. L.: Nitrated and oxygenated derivatives of polycyclic aromatic hydrocarbons in the ambient air of two French alpine valleys: Part 1: Concentrations, sources and gas/particle partitioning, Atmos. Environ., 42, 43–54, 2008.

Andreae, M. O. and Crutzen, P. J.: Atmospheric aerosols: Biogeochemical sources and role in atmospheric chemistry, Science, 276, 1052–1058, 1997.

Andreae, M. O. and Rosenfeld, D.: Aerosol–cloud–precipitation interactions. Part 1. The nature and sources of cloud-active aerosols, Earth-Sci. Rev., 89, 13–41, 2008.

Anenberg, S. C., Horowitz, L. W., Tong, D. Q., and West, J. J.: An estimate of the global burden of anthropogenic ozone and fine particulate matter on premature human mortality using atmospheric modeling, Environ. Health Perspect., 118, 1189–1195, 2010.

Atkinson, R. and Arey, J.: Atmospheric chemistry of gas-phase polycyclic aromatic hydrocarbons: formation of atmospheric mutagens., Environ. Health. Perspect., 102, 117–126, 1994.

Baek, S. O., Field, R. A., Goldstone, M. E., Kirk, P. W., Lester, J. N., and Perry, R.: A review of atmospheric polycyclic aromatic hydrocarbons: Sources, fate and behavior, Water. Air. Soil Pollut., 60, 279–300, 1991.

Bandowe, B. A. M. and Meusel, H.: Nitrated polycyclic aromatic hydrocarbons (nitro-PAHs) in the environment – A review, Sci. Total Environ., 581-582, 237–257, 2017.

Berkemeier, T., Shiraiwa, M., Pöschl, U., and Koop, T.: Competition between water uptake and ice nucleation by glassy organic aerosol particles, Atmos. Chem. and Phys., 14, 12 513–12 531, 2014.

Berkemeier, T., Ammann, M., Krieger, U. K., Peter, T., Spichtinger, P., Pöschl, U., Shiraiwa, M., and Huisman, A. J.: Technical note: Monte Carlo genetic algorithm (MCGA) for model analysis of multiphase chemical kinetics to determine transport and reaction rate

coefficients using multiple experimental data sets, Atmos. Chem. Phys., 17, 8021–8029, 2017.

Bockhorn, H., ed.: Soot formation in combustion: mechanisms and models, Springer Series in Chemical Physics, Springer-Verlag, Berlin Heidelberg, 1994.

Bolton, J. L., Trush, M. A., Penning, T. M., Dryhurst, G., and Monks, T. J.: Role of quinones in toxicology, Chem. Res. Toxicol., 13, 135–160, 2000.

Bongaarts, J.: Human population growth and the demographic transition, Philos. Trans. R. Soc. Lond., B, Biol. Sci., 364, 2985–2990, 2009.

Boström, C.-E., Gerde, P., Hanberg, A., Jernström, B., Johansson, C., Kyrklund, T., Rannug, A., Törnqvist, M., Victorin, K., and Westerholm, R.: Cancer risk assessment, indicators, and guidelines for polycyclic aromatic hydrocarbons in the ambient air., Environ. Health Perspect., 110, 451, 2002.

Brasseur, G. P. and Jacob, D. J.: Modeling of atmospheric chemistry, Cambridge University Press, Cambridge, 2017.

Brauer, M., Freedman, G., Frostad, J., van Donkelaar, A., Martin, R. V., Dentener, F., Dingenen, R. v., Estep, K., Amini, H., Apte, J. S., Balakrishnan, K., Barregard, L., Broday, D., Feigin, V., Ghosh, S., Hopke, P. K., Knibbs, L. D., Kokubo, Y., Liu, Y., Ma, S., Morawska, L., Sangrador, J. L. T., Shaddick, G., Anderson, H. R., Vos, T., Forouzanfar, M. H., Burnett, R. T., and Cohen, A.: Ambient air pollution exposure estimation for the global burden of disease 2013, Environ. Sci. Technol., 50, 79–88, 2016.

Chapple, I. L.: Reactive oxygen species and antioxidants in inflammatory diseases, J. Clin. Periodontol., 24, 287–296, 1997.

Charlson, R. J., Schwartz, S. E., Hales, J. M., Cess, R. D., Coakley, J. A., Hansen, J. E., and Hofmann, D. J.: Climate forcing by anthropogenic aerosols, Science, 255, 423–430, 1992.

Cohen, A. J., Brauer, M., Burnett, R., Anderson, H. R., Frostad, J., Estep, K., Balakrishnan, K., Brunekreef, B., Dandona, L., Dandona, R., Feigin, V., Freedman, G., Hubbell, B., Jobling, A., Kan, H., Knibbs, L., Liu, Y., Martin, R., Morawska, L., Pope, C. A., Shin, H., Straif, K., Shaddick, G., Thomas, M., Dingenen, R. v., Donkelaar, A. v., Vos, T., Murray, C. J. L., and Forouzanfar, M. H.: Estimates and 25-year trends of the global burden of disease attributable to ambient air pollution: an analysis of data from the Global Burden of Diseases Study 2015, The Lancet, 389, 1907–1918, 2017.

Dachs, J. and Eisenreich, S. J.: Adsorption onto aerosol soot carbon dominates gas-particle partitioning of polycyclic aromatic hydrocarbons, Environ. Sci. Technol., 34, 3690–3697, 2000.

Ding, N., Chen, X., and Wu, C.-M. L.: Interactions between polybrominated diphenyl ethers and graphene surface: a DFT and MD investigation, Environ. Sci. Nano, 1, 55–63, 2014.

Finlayson-Pitts, B. J. and Pitts, J. N.: Chemistry of the upper and lower atmosphere: Theory, experiments, and applications, Academic Press, 1999.

Frenklach, M.: Reaction mechanism of soot formation in flames, Phys. Chem. Chem. Phys., 4, 2028–2037, 2002.

Friedman, C. L. and Selin, N. E.: Long-range atmospheric transport of polycyclic aromatic hydrocarbons: A global 3-D model analysis including evaluation of arctic sources, Environ. Sci. Technol., 46, 9501–9510, 2012.

Friedman, C. L., Zhang, Y., and Selin, N. E.: Climate change and emissions impacts on atmospheric PAH transport to the Arctic, Environ. Sci. Technol., 48, 429–437, 2014.

George, C., Ammann, M., D'Anna, B., Donaldson, D. J., and Nizkorodov, S. A.: Heterogeneous photochemistry in the atmosphere, Chem. Rev., 115, 4218–4258, 2015.

George, I. J. and Abbatt, J. P. D.: Heterogeneous oxidation of atmospheric aerosol particles by gas-phase radicals, Nat. Chem., 2, 713–722, 2010.

Goudie, A. S.: Human impact on the natural environment, Wiley-Blackwell, Hoboken, NJ, USA, 2018.

Hallquist, M., Wenger, J. C., Baltensperger, U., Rudich, Y., Simpson, D., Claeys, M., Dommen, J., Donahue, N. M., George, C., Goldstein, A. H., Hamilton, J. F., Herrmann, H., Hoffmann, T., Iinuma, Y., Jang, M., Jenkin, M. E., Jimenez, J. L., Kiendler-Scharr, A., Maenhaut, W., McFiggans, G., Mentel, T. F., Monod, A., Prévôt, A. S. H., Seinfeld, J. H., Surratt, J. D., Szmigielski, R., and Wildt, J.: The formation, properties and impact of secondary organic aerosol: current and emerging issues, Atmos. Chem. Phys., 9, 5155–5236, 2009.

Harrison, R. M. and Yin, J.: Particulate matter in the atmosphere: which particle properties are important for its effects on health?, Sci. Total Environ., 249, 85–101, 2000.

Haynes, B. S. and Wagner, H. G.: Soot formation, Prog. Energy Combust. Sci., 7, 229–273, 1981.

Hermans, C. and Bernard, A.: Lung epithelium–specific proteins, Am. J. Respir. Crit. Care Med., 159, 646–678, 1999.

Inomata, Y., Kajino, M., Sato, K., Ohara, T., Kurokawa, J.-I., Ueda, H., Tang, N., Hayakawa, K., Ohizumi, T., and Akimoto, H.: Emission and atmospheric transport of particulate PAHs in Northeast Asia, Environ. Sci. Technol., 46, 4941–4949, 2012.

International Energy Agency (IEA): World Energy Outlook 2020, World Energy Outlook, OECD, 2020.

IPCC: Climate Change 2013: The Physical Science Basis. Contribution of Working Group I to the Fifth Assessment Report of the Intergovernmental Panel on Climate Change, Cambridge University Press, Cambridge, United Kingdom and New York, NY, USA, 2013.

Jacob, D. J.: Introduction to atmospheric chemistry, Princeton University Press, Princeton, N.J, 1999.

Kampa, M. and Castanas, E.: Human health effects of air pollution, Environ. Pollut., 151, 362–367, 2008.

Keller, C. A. and Evans, M. J.: Application of random forest regression to the calculation of gas-phase chemistry within the GEOS-Chem chemistry model v10, Geosci. Model Dev., 12, 1209–1225, 2019.

Kelly, F. J. and Fussell, J. C.: Toxicity of airborne particles—established evidence, knowledge gaps and emerging areas of importance, Philos. Trans. R. Soc. A, 378, 20190 322, 2020.

Kelly, F. J., Cotgrove, M., and Mudway, I. S.: Respiratory tract lining fluid antioxidants: the first line of defence against gaseous pollutants, Cent. Eur. J. Public Health, 4 Suppl, 11–14, 1996.

Kerkweg, A., Buchholz, J., Ganzeveld, L., Pozzer, A., Tost, H., and Jöckel, P.: Technical Note: An implementation of the dry removal processes DRY DEPosition and SEDImentation in the Modular Earth Submodel System (MESSy), Atmos. Chem. Phys., 6, 4617–4632, 2006.

Keyte, I. J., Harrison, R. M., and Lammel, G.: Chemical reactivity and long-range transport potential of polycyclic aromatic hydrocarbons – a review, Chem. Soc. Rev., 42, 9333–9391, 2013.

Kim, K.-H., Jahan, S. A., Kabir, E., and Brown, R. J. C.: A review of airborne polycyclic aromatic hydrocarbons (PAHs) and their human health effects, Environ. Int., 60, 71–80, 2013.

Koop, T., Bookhold, J., Shiraiwa, M., and Pöschl, U.: Glass transition and phase state of organic compounds: dependency on molecular properties and implications for secondary organic aerosols in the atmosphere, Phys. Chem. Chem. Phys., 13, 19 238–19 255, 2011.

Kroll, J. H. and Seinfeld, J. H.: Chemistry of secondary organic aerosol: Formation and evolution of low-volatility organics in the atmosphere, Atmos. Environ., 42, 3593–3624, 2008.

Lakey, P. S. J., Berkemeier, T., Tong, H., Arangio, A. M., Lucas, K., Pöschl, U., and Shiraiwa, M.: Chemical exposure-response relationship between air pollutants and reactive oxygen species in the human respiratory tract, Sci. Rep., 6, 2016.

Lamarque, J.-F., Bond, T. C., Eyring, V., Granier, C., Heil, A., Klimont, Z., Lee, D., Liousse, C., Mieville, A., Owen, B., Schultz, M. G., Shindell, D., Smith, S. J., Stehfest, E., Aardenne, J. V., Cooper, O. R., Kainuma, M., Mahowald, N., McConnell, J. R., Naik, V., Riahi, K., and Vuuren, D. P. v.: Historical (1850–2000) gridded anthropogenic and biomass burning emissions of reactive gases and aerosols: methodology and application, Atmos. Chem. Phys., 10, 7017–7039, 2010.

Lammel, G., Sehili, A. M., Bond, T. C., Feichter, J., and Grassl, H.: Gas/particle partitioning and global distribution of polycyclic aromatic hydrocarbons – A modelling approach, Chemosphere, 76, 98–106, 2009.

Lelieveld, J., Evans, J. S., Fnais, M., Giannadaki, D., and Pozzer, A.: The contribution of outdoor air pollution sources to premature mortality on a global scale, Nature, 525, 367–371, 2015.

Leonardi, A., Ricker, H. M., Gale, A. G., Ball, B. T., Odbadrakh, T. T., Shields, G. C., and Navea, J. G.: Particle formation and surface processes on atmospheric aerosols: A review of applied quantum chemical calculations, Int. J. Quantum Chem., 120, e26 350, 2020.

Lighty, J. S., Veranth, J. M., and Sarofim, A. F.: Combustion aerosols: Factors governing their size and composition and implications to human health, J. Air Waste Manag. Assoc., 50, 1565–1618, 2000.

Lohmann, R. and Lammel, G.: Adsorptive and absorptive contributions to the gas-particle partitioning of polycyclic aromatic hydrocarbons: State of knowledge and recommended parametrization for modeling, Environ. Sci. Technol., 38, 3793–3803, 2004.

Ludlow, R. F. and Otto, S.: Systems chemistry, Chem. Soc. Rev., 37, 101–108, 2007.

Mu, Q., Shiraiwa, M., Octaviani, M., Ma, N., Ding, A., Su, H., Lammel, G., Pöschl, U., and Cheng, Y.: Temperature effect on phase state and reactivity controls atmospheric multiphase chemistry and transport of PAHs, Sci. Adv., 4, 2018.

Mudway, I. S., Kelly, F. J., and Holgate, S. T.: Oxidative stress in air pollution research, Free Radic. Biol. Med., 151, 2–6, 2020.

Pankow, J. F.: An absorption model of gas/particle partitioning of organic compounds in the atmosphere, Atmos. Environ., 28, 185–188, 1994.

Pavlopoulos, G. A., Secrier, M., Moschopoulos, C. N., Soldatos, T. G., Kossida, S., Aerts, J., Schneider, R., and Bagos, P. G.: Using graph theory to analyze biological networks, BioData Min., 4, 10, 2011.

Pope III, C. A.: Lung cancer, cardiopulmonary mortality, and long-term exposure to fine particulate air pollution, JAMA, 287, 1132, 2002.

Pöschl, U.: Atmospheric aerosols: Composition, transformation, climate and health effects, Angew. Chem. Int. Ed., 44, 7520–7540, 2005.

Pöschl, U., Rudich, Y., and Ammann, M.: Kinetic model framework for aerosol and cloud surface chemistry and gas-particle interactions – Part 1: General equations, parameters, and terminology, Atmos. Chem. Phys., 7, 5989–6023, 2007.

Pöschl, U., Martin, S. T., Sinha, B., Chen, Q., Gunthe, S. S., Huffman, J. A., Borrmann, S., Farmer, D. K., Garland, R. M., Helas, G., Jimenez, J. L., King, S. M., Manzi, A., Mikhailov, E., Pauliquevis, T., Petters, M. D., Prenni, A. J., Roldin, P., Rose, D., Schneider, J., Su, H., Zorn, S. R., Artaxo, P., and Andreae, M. O.: Rainforest aerosols as biogenic nuclei of clouds and precipitation in the Amazon, Science, 329, 1513–1516, 2010.

Ramanathan, V. and Carmichael, G.: Global and regional climate changes due to black carbon, Nat. Geosci., 1, 221–227, 2008.

Ramanathan, V., Crutzen, P. J., Kiehl, J. T., and Rosenfeld, D.: Aerosols, climate, and the hydrological cycle, Science, 294, 2119–2124, 2001.

Rapacioli, M., Calvo, F., Spiegelman, F., Joblin, C., and Wales, D. J.: Stacked clusters of polycyclic aromatic hydrocarbon molecules, J. Phys. Chem. A, 109, 2487–2497, 2005.

Ravindra, K., Sokhi, R., and Van Grieken, R.: Atmospheric polycyclic aromatic hydrocarbons: Source attribution, emission factors and regulation, Atmos. Environ., 42, 2895–2921, 2008.

Ravishankara, A. R.: Heterogeneous and multiphase chemistry in the Troposphere, Science, 276, 1058–1065, 1997.

Reinmuth-Selzle, K., Kampf, C. J., Lucas, K., Lang-Yona, N., Fröhlich-Nowoisky, J., Shiraiwa, M., Lakey, P. S. J., Lai, S., Liu, F., Kunert, A. T., Ziegler, K., Shen, F., Sgarbanti, R., Weber, B., Bellinghausen, I., Saloga, J., Weller, M. G., Duschl, A., Schuppan, D., and Pöschl, U.: Air pollution and climate change effects on allergies in the Anthropocene: Abundance, interaction, and modification of allergens and adjuvants, Environ. Sci. Technol., 51, 4119–4141, 2017.

Rockström, J., Steffen, W., Noone, K., Persson, , Chapin, F. S., Lambin, E. F., Lenton, T. M., Scheffer, M., Folke, C., Schellnhuber, H. J., Nykvist, B., Wit, C. A. d., Hughes, T., Leeuw, S. v. d., Rodhe, H., Sörlin, S., Snyder, P. K., Costanza, R., Svedin, U., Falkenmark, M.,

Karlberg, L., Corell, R. W., Fabry, V. J., Hansen, J., Walker, B., Liverman, D., Richardson, K., Crutzen, P., and Foley, J. A.: A safe operating space for humanity, Nature, 461, 472–475, 2009.

Rosenfeld, D.: Suppression of rain and snow by urban and industrial air pollution, Science, 287, 1793–1796, 2000.

Rosenkranz, H. S. and Mermelstein, R.: The genotoxicity, metabolism and carcinogenicity of nitrated polycyclic aromatic hydrocarbons, J. Environ. Sci. Health C, 3, 221–272, 1985.

Sadezky, A., Muckenhuber, H., Grothe, H., Niessner, R., and Pöschl, U.: Raman microspectroscopy of soot and related carbonaceous materials: Spectral analysis and structural information, Carbon, 43, 1731–1742, 2005.

San José, R., Pérez, J. L., Callén, M. S., López, J. M., and Mastral, A.: BaP (PAH) air quality modelling exercise over Zaragoza (Spain) using an adapted version of WRF-CMAQ model, Environ. Pollut., 183, 151–158, 2013.

Seinfeld, J. and Pandis, S.: Atmospheric chemistry and physics: From air pollution to climate change, 1998.

Shahpoury, P., Lammel, G., Albinet, A., Sofuoğlu, A., Dumanoğlu, Y., Sofuoğlu, S. C., Wagner, Z., and Zdimal, V.: Evaluation of a conceptual model for gas-particle partitioning of polycyclic aromatic hydrocarbons using polyparameter linear free energy relationships, Environ. Sci. Technol., 50, 12 312–12 319, 2016.

Shen, H., Huang, Y., Wang, R., Zhu, D., Li, W., Shen, G., Wang, B., Zhang, Y., Chen, Y., Lu, Y., Chen, H., Li, T., Sun, K., Li, B., Liu, W., Liu, J., and Tao, S.: Global atmospheric emissions of polycyclic aromatic hydrocarbons from 1960 to 2008 and future predictions, Environ. Sci. Technol., 47, 6415–6424, 2013.

Shen, H., Tao, S., Liu, J., Huang, Y., Chen, H., Li, W., Zhang, Y., Chen, Y., Su, S., Lin, N., Xu, Y., Li, B., Wang, X., and Liu, W.: Global lung cancer risk from PAH exposure highly depends on emission sources and individual susceptibility, Sci. Rep., 4, 2015.

Shiraiwa, M., Garland, R. M., and Pöschl, U.: Kinetic double-layer model of aerosol surface chemistry and gas-particle interactions (K2-SURF): Degradation of polycyclic aromatic hydrocarbons exposed to O_3, NO_2, H_2O, OH and NO_3, Atmos. Chem. Phys., 9, 9571–9586, 2009.

Shiraiwa, M., Pfrang, C., and Pöschl, U.: Kinetic multi-layer model of aerosol surface and bulk chemistry (KM-SUB): the influence of interfacial transport and bulk diffusion on the oxidation of oleic acid by ozone, Atmos. Chem. Phys., 10, 3673–3691, 2010.

Shiraiwa, M., Pfrang, C., Koop, T., and Pöschl, U.: Kinetic multi-layer model of gas-particle interactions in aerosols and clouds (KM-GAP): linking condensation, evaporation and chemical reactions of organics, oxidants and water, Atmos. Chem. Phys., 12, 2777–2794, 2012.

Shrivastava, M., Lou, S., Zelenyuk, A., Easter, R. C., Corley, R. A., Thrall, B. D., Rasch, P. J., Fast, J. D., Massey Simonich, S. L., Shen, H., and Tao, S.: Global long-range transport and lung cancer risk from polycyclic aromatic hydrocarbons shielded by coatings of organic aerosol, Proc. Natl. Acad. Sci. U.S.A., 114, 1246–1251, 2017.

Sies, H., Berndt, C., and Jones, D. P.: Oxidative stress, Annu. Rev. Biochem., 86, 715–748, 2017.

Silva, S. J., Heald, C. L., Ravela, S., Mammarella, I., and Munger, J. W.: A deep learning parameterization for ozone dry deposition velocities, Geophys. Res. Lett., 46, 983–989, doi:10.1029/2018GL081049, 2019.

Socorro, J., Lakey, P. S. J., Han, L., Berkemeier, T., Lammel, G., Zetzsch, C., Pöschl, U., and Shiraiwa, M.: Heterogeneous OH oxidation, shielding effects, and implications for the atmospheric fate of terbuthylazine and other pesticides, Environ. Sci. Technol., 51, 13 749–13 754, 2017.

Solomon, S.: Stratospheric ozone depletion: A review of concepts and history, Rev. Geophys., 37, 275–316, 1999.

Tang, H., Zhao, Y., Shan, S., Yang, X., Liu, D., Cui, F., and Xing, B.: Wrinkle- and edge-adsorption of aromatic compounds on graphene oxide as revealed by atomic force microscopy, molecular dynamics simulation, and density functional theory, Environ. Sci. Technol., 52, 7689–7697, 2018.

Tomaz, S., Jaffrezo, J.-L., Favez, O., Perraudin, E., Villenave, E., and Albinet, A.: Sources and atmospheric chemistry of oxy- and nitro-PAHs in the ambient air of Grenoble (France), Atmos. Environ., 161, 144–154, 2017.

Tong, H., Lakey, P. S. J., Arangio, A. M., Socorro, J., Shen, F., Lucas, K., Brune, W. H., Pöschl, U., and Shiraiwa, M.: Reactive oxygen species formed by secondary organic aerosols in water and surrogate lung fluid, Environ. Sci. Technol., 2018.

Tost, H., Jöckel, P., Kerkweg, A., Sander, R., and Lelieveld, J.: Technical note: A new comprehensive SCAVenging submodel for global atmospheric chemistry modelling, Atmos. Chem. Phys., 6, 565–574, 2006.

Turanyi, T. and Tomlin, A. S.: Analysis of kinetic reaction mechanisms, Springer-Verlag, Berlin Heidelberg, 2014.

van der Vliet, A., O'Neill, C. A., Cross, C. E., Koostra, J. M., Volz, W. G., Halliwell, B., and Louie, S.: Determination of low-molecular-mass antioxidant concentrations in human respiratory tract lining fluids, Am. J. Physiol., 276, L289–296, 1999.

Wesely, M. L.: Parameterization of surface resistances to gaseous dry deposition in regional-scale numerical models, Atmos. Environ., 23, 1293–1304, 1989.

Zheng, Z., Riemer, N., West, M., and Anantharaj, V. G.: Evaluation of machine learning approaches to estimate aerosol mixing state metrics in atmospheric models, Tech. rep., Oak Ridge National Lab. (ORNL), United States, 2019.

Zhou, S., Shiraiwa, M., D. McWhinney, R., Pöschl, U., and D. Abbatt, J. P.: Kinetic limitations in gas-particle reactions arising from slow diffusion in secondary organic aerosol, Faraday Discuss., 165, 391–406, 2013.

Zimmermann, K., Jariyasopit, N., Massey Simonich, S. L., Tao, S., Atkinson, R., and Arey, J.: Formation of nitro-PAHs from the heterogeneous reaction of ambient particle-bound PAHs with $N_2O_5/NO_3/NO_2$, Environ. Sci. Technol., 47, 8434–8442, 2013.

Zuberi, B., Johnson, K. S., Aleks, G. K., Molina, L. T., Molina, M. J., and Laskin, A.: Hydrophilic properties of aged soot, Geophys. Res. Lett., 32, 2005.

A. Personal List of Publications

1. Wilson, J., Pöschl, U., Shiraiwa, M., and Berkemeier, T.: Non-equilibrium interplay between gas-particle partitioning and multiphase chemical reactions of semivolatile compounds: mechanistic insights and practical implications for atmospheric modeling of PAHs, Atmos. Chem. Phys. Discuss., in review (2020).

2. Wilson, J., Octaviani, M., Bandowe, B., Wietzoreck, M., Zetzsch, C., Pöschl, U., Berkemeier, T., and Lammel, G.: Modeling the formation, degradation and spatiotemporal distribution of 2-nitrofluoranthene and 2-nitropyrene in the global atmosphere, Environ. Sci. Technol. (2020).

3. Wilson, J., Berkemeier, T., Lelieveld, S. and Pöschl, U.: *KinViz* - Visualization of systems of chemical reactions as weighted networks, in preparation (2020).

4. Lelieveld, S., Wilson, J., Lakey, P., Filippi, A., Tong, H., Shiraiwa, M., Pöschl, U., and Berkemeier, T.: ROS sources, buffers and reservoirs in the human respiratory tract, in preparation (2020).

5. Tong, H., Liu, F., Filippi, A., Wilson, J., Arangio, A. M., Zhang, Y., Yue, S., Lelieveld, S., Shen, F., Keskinen, H.-M. K., Li, J., Chen, H., Zhang, T., Hoffmann, T., Fu, P., Brune, W. H., Petäjä, T., Kulmala, M., Yao, M., Berkemeier, T., Shiraiwa, M., and Pöschl, U.: Reactive species formed upon interaction of water with fine particulate matter from remote forest and polluted urban air, Atmos. Chem. Phys. Discuss., in review (2020).

6. Wietzoreck, M., Filippi, A., Wilson, J., Shahpoury, P., Lelieveld, S., Tong, H., Berkemeier, T., Pöschl, U., Lammel, G., and Bandowe, B.: Oxidative potential of polycyclic aromatic compounds (PACs) and their predictability by chemical structure and reduction potential, in preparation (2020).

7. Filippi, A., Liu, F., Wilson, J., Lelieveld, S., Korschelt, K., Wang, T., Wang, Y., Reich, T., Pöschl, U., Tremel, W., and Tong, H.: Antioxidant activity of cerium dioxide nanoparticles and nanorods in scavenging hydroxyl radicals, RSC Adv. 9, 11077-11081 (2019).

8. Shahpoury, P., Harner, T., Lammel, G., Lelieveld, S., Tong, H., and Wilson, J.: Development of an antioxidant assay to study oxidative potential of airborne particulate matter, Atmos. Meas. Tech. 12, 6529–6539 (2019).

9. Mulder, M. D., Dumanoglu, Y., Efstathiou, C., Kukucka, P., Matejovicova, J., Maurer, C., Přibylová, P., Prokeš, R., Sofuoglu, A., Sofuoglu, S. C., Wilson, J., Zetzsch, C., Wotawa, G., and Lammel, G.: Fast formation of nitro-PAHs in the marine atmosphere constrained in a regional-scale Lagrangian field experiment, Environ. Sci. Technol. 53, 8914–8924 (2019).

10. Wilson J., Faginas-Lago, N., Vekeman, J., Cuesta, I. G., Sánchez-Marín, J., and Sánchez de Merás, A.: Modeling the interaction of carbon monoxide with Flexible Graphene: from coupled cluster calculations to molecular-dynamics simulations, ChemPhysChem 19, 774-783 (2018).

11. Vekeman, J., Cuesta, I. G., Faginas-Lago, N., Wilson, J., Sánchez-Marín, J., and Sánchez de Merás, A.: Potential models for the simulation of methane adsorption on graphene: development and CCSD (T) benchmarks, Phys. Chem. Chem. Phys. 20, 25518-25530 (2018).

12. Degrendele, C., Wilson, J., Kukučka, P., Klánová, J., and Lammel, G.: Are atmospheric PBDE levels declining in central Europe? Examination of the seasonal and semi-long-term variations, gas–particle partitioning and implications for long-range atmospheric transport, Atmos. Chem. Phys. 18, 12877-12890 (2018).